1-1-2013

Electrokinetic Mixing and Separation in Microfluidic Systems

FANG YANG
University of South Carolina

ELECTROKINETIC MIXING AND SEPARATION IN MICROFLUIDIC SYSTEMS

by

FANG YANG

Master of Science
Jilin University, 2008

Bachelor of Science
Jilin University, 2005

Submitted in Partial Fulfillment of the Requirements

For the Degree of Doctor of Philosophy in

Mechanical Engineering

College of Engineering and Computing

University of South Carolina

2013

Accepted by:

Dr. Guiren Wang, Major Professor

Dr. Chen Li, Committee Member

Dr. Sarah Baxter, Committee Member

Dr. Richard L. Goodwin, Committee Member

Lacy Ford, Vice Provost and Dean of Graduate Studies

ACKNOWLEDGEMENT

Foremost, I would like to express my sincere gratitude to my advisor Prof. Guiren Wang for the continuous support of my Ph.D study and research, for his patience, motivation, enthusiasm, and immense knowledge. His guidance helped me in all the time of research and writing of this dissertation. I could not have imagined having a better advisor and mentor for my Ph.D study.

I would also like to thank my committee members, Dr. Chen Li, Dr. Sarah Baxter and Dr. Richard L. Goodwin for their friendly guidance, thought-provoking suggestions. Their profound knowledge and insight highly improved my research levels and broadened my academic horizons.

I thank my fellow lab mates in Microfluidic and Nanofluidic Group: Dr. Cuifang Kuang, Wei Zhao, and Paul Wach for the stimulating discussions, for the sleepless nights we were working together, and for all the fun we have had in the last five years. Specially, Wei Zhao did a lot of works and helping me on the turbulence mixing project, it is impossible to finish this project without his help.

Finally, I would also like to thank my parents. They were always supporting me and encouraging me with their best wishes.

ABSTRACT

Electrokinetics involves the study of liquid or particle motion under the action of an electric field; it includes electroosmosis, electrophoresis, dielectrophoresis, and electrowetting, etc. The applications of electrokinetics in the development of microfluidic devices have been widely attractive in the past decade. Electrokinetic devices generally require no external mechanical moving parts and can be made portable by replacing the power supply by small battery. Therefore, electrokinetic based microfluidic systems can serve as a viable tool in creating a lab-on-a-chip (LOC) for use in biological and chemical assays. Here we present our works of electrokenitic based mixing and separation in microfluidics systems.

Firstly, we present a novel fast micromixer of quasi T-channel with electrically conductive sidewalls and some newly observed phenomena on mixing process. The sidewalls of the microchannel can be either parallel or non-parallel with an angle. The mixing behaviors in the micromixer with different angles between the two electrodes located at the sidewalls are studied in terms of velocity and scalar concentration distributions. It is found that mixing can be enhanced rapidly at a small angle about 5 ° between the two electrode sidewalls even at low AC voltage, compared with that in parallel sidewalls. The effectiveness of several parameters were explored for the further enhancement of the fluid mixing, including conductivity gradient, AC electric flied frequency, applied voltage, AC signal phase shift between the electrodes, etc. The results

reveal that the mixing is the stronger under high conductivity gradient, low frequency, high voltage and 180 ºsignal phase shift between the two electrodes. Fast mixing under high AC frequency can be achieved in this quasi T-channel micromixer as well. The most important observation is that for the first time turbulence can be achieved under AC electrokinetic forcing at low Reynolds number in the order of 1 in this novel design. Thus, turbulent mixing can also be generated in micofluidics to cause rapid mixing. The turbulent flow is also measured with laser induced fluorescence photobleaching anemometer.

Secondly, we have successfully manipulated and isolated cancer cells from other cells and bio-particles, by dielectrophoresis (DEP) in a microfluidic platform in a continuous operation. In this cell sorter, the cancer cells were treated as target cells and were deflected to a side channel from a main channel as they experienced a negative DEP force, when an AC electric field at the cross-over frequency of the cancer cells was supplied. This motion consequently led to the separation of the cancer cells from other cells and bio-particles. Colorectal cancer cells (HCT116) were firstly separated from human Embryonic Kidney 293 cells (HEK 293) and *Escherichia coli* (*E. coli*) bacterium. Then prostate cancer cells (LNCaP) were separated from HCT116 cells. Furthermore, we developed a cascade configuration sorter to increase purity of the isolated target cells, and a staggered sorter with two side channels in opposite side walls to increase sample throughput without compromising enrichment factor. Comparing to a single side channel DEP cell sorter, the isolation purity was improved from 80% to 96% by single cascade sorter and the sample throughput was increased from 0.2 μL/min to 0.65 μL/min by a single staggered side channel sorter.

Here we report the theory and method, experimental setup, results and discussion. The future work and direction will be proposed as well.

TABLE OF CONTENTS

LIST OF FIGURES

1. INTRODUCTION

1.1 Electrokinetics

Electrokinetics is the study of liquid or particle motion under the action of an electric field; it covers the following types of particle and fluid transport mechanisms: elecrokinetic instability, electrophoresis, electrokinesis, dielectrophoresis, electro-osmosis, electrowetting and electrorotation. In general, the phenomena relate to the direct conversion of electrical energy into kinetic energy, and vice versa.

1.2 Microfluidics

Microfluidics refers to a set of technologies that control and manipulation of fluids that are geometrically constrained to a small, typically sub-millimeter scale. Microfluidics can deliver greater efficiency in existing processes (faster sequences, higher throughput, smaller sample and solvent volumes and lower costs), and also enabling newer processes to be developed in areas such as genetic research, chromatography and pharmaceuticals.

The behavior of fluids at the microscale can differ from 'macrofluidic' behavior in that factors such as surface tension, energy dissipation, and fluidic resistance start to dominate the system. Microfluidics studies how these behaviors change, and how they can be worked around, or exploited for new uses.[1-3]

At small scales (channel diameters of around 100 nanometers to several hundred micrometers) some interesting and sometimes unintuitive properties appear. In particular, the Reynolds number (which compares the effect of momentum of a fluid to the effect of viscosity) can become very low. A key consequence of this is that fluids, when side-by-side, do not necessarily mix in the traditional sense; molecular transport between them must often be through diffusion.[4]

The most common form of microfluidics in practice is lab-on-a-chip device.

1.3 Lab on a chip

A lab-on-a-chip (LOC) [5] device integrates one or several laboratory functions on a single chip of only millimeters to a few square centimeters in size. LOCs deal with extremely small fluid volumes down to less than picoliters.[6] Lab-on-a-chip devices are a subset of MEMS devices and often indicated by "Micro Total Analysis Systems" (μTAS) [7-9] as well. These devices offer significant advantages over their macro-scale counterparts, including a reduction in reagent consumption and the amount of chemical waste, a more rapid analysis with parallel operation for high throughput, and a significant improvement in performance.[10] Among these functions, two-fluid mixing is an essential process for many microfluidic lab-on-a-chip devices.

1.4 Two opposite effects of electrokinetics

1.4.1 Two-fluid mixing

The mixing of two or more miscible fluids in microfluidic is very important in many applications. For example, often chemical analysis in microfluidics involves mixing of two fluids, it is important to achieve a homogenized solution of the reagents to ensure maximum products in chemical reactions. Meanwhile, in many biological processes, such as enzyme reaction, protein folding, DNA purification,[11] etc. These processes' performance, e.g. sensitivity and measurement of chemical kinetics depends strongly on the effectiveness and rapidness of the samples-reagents mixing. Fast mixing will generate more signals to increase the sensitivity and enable more accurate measurement of the kinetics. However, traditionally, turbulence is usually absent due to the nature of low Reynolds number in microfluidics, the flows are laminar and the mixing is slow and carried out by molecular diffusion. Thus, fast and effectual mixing of two fluids inside microchannels could be very demanding. Therefore, developing new techniques and methodologies to increase the interfacial contact surface area between adjacent streams for mixing enhancement in the diffusion dominated processes inside microchannels is very important and necessary to improve the performance of 'lab-on-a-chip' devices.

An ideal micromixer should possess features of rapid and efficient mixing, be compact in size, be easily integrated with other components. Achieving such a mixer is an essential but challenging task when developing microfluidic devices for chemical and biological analysis applications. The development of micromixing approaches for microfluidic applications has attracted the attention of many research groups worldwide,

and a quite large number of papers have already appeared which reported on the development of micromixers based on different strategies.

Electrokinetics generally involves the study of liquid or particle motion under the action of an electric field; this includes electroosmosis, electrophoresis, dielectrophoresis, and electrowetting. These phenomena have been used as an active control method to achieve fluid mixing enhancement inside a quasi T-channel. Oddy et al first presented an active micromixer,[12] in which an AC electric field induces a more chaotic flow field to enhance the mixing of two pressure-driven flow streams. Besides, it was demonstrated by Shin et al,[13] that more chaotic trajectories can be generated in a cross-shaped microchannel by a time-dependent electric field. Moreover, El Moctar et al. used wire electrodes placed in the direction perpendicular to the interface between the two fluids with different electrical properties, to create a transversal secondary flow and achieved mixing.[14]

These new micromixers [15-28] can generally be categorized into two groups: passive and active mixers.[29, 30]

1.4.1.1 Passive electrokinetic micromixers

Passive mixing refers to the mixing effect in electrokinetically driven systems and is enhanced by virtue of their particular geometry topologies, surface properties, or instability phenomenon which occurs naturally under a static (DC) electric field. Passive mixers do not require external energy; the enhanced mixing process relies entirely on the augmentation of diffusion of chaotic advection through special geometrical design of

microchannals.[31, 32] Here we review some Passive electrokinetic micromixer examples based on different strategies.

T- and quasi T-shaped microchannels with two inlets were generally used microfluidic devices design for the mixing of analytes and reagents in the literature. Jacobson et al. developed a micromixer Mixing of multiple parallel electroosmotic streams based on molecular diffusion.[10] They proposed an electroosmotic-based microfluidic device designed with series T-intersections capable of multiple samples parallel mixing. The device was tested by mixing a sample with buffer in a dilution experiment.

Besides the multi-stream lamination mixing mentioned above, there is a mixing method called Grooved surface enhanced electroosmotic mixing. Stroock et al.[33] proposed a chaotic mixing channel with patterned grooves for pressure-driven flow system. The transverse flows can be produced in the grooved channels which result in a helical flow motions at a low Reynolds number regime.

Surfaces with non-uniform zeta potentials are one way to produce vortices or specific flow structures to achieve mixing in electroosmotic flow fields. Strook et al. firstly observed this flow phenomena experimentally.[34] Later on, these induced localized circulations in the steady flow field were successfully employed to improve species mixing in a microchannel, by many researchers.[35]

DC electrokinetic instability (EKI) mixing attracted a great attention of researching recent years, and this phenomenon has been brought into many microfluidics mixing applications. The electrokinetic instability (EKI) phenomenon was firstly observed experimentally in microfluidics by Oddy et al.[36] This instability phenomenon

is not due to mechanisms such as time-modulated electric fields and Joule heating effects. It is described by charge accumulation at perturbed interfaces due to electrical conductivity gradients, which exist in the bulk flow.[37]

1.4.1.2 Active electrokinetic mixers

Active mixing refers to the enhancement of mixing in electrokinetically driven microfluidic systems using a time-dependent electric field or in pressure-driven flow systems by means of an externally time-dependent or time-indepentent electrical force. Several active micro-mixers generating external disturbances in terms of temperature,[38] pressure,[39, 40] electro-hydrodynamics,[14] dielectrophoretics,[41] acoustics [42] as well as magnetohydrodynamics [43] have already been published to effectively enhance fluid mixing in microchannels.[37, 44]

Lee et al. and Deval et al. have used dielectrophoretic forces as a perturbation source to facilitate chaotic mixing in simple microchannel geometry.[41] Dielectrophoresis (DEP) refers to the polarization of a particle or biological element relative to a suspension medium in a non-uniform electric field which results in motion. The main stream in their device was driven by a syringe pump. In this device, the working unit is composed of square cavity and electrodes on the side walls. The saddle point regions can be generated when the positive or negative DEP force is large enough to overcome hydrodynamic force, where particle distributions are stretched and folded, resulting in chaotic trajectories. However, this kind of dielectrophoresis mixing device can only deal with the mixing have particles involved. This disadvantage limited its application areas.

In contrast of DC EKI mixing, more chaotic flow patterns may be induced by time-dependent electric fields, which can improve the mixing performance at a low intensity of electric field. Oddy et al. first presented an active AC electrokinetic instability micromixer in which an AC electric field induces a more chaotic flow field to enhance the mixing of a two pressure-driven flow stream.[36] In their mixing, a high intensity AC electric field (1 kV/cm with a relatively low frequency) from side channels was still required to induce electrokinetic instability for enhancing mixing.

By pulsing their velocities or pressures in certain arrangement, efficient active mixing scheme to enhance the mixing effect of two pressure-driven flow streams at low Reynolds number could also be achieved. Dodge et al. presented a mixer comprising a main channel and one pair of side channels in which the mixing species were stirred by pulsing the velocities of the fluids introduced through the side channels.[45]

1.4.1.3 proposed electrokinetic micromixers

Although many significant results have already been obtained through those previous works,[5, 43, 46-51] much effort is still needed to improve our understanding about electrokinetic mixing under AC electric field and to make the electrokinetic micromixers more efficient and flexible for “lab-on-a-chip” applications due to its importance.

Here we report a new design of active AC electrokinetic micromixer and the corresponding parametric study of effectiveness of achieving rapid fluid mixing inside a quasi T-microchannel with non-parallel conductive sidewalls in pressure-driven flows by means of an externally time-dependent electrical force. The observed phenomenon could

advance our understanding pertaining to the fundamental physics of electrokinetics and improve the mixing technology in microfluidics. Epi-fluorescence imaging technique was used to conduct qualitative flow visualization and quantitative scalar concentration field measurements to quantify the fluid mixing process inside the quasi T-shaped microchannel. Parameters such as angles between two electrodes, and voltage phase shift variation between two electrodes, have been investigated.

1.4.1.4 Electrokinetically forced turbulence in microfluidics with Reynolds number on the order of unity

In macroflows, where Re is relatively high, mixing can usually be enhanced by forcing flow to be turbulent. Although there can be elastic turbulence in a polymer solution at low Re [52], it is conventionally believed that the flow in microfluidics, where typical Re is on the order of 1 or lower and fluids are often approximately seen as Newtonian, can only be laminar [33, 53] and cannot be turbulent [54, 55]. So far many efforts have been explored to enhance mixing in microfluidics [30], e.g. using sufficiently high DC or AC voltage to force flow in a microchannel based on electrokinetic instability [24, 36, 37], the forced flows in these studies are chaotic advection, not turbulence [30].

Can there be turbulence in a flow with Re on the order of 1? To address this issue, we have to know what turbulence is first. Although it is difficult to give an accurate definition of turbulence, there are some common features in turbulence[56]: fast diffusion, random motion, high dissipation rate, continuous flow, multiscale eddies, 3-D and high Re. Based on these features, common knowledge is that the critical Reynolds number Re_c is 2100~2300 in tubes. In microfluidics textbooks,[4, 57] it is understood that there should

be no turbulence unless pressure is very high. As we know, turbulence is a complex and non-linear phenomenon, and there are evidences that Re_c in microchannels is similar to that in macroflows, although debates exist.[58] In macroflows, we have realized ultrafast mixing and strong turbulence at relatively low Re based on receptivity.[59, 60] In the present work, we demonstrate that turbulence can be achieved in an electrokinetically forced pressure driven flow in microchannels with Re on the order of 1. In addition, we then characterized the microflow with a newly developed velocimeter and found that the corresponding forced flow even possesses the well-known -5/3 power spectrum and exponential tail of probability distribution function (pdf) of velocity increment, which can only be achieved at very high Re in macroflows. The present work intends to demonstrate that the feature of high Re seems not to be necessary for turbulence, at least for the electrokinetically forced flow in microfluidics.

1.4.1.5 Scalar turbulence

Recently scalar turbulence and mixing have rapidly attracted attention in physics and engineering [61-67]. Scalar turbulence and mixing strongly depends on flow, i.e. transition from laminar to turbulent flows (instability issue), universal small-scale structures in fully developed high Re turbulent flows, large coherent structures and control of the these structures for scalar mixing enhancement.

In turbulent flows the well-known phenomenological theory pioneered by Kolmogorov predicts that the power spectrum density (PSD) for velocity fluctuations possesses a universal -5/3 slope based on isotropic turbulence [68] if the Reynolds number is sufficiently high. For the small scalar structures in scalar turbulence, it is also

well known that Obukhov and Corrsin extended this theory to scalar fluctuations, i.e. a scalar PSD also has a -5/3 slope as long as Re is sufficiently high [69-71]. Batchelor further predicted that, when Schmidt number (Sc) is sufficiently high, i.e. $Sc = D_m/\nu >> 1$, (D_m is molecular diffusion coefficient) there is a –1 spectrum in viscous-convective subrange beyond the –5/3 spectrum as well [72].

However, there is currently a debate on whether this -1 spectrum exists. This prediction has been supported by some experiments [73-76] and numerical simulations [77-80]. However some other experiments [81, 82] and numerical simulations [83-85] have not observed it. Most positive experiments were done in 1960s and had limited spatial resolution, and experimental validation of the Batchelor theory faces the well-known challenge: the spatial resolution is too low to make a proper test of the Batchelor spectrum at high Re [81] [82]. So far the optical based measuring techniques have limited resolution due to well-known diffraction limit. Therefore, although Batchelor theory has been widely accepted for more than five decades, reliable experimental validation that has convincing high spatial resolution is still missing.

So far, to the best of our knowledge, the aforementioned scalar turbulence has been studied only in macroflows. This is because that commonly the critical Reynolds number $Re_D = D*U/\nu$ (D, U and ν are pipe diameter, mean velocity and viscosity respectively) in a pipe flow is about ~ 2,100 (If the inlet has a settling chamber with high contraction ratio, the acceleration flow is more stable, and the corresponding critical *Re* will greatly increase, [86]. Since turbulence can enhance mixing, if fast mixing between two fluids is needed, turbulence is generated either by increasing Reynolds number or using turbulence generator to generate turbulence in macroflows. In microfluidics,

however, where the Reynolds number is normally below or on the order of unity, it is believed that there are only laminar flows and the corresponding mixing is usually slow.

In macroflows, it has been recently observed that, mixing layers in a confined configuration (i.e. in a pipe) exhibit an extraordinarily high receptivity under specific forcing, i.e. strong external forcing can be accepted from the shear flow without the saturation and the corresponding forcing energy can be converted into large coherent structures rapidly, even at relatively low *Re* [59, 87, 88]. Hence, at high forcing level, an originally laminar flow can be forced into a turbulent flow. Such a confined mixing layer in a pipe could provide a new opportunity to force a low Re flow to achieve some features of high Re flow. Using the similar methodology, i.e. active forcing, we even have recently also achieved turbulence in microfluidics with Re in the order of only 1 when electrokinetic force is used to force a pressure driven flow, and furthermore, in such a low Re flow in microfluidics, we have surprisingly realized Kolmogorov -5/3 spectrum for velocity fluctuation and exponential tail of probability distribution function of velocity increment [89, 90].

Here we report, for the first time (to the best of our knowledge), our experimental characterization of the corresponding scalar turbulence in microfluidics. It is found that the forced scalar turbulence can possess some important features of high *Re* turbulent flows, such as the corresponding Obukhov-Corrsin -5/3 spectrum and exponential tail of concentration probability distribution function [91, 92]. However, we have not found the well-known -1 Batchelor spectrum beyond the Obukhov and Corrsin spectrum in the viscous-convective subrange.

1.4.2 Electrokinetic separation phenomena

Separation is often a necessary first step in performing an analysis. Chemical species and particles (bio-particles) separations are a critical component of analytical and synthetic chemistry. In microfluidic applications, one can separate a sample comprising multiple chemical species or different particles into individual components by inducing the components of a sample to move at different velocities, in a microchannel.

1.4.2.1 Microfluidic based cell separation methods review

Compact microfluidic systems (or lab-on-a-chip system, Micro Total Analysis System (lTAS)) can be used to manipulate and separate biological particles. These compact microfluidic systems nowadays are of wide interest in biodefense and clinical diagnostic applications, and have attracted much attention recently.[93-95] It is a critical component in biochemistry, molecular biology and synthesis protocols.[96] Microfluidic systems are expected to have major impacts on biomedical research, clinical diagnosis,[97] point of care, food pathogen screening,[98] environmental testing, and other endeavors by providing automated, portable solutions to a wide range of fluid based problems.[99-101] Here we review several current broadly used state-of-the-art microfluidic cell separation designs and systems. Both of their advantages and disadvantages will also be discussed briefly.

1.4.2.1.1 Fluorescence-activated cell sorting (FACS) or flow cytometry

FACS is a laser induced fluorescent (LIF) detection based, biophysical technology employed in cell counting, sorting, biomarker detection and protein engineering, by

suspending cells in a stream of fluid and passing them by an electronic detection apparatus. The original name of the fluorescence-based flow cytometry technology was "pulse cytophotometry" (German: Impulszytophotometrie). FACS has been the cell sorting method of choice for many biologists, because it is mature engineering developed. And it can provide high sensitivity and also high throughput. Modern flow cytometers are able to analyze several thousand particles every second, in "real time," and can actively separate and isolate particles having specified properties.

In this flow cytometry, the cell surface markers are identified via specific antibodies labeled with fluorescent molecules. Cells are identified via fluorescence signal from individual cells, along the flow of cell solutions streaming past a detector, one by one but at a relatively high speed. Specially, immunohistochemistry or cytosolic expression of GFP-tagged proteins is used to identify the subset of cells with specific properties. There are mainly two method of detection, besides the detection of fluorescent light scattering coming from each cell , it can also be done in the way of that detecting the absence of fluorescence signal from cell. Then after detection and analysis, each liquid droplet is deflected using a tangential electric field to different buckets for sorting. FACS involves ejecting single cells in liquid droplets of around 70 lm, which is a similar process used in an inkjet printer.

The first impedance-based flow cytometry device, based on Coulter principle, was disclosed in U.S. Patent 2,656,508, issued in 1953, to Wallace H. Coulter. Mack Fulwyler was the inventor of the forerunner to today's flow cytometers - particularly the cell sorter. Fulwyler developed this in 1965 and published it in Science.[102] The first fluorescence-based flow cytometry device (ICP 11) was developed in 1968 by Wolfgang Göhde, filed

for patent on 18 December 1968.[103] In their design, “The central vertical nozzle of the conduit is disposed with its opening in the sharply focussed object plane of a microscope and uniformly illuminated from below or by incident illumination. Electronic counting and recording devices are coupled to the output of the microscope for analyzing light pulses occuring in the nozzle when particles pass therethrough.” Which is the basic idea for laser induced fluorescent signal based flow cytometer.

In recent years, fluorescence-based sorting of cells has been implemented in microfluidic devices more and more. Cells often flow through a microchannel, the laser detection usually applied at the upstream of the flow, and then an external force (electrophoresis, optical, hydrostatic pressure changes) could be sufficiently influence whether each cell is deflected left or right at the downstream channel junction. The main difference between conventional FACS and microfluidic FACS is that, in microfluidic channels, flow switching (necessary for sorting) would be subject to much higher drag, compared with droplet-based switching in conventional FACS. This inherent limitation can be overcomed by building a parallel array of microfluidic cytometer units, which is a advantage of microfluidic systems.

However, there are several technical drawbacks associated with this Flow Cytometry method (including equipment expense, clogging, contamination,serial nature of the sorting, and cell viability after ejection, deflection, and impact). The most important disadvantage is that, cell labeling via antigen-antibody reaction, is required for the fluorescent signal detection, If the cell cannot be identified by antigen-antibody reaction, then it cannot be separated from another cells by this flow cyrometry method. Therefore,

label-free cell separation method is demanded for diagnostic and many other real life applications.

1.4.2.1.2 Magnetic cell sorting

The main idea for magnetic cell sorting is that, cells are firstly incubated with magnetic nanoparticles coated with antibodies against a particular surface antigen, which causes the cells expressing this antigen to attach to the magnetic nanoparticles. After that, the cell solution is transferred on a column or microchannel, placed in a strong magnetic field. In this step, the cells attached to the nanoparticles (expressing the antigen) will stay on the column, while other cells (not expressing the antigen) flow through by applied hydrodynamic force (pressure driven flow by a syringe pump, for example). This is often also termed as Magnetically Actuated Cell Sorter (MACS), which is a trademark of Miltenyi Biotec GmbH, a company that provides commercial solutions for magnetic cell sorting.

Since the magnetic field is largely permeable to biological tissues and cells, a clear advantage of using a magnetic field is that, it less likely to interfere with cell function or immunochemistry necessary for magnetic labeling. The entire process can be done in solution phase, thus minimizing any physical damage to the cells. This magnetic cell sorting can be normally operated in either batch or continuous flow processing modes. Batch processing involves first the presence of a magnetic field to collect the cells attached to magnetic beads, and then the absence of that magnetic field to collect the accumulated cells. In continuous flow magnetic cell sorting process, one can place a quadrupole magnet besides the microchannel or column. When the sample flow pass

through the channel, cells attached to magnetic beads are deflected in one direction by the applied magnetic field, while other cells that do not have beads attached continue to go straight.

Miltenyi et al. published this method in 1990 on *Ctometry*.[104] In this paper, they states that cells stained sequentially with biotinylated antibodies, fluorochrome-conjugated avidin, and superparamagnetic biotinylated-microparticles (about 100 nm diameter) are separated on high gradient magnetic (HGM) columns. Unlabelled cells pass through the column, while labeled cells are retained. The retained cells can be easily eluted. More than 10^9 cells can be processed in about 15 min. Enrichment rates of more than 100-fold and depletion rates of several 1,000-fold can be achieved. They achieved a relative high throughput for cell separation.

However, the disadvantage of this magnetic cell sorting method is also obvious, antigen-antibody reactions are required for cells to bind to magnetic particles for magnetic based methods, and this method is limited by the specificity of antigen-antibody reaction. If the cell cannot be identified by antigen-antibody reaction, then it cannot be separated from another cells by magnetic based cell separation methods.[105]

1.4.2.1.3 Optical cell sorting

Light has also been used to manipulate and separate particles and cells depending on their optical polarizability, this technique has been widely demonstrated by the popular optical trapping method. One common used light cell trap technique is optical tweezer (or so called “single-beam gradient force trap”). This technique use a highly focused laser beam to provide an attractive or repulsive force (typically on the order of piconewtons),

depending on the refractive index mismatch to physically hold and move microscopic dielectric objects (cells for example).

Guck et al. present a microfluidic optical stretcher, with a two-beam laser trap optimized to serially deform single suspended cells by optically induced surface forces. In their work, they used a focused laser beam to count and sort the cells based on deformability, in a serial manner.[106]

Although this technique is unique in terms of tracking the cells' deformabilty with very minimal preparation/labeling, however the throughput of this technique is still limited compared with FACS. Nevertheless, there is another obvious disadvantage that highly focused laser beam is potentially harmful for the cells, by the heat it generates

1.4.2.1.4 Acoustic cell sorting

By using piezoelectric material, one can induce ultrasonic acoustic resonance (standing waves) within a microchannel, which can produce radiation force to manipulate particles and molecules.

For example, Evander et al. present a microfluidic Perfusion System for Noninvasive Acoustic Cell Trapping and Online Bioassays.[107] In their work, an acoustic standing wave is generated in etched glass channels (600 × 61 μm2) by miniature ultrasonic transducers (550 × 550 × 200 μm3). Particles or cells passing the transducer will be retained and levitated in the center of the channel without any contact with the channel walls. Neural stem cells were acoustically trapped and shown to be viable after 15 min. Additional evidence of the mild cell handling conditions was demonstrated as yeast

cells were successfully cultured for 6 h in the acoustic trap while being perfused by the cell medium at a flow rate of 1 μL/min.

However, due to the nature of the system, materials for the device must be chosen carefully to transmit the acoustic power to the fluid properly, which is the unavoidable disadvantage for this kind of Acoustic cell sorting system.

1.4.2.1.5 Other cell separation and sorting method

In microfluidic channels, various other cell sorting mechanisms have been implemented. For example, size and deformability based cell sorting is realized in pillared structures. By tailoring the dimensions in between pillars, selection of cells based on their size and deformability can be achieved. Huang et al. described a method with separation resolution less than 20 nm of continuous separation based on ‘‘deterministic lateral displacement’’ (DLD) of micron sized particles.[108] This kind of cell sorting method is categorized as “passive cell separation techniques”, since it require no external energy for cell separation. Similar examples including Pinched flow fractionation (PFF),[109] Affinity-based separation,[110] Biomimetic separation,[111] etc.

1.4.2.2 Dielectrophoresis separations

DEP is a phenomenon in which a force is exerted on a dielectric particle when it is subjected to a non-uniform AC electric field. DEP force does not require the particle to be charged. This is due to the fact that when an electric field is applied to systems consisting of particles suspended in a liquid, a dipole moment is induced on the particles, due to the electrical polarizations at the interface between the particle and the suspending

liquid.[112, 113] If the field is non-uniform, the particles experience a translational force (DEP force) of magnitude and polarity, depending not only on the electrical properties of the particles and the medium, but also on the magnitude and frequency of the applied electric field. The polarizability of living cells depends strongly on their composition, morphology, and phenotype and is also highly dependent on the frequency of the applied electrical field.[114, 115] This means that for a given particle type and suspending medium, the particle can experience, at a certain AC frequency applied to the electrodes, a translational force directed towards regions of high electric field strength (this phenomenon is called positive DEP, *i.e.* pDEP). Alternatively, by simply changing the frequency, they may experience a force that will direct the particle away from the high electric field strength regions (this phenomenon is called negative DEP, *i.e.* nDEP).[116]

DEP has been demonstrated for manipulation of biological particles such as cells,[117, 118] bacteria,[119, 120] viruses,[121-124] yeast (*S. cerevisiae*)[125, 126] and even breast cancer cells.[127, 128] The applicability of this technology to colorectal cancer cell separation has, to our knowledge, never been reported.

2. THEORY

2.1 Electrokinetic instability (EKI) mixing

The fluid flows in microfluidic and nanofluidic devices are often stable and strongly damped by viscous forces (with Reynolds numbers of order unity or smaller). However, heterogeneous ionic conductivity fields in the presence of applied electric fields can, under certain conditions, generate an unstable flow field owing to electrokinetic instabilities (EKI). Conductivity gradients are prevalent in on-chip electrokinetic processes such as preconcentration methods (e.g. field amplified sample stacking and isoelectric focusing), multidimensional assays, and systems with poorly specified sample chemistry. The dynamics and periodic morphology of electrokinetic instabilities are similar to other systems with Rayleigh–Taylor instabilities.

Electrokinetic instabilities can be leveraged for rapid mixing or can cause undesirable dispersion in sample injection, separation and stacking. These instabilities are caused by a coupling of electric fields and ionic conductivity gradients that results in an electric body force. This coupling results in an electric body force in the bulk liquid, outside the electric double layer, that can generate temporal, convective, and absolute flow instabilities. Electrokinetic flows with conductivity gradients become unstable when the electroviscous stretching and folding of conductivity interfaces grows faster than the dissipative effect of molecular diffusion.

2.1.1 Brief review of electrokinetic instability

It was first observed EKI in the microfluidic in various laboratories when pursuing electrokinetic applications such as sample loading and injection, and field-amplified sample stacking.[129, 130] In the meantime, a variety of groups also explored the possibility of using this instability for efficient and non-mechanical micro-mixing.[14, 36] Although the instability mechanism was not fully understood, a more systematic investigation by Chen and Santiago (2002) established the critical importance of conductivity gradient and high electric field strength in inducing the instability. Deeper studies by Santiago and co-authors[24, 37] related the instability physics with earlier works on electrohydrodynamic (EHD) instability by Hoburg and Melcher (1976),[131] Hoburg and Melcher (1977)[132] and Baygents and Baldessari (1998)[133]. By combining linear analysis and non-linear numerical simulations, their studies provided a comprehensive model framework for the understanding and prediction of EKI, and the results compared favorably with experimental measurements. A lot of work followed to systematically investigate the instability in greater details, including those on the effects of field alignment,[134] electroosmotic convection (convective and absolute instability),[135] channel dimension,[24] time-periodic forcing[13] and multiple-species;[136] and those implemented EKI in various designs for mixing applications.[137-139] A discussion on two important features helps us relate EKI to proper context and other similar flow phenomena. The first is that EKI is induced by the presence of an electrical conductivity gradient, which under an applied field results in charge separation and an electrical body force (the Maxwell stress). In this regard EKI can be viewed as a special type of EHD flow, the modern theoretical foundation of which

was laid by Melcher and Taylor (1969).[140] However, different than the original leaky-dielectric model, in EKI charge separation occurs in the bulk of a single miscible fluid, not at the interface of two immiscible fluids. Consequently, and as correctly first pointed out by Baygents and Baldessari (1998),[133] ion diffusion in EKI results in a conditional instability. EHD instability of two (or more) immiscible fluids in microfluidic devices is another subject extensively studied by Li et al. (2007),[141] Ozen et al. (2006),[142] and Zahn and Reddy (2006),[143] among others, and is not discussed here. Another feature of EKI is that it is driven by an electrostatic force in the bulk of the liquid away from charged solid–liquid interfaces (and hence away from the electric double layers). This feature distinguishes EKI from other types of instabilities and/or mixing phenomena in electrokinetic flows, such as those induced by modulated electroosmotic flows.[144] In this latter case electrostatic forcing is regarded as absent away from the (often relatively thin) electric double layers.

2.1.2 EKI mixing strategy

The flow configuration is shown in Fig. 2.1. The sidewalls of the channel are made of electrically conducting metal and can be either parallel or non-parallel. x and y denote the position in the streamwise and transverse directions in the main channel respectively.

Two fluids with different electrical conductivity are used for the study. Each fluid enters the microchannel through its own inlet channel. As soon as they meet, a jump in electrical conductivity is generated at the interface between the two fluids. When the electrodes are electrically activated, the fluids entering the influence zone of the electric

field between the pair of facing electrodes, are subjected to an electrical force, which, if its magnitude is sufficiently large, creates a transversal convection (secondary flow) across the interface between the two fluids, thus destabilize the interface and promote the mixing process of the two fluids.

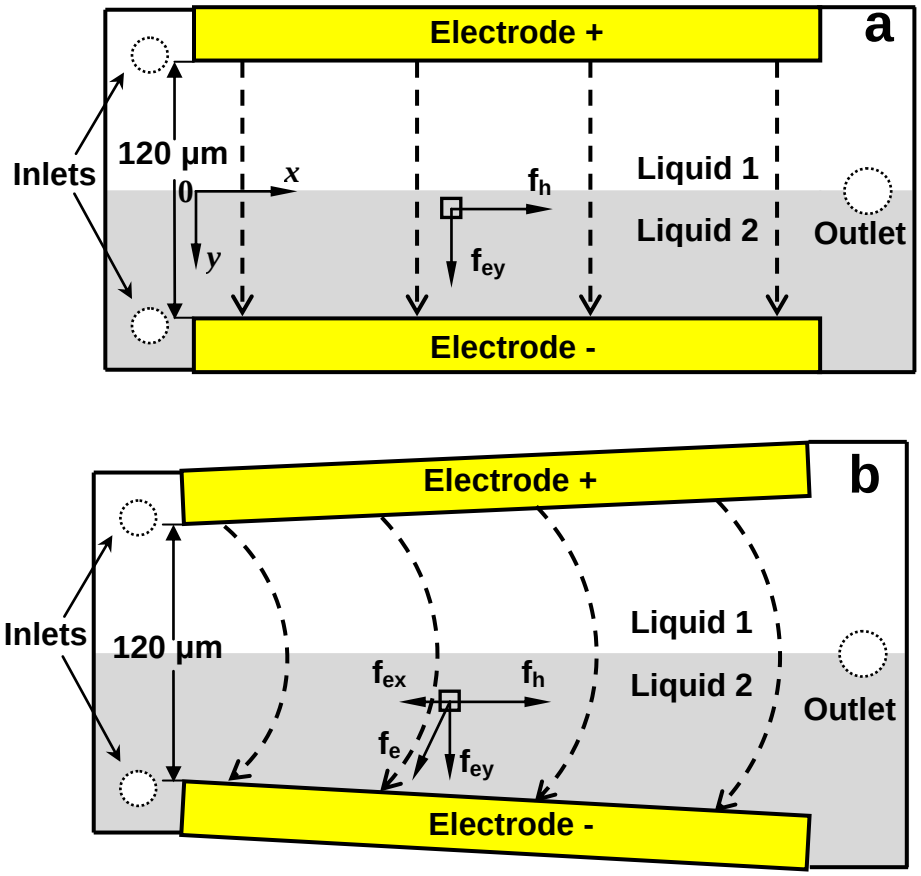

Figure 2.1 Flow, electrodes configuration and force descriptions in the micromixer with comparison of (a) parallel electrodes, and (b) non-parallel electrodes channel.

The principle of turbulent mixing in microfluidics at low Re is described below. With electrokinetics, the Navier-Stokes equation can be described as:

$$\rho\left[\frac{\partial \bar{u}}{\partial t} + \bar{u}\cdot\nabla\bar{u}\right] = -\nabla p + \eta\nabla^2\bar{u} + \bar{f}_e \qquad (2.1)$$

The main driving force in this mixing process is suggested as Coulomb electrical body force $\vec{f}_e$ caused by the action of the electric field $\vec{E}$ on the net charge density ρ_f in solution.[133]

$$\vec{f}_e = \rho_f \vec{E} - \frac{1}{2} E^2 \nabla \varepsilon - \nabla \left(\frac{1}{2} \rho E^2 \left(\frac{\partial \varepsilon}{\partial \rho} \right)_T \right) \tag{2.2}$$

The net charge density in the bulk liquid can be derived from electrostatics theory is expressed as:[24]

$$\rho_f = -\frac{\varepsilon \vec{E} \cdot \vec{\nabla} \sigma}{\sigma} \tag{2.3}$$

where ε is the permittivity of the electrolyte. In this equation, electrical conductivity is not a passive scalar because a change in conductivity will alter the electric field and induce net charge, and the resulting electric body force will change the velocity field.

If the there is no conductivity gradient, which means $\nabla \sigma = 0$, then no net charge will be induced $(\rho_f = 0)$, consequently, no body force on liquid will be generated $(\rho_f \vec{E} = 0)$, then no EKI will occurs.

In pressure driven flows at low Re in microfluidics, usually inertial force ∇p alone cannot surpass viscous force $\eta \nabla^2 u$ to generate turbulence, and the flows should be laminar. To overcome the strong viscous force to generate turbulence, extra inertial force is required. If electrokinetics is involved, we can increase the inertial force $\vec{f}_e$, by increasing ρ_f. It is important to notice that, indicated by the term of $\vec{E} \cdot \vec{\nabla} \sigma$, the charge density could be minimum when the external electric field is perpendicular to the electrical conductivity gradients. In microfluidics, electrodes are commonly placed at the inlet and outlet of the channel to induce electrokinetic instability and to increase mixing in

the flow. In such a kind of micromixer, since $\vec{E}$ is perpendicular to $\vec{\nabla}\sigma$, ρ_f and $\vec{f}_e$ are very small, and the corresponding mixing is achieved by amplifying the original tiny disturbance at the interface between two fluid streams.[24] In contrast, when the external electric field is parallel to the electrical conductivity gradients, the charge density can be maximized, which will result in a maximum electrical force and strongest distortion at the interface of two liquid flows. In our micromixer, the electrodes are directly used to form the side wall, therefore the external electric field is parallel to the electrical conductivity gradients, and a strongest EKI is achieved in our micro mixer.

As the Coulomb force plays a key role in current designed mixing process, we could further introduce a non-uniform electric field, with expectation of generating more chaotically secondary flow perpendicular to the flow direction, dramatically improving the mixing process. The brief design scheme is shown in Fig. 2.1(b).

If the two electrodes are parallel as shown in Fig. 2.1(a), the electric field is approximately uniform inside the mixing chamber. However, if a small angle (e.g. 5°) between the two electrodes is introduced in the micromixer, the electric field could be non-uniform between these two electrodes, as shown in Fig. 2.1(b).

For a small volume in the fluid, the forces it experiences are hydrodynamic force $\vec{f}_h$ and electric field force $\vec{f}_e$, respectively as shown in Fig. 2.1. From equation (2.2), we know that the $\vec{f}_e$ depends mainly on the ρ_f and $\vec{E}$, and its direction is the same as $\vec{E}$. In the rectangular coordinate, the $\vec{E}$ and $\vec{f}_e$ can be write in the term of components in x (stremwise) and y (transverse) direction respectively,

$$\vec{E} = \vec{E}_x + \vec{E}_y \tag{2.4}$$

$$\vec{f}_e = \vec{f}_{ex} + \vec{f}_{ey} \tag{2.5}$$

In the parallel electrodes mode, the direction of $\vec{E}$ is perpendicular to the streamwise direction, therefore, $\vec{E}_x$ is approximately equal to zero. Hence, $\vec{f}_{ex} = 0$. However, in the non-parallel electrodes mode, the direction of $\vec{E}$ is in the tangential direction of each point on the electric field lines, and it changes along the electric field lines. Thus, $\vec{E}_x$ and $\vec{f}_{ex}$ are not equal to zero except the point whose tangential direction is perpendicular to the streamwise direction, in our case, the points on the middle line between the two electrodes. Meanwhile, the strength of $\vec{E}_x$ and $\vec{f}_{ex}$ will increase from the middle towards to the electrodes and reach the maximum at the point infinitely close to the electrodes. As the sum force exerted on the fluid in the x direction is

$$\vec{f}_{sum} = \vec{f}_h + \vec{f}_{ex} \tag{2.6}$$

$\vec{f}_{sum}$ could be enhanced at the points, where $\vec{f}_{ex}$ is positive and be attenuated at the points where $\vec{f}_{ex}$ is negative, assuming hydrodynamic force $\vec{f}_h$ is positive. When $\vec{f}_{ex}$ near the surface of one electrode is in the opposite direction to the hydrodynamic force near the other electrode, the two forces will generate shear stresses and a moment, resulting in a vortex along the spanwise direction, if the electric field strength is sufficiently high as indicated in Fig. 2.1. The vortex could enhance more chaotic flow and efficient mixing.

2.2 Dielectrophoresis based cell separation

Cell separation and sorting are essential steps in cell biology research and in many diagnostic and therapeutic methods. Specially, Non-invasive and low cost screening is

needed for cancer diagnostic. Separation and enrichment of cancer cell (e.g. circulating tumor cells) from other cells could significantly enhance sensitivity and specificity for cancer diagnosis. The need for efficient cell separation has led to the recent development of numerous microscale separation techniques. With the appropriate length scale that matches the scales of cells, microfluidics is widely investigated and contributes significantly to cell separation technology development.

2.2.1 DEP cell separation review

Among all these cell separation methods, dielectrophoresis (DEP) has emerged as a promising method for a variety of engineering applications involving manipulation of micro- and nano-particles.

DEP is a phenomenon in which a force is exerted on a dielectric particle when it is subjected to a non-uniform electric field. It is not necessary for particle to be charged. This is due to the fact that when an electric field is applied to systems consisting of particles suspended in liquid, a dipole moment is induced on the particle, due to the electrical polarization at the interface between the particle and suspending liquid.[112, 113] The DEP force on the particle depends not only on the electrical properties of the particle and the medium, but also on the magnitude and frequency of the applied electric field. The polarizability of living cells depends strongly on their composition, morphology, and phenotype as well as on the frequency of the applied electrical field.[115, 145] This means that for a given type of cell and suspending medium, cells can experience, at a certain alternating current (AC) frequency applied to the electrodes, a translational force which directs the cells to the regions of the highest electric field

strength (this phenomenon is called positive DEP, *i.e*. pDEP). Alternatively, by simply changing the frequency, they may experience a force that will direct them away from the highest electric field strength regions (this phenomenon is called negative DEP, *i.e*. nDEP).

DEP offers advantages of contactless, label free, easy operation and high specificity. In addition, it can be used to manipulate, transport, separate and sort different types of particles [146-148] including biological particles, such as cells,[117, 118, 149-152] bacteria,[119, 120] viruses,[121-124] yeast [125, 126] and even breast cancer cells.[127, 128]

The dielectrophoresis can be easily adopted in integrated microfluidic systems to manipulate, separate particles and cells. In recent years, microfluidics has generated great excitement due to its potential of providing rapid analyses with high resolutions and low costs for a wide range of biological and chemical applications.[93, 95, 97, 110, 153-156] The integrated microfluidic system will play a key role in biochemistry, molecular biology and synthesis protocols,[96] and is expected to have major impacts on biomedical research, clinical diagnosis,[97] point of care, food pathogen screening [98] and environmental monitoring by providing automated and portable solutions to a wide range of fluid based problems.[99-101]

In the United States, colorectal cancer is the second most common cause of cancer death, with approx 130,000 new cases and 55,000 deaths per year.[157, 158] Often if the pre-invasive form of the disease can be detected early, it can be cured and cancer spread can be prevented. Separation of colorectal cancer cells from other biological materials is very important to improving the accuracy and cost-effectiveness of cancer diagnosis.

Prostate cancer is a slow growing tumor but the second-leading cause of cancer death in men.[159] A man's lifetime risk of prostate cancer is one in six, and the chance of death due to this disease is 3.4%,[160] The long latent period of prostate cancer has made early diagnosis possible. Usually if the development of a tumor can be detected early, it can be cured and the spread prevented. Currently, the most common screening methods for prostate cancer are digital rectal examination [161] and serum prostate specific antigen (PSA) testing.[162] Digital rectal examination detects the palpable tumors in the peripheral zone of the prostate. Serum PSA is an FDA-approved biomarker for the early detection of prostate cancer. However, it remains controversial as a marker for population screening due to the lack of enough specificity and sensitivity. Some men may have elevated serum PSA but do not develop lethal prostate cancer. As a result, PSA testing tends to cause over-diagnosis and over treatment.[163] Therefore, developing a simple, fast and accurate method for early cancer diagnostics at a low cost is highly desirable.

Existing of circulating tumor cells (CTCs) in peripheral blood could provide another opportunity for cancer diagnosis and prognosis.[110, 164, 165] The major cause of cancer-associated death is metastasis that involves rare events such as cell dissemination and invasion. Although cell dissemination was thought to be a late step in cancer progression, this concept has recently been seriously challenged. Increasing evidence indicates that tumor cell dissemination and invasion occur at the very early stage of tumor development, even before the tumor can be detected clinically at the primary site.[166] To provide information for locating the origin of the cancerous material, isolation of CTCs from other cells is often required.[167] Since most cancer

cells are epithelia and have common biomarkers, similar size and morphology, separation of the prostate cancer cells from other epithelial cancer cells can be difficult. Thus, to specifically determine which cancer cell exists in the blood sample, separation of different types of cancer cell is crucial. Hence, the major challenges for CTC detection are the enrichment and isolation of rare cancer cells from blood cells and the identification of source of tumor cells.

Several methods have been developed to capture the circulating tumor cells such as immunomagnetic separation.[167] However, this method may lead to a high false positive rate due to the non-specific binding of the antibody. A microchip based CTC capture and detection from whole blood has also been developed.[110, 168] Benefits that microfluidic devices could offer include high specificity, contactless separation process, high efficiency and low cost.[93, 97, 101, 169]

There currently are several methods that can enable separation of different cell types.[170] For prostate cancer cell separation, some methods have been developed, such as PSA based separation methods,[171] prostate-specific membrane antigen (PSMA) based separation methods,[172] size based methods,[155] membrane microfilter device,[173] magnetic based methods,[170] etc. However, these methods face some challenges. Size based methods and membrane microfilter device have the limitation of separating cancer cells from the cells with similar size, such as normal epithelial cells. Antibodies are required for cells to bind to magnetic particles for magnetic based methods, and this method is limited by the specificity of antigen-antibody reaction. If the cell cannot be identified by antigen-antibody reaction, then it cannot be separated from another cells by magnetic based cell separation methods.[105]

Dielectrophoresis (DEP) is one of the most widely used methods to separate different types of cell.[150] Compared with other methods for manipulating biological and non-biological particles in a microfluidic platform, for instance, optophoresis,[174] magnetic,[105] acoustics,[175] and dielectrophoresis, etc.[176] DEP has emerged as a promising label-free method for a variety of engineering applications involving manipulation of micro- and nano-particles.[112, 118, 124, 126-128, 176, 177] DEP manipulation of biological particles such as mammalian cells, [117, 149, 153, 178] bacteria,[119, 120] viruses,[121-124] yeast (*S. cerevisiae*) [125, 126] and even breast cancer cells [127, 128] has already been achieved by researchers.

Compare with other cell separation method/strategy, microfluidic DEP cell sorter provides the advantages of label-free, harmless to bio-particles, continue cell separation/sorting, easy operation, high specificity, high efficiency and high throughput at a low cost. DEP cell sorter can also avoid nonspecific binding and has no moving part to increase system reliability. Specially, compared with devices that use other electrokinetic approaches to move particles, such as electrophoresis or electroosmosis,[179] DEP systems can be easily combined with electronic detection technologies (e.g. resistive and/or capacitive sensing), to give a real fully-electronic lab-on-a-chip.[180] However, surprisingly, to our knowledge, DEP has not been used for prostate cancer separation.

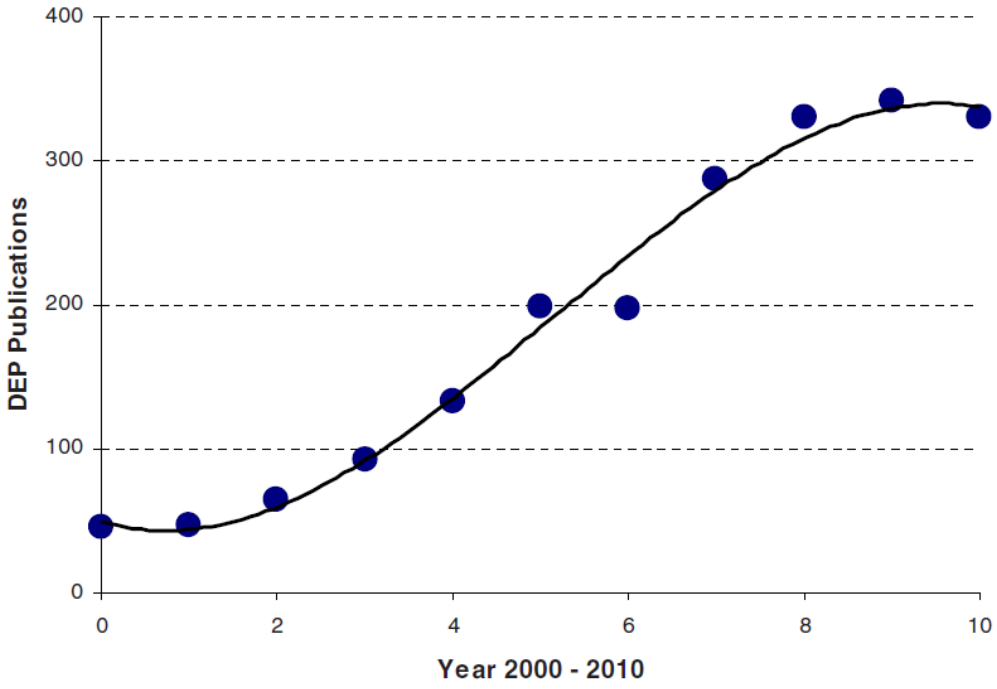

Figure 2.2 Number of publications on DEP for the period 2000–2010.

Since the integration of DEP systems into the microfluidics provides many advantages for detection and analysis of target bioparticles, it has attracted more and more attention of researchers from different area.

There has been a significant increase in the number of DEP publications over the past decade, as shown in Fig. 2.2.[150] A search of databases (MEDLINE, ScienceDirect, Web of Science) generates details of nearly 2000 publications (excluding conference reports and patents) in this field of study over the past 10 years.

In these published papers, various operating strategies have been used for manipulating, separation, isolating cells and bio-particles. The operating strategies can be mainly classified into the following groups: gravitational field-flow-fraction (FFF), lateral sorting, multi-step, barrier-assisted, electrothermal-assisted, travelling wave

dielectrophoresis, multiple frequency dielectrophoresis, pulsed dielectrophoresis, medium conductivity gradient, immuno-assisted sorting, marker-specific, light-induced and electrorotation. Here we briefly introduce some of these mechanisms underlying each DEP strategy.

2.2.1.1 Gravitational FFF

Particles are levitated under the negative DEP force at different heights, where they are carried at different velocities due to the parabolic profile of flow velocity. Therefore, cells leave the channel at different times. When there is sufficient difference in the density or dielectric properties, and the channel is sufficiently long, various particles can be sorted.

For example, Gascoyne et al. present a depFFF tumor cell isolating device.[178] In their work, the application of dielectrophoretic field-flow fractionation (depFFF) to the isolation of circulating tumor cells (CTCs) from clinical blood specimens was studied using simulated cell mixtures of three different cultured tumor cell types with peripheral blood.

2.2.1.2 Lateral sorting

In this kind of lateral sorting designed cell sorting device, under the applied electric field, Particles experience transverse deflection due to the negative DEP force across the channel width. Two different situations occur depending on the relative magnitude of the DEP and drag forces at the electrode tips: at high flow rates, the

particles are focused along the centerline. On the contrast, at a relative low flow rates, the particles are pushed towards the sidewalls.

As a example, Doh et al. a high-throughput continuous cell separation chip using hydrodynamic dielectrophoresis (DEP) process.[176] In this separation process, they used three planar electrodes in a separation channel for the continuous cell separation chip. When electric field applied, the positive DEP cells are moved away from the central streamline while the negative DEP cells remain in the central streamline. In their experiment, viable (live) yeast cells are separated from nonviable (dead) yeast cells. Their fabricated chip performs a continuous separation of the yeast cell mixture at the varying flow-rate in the range of 0.1–1 μl/min; thereby, resulting in the purity ranges of 95.9–97.3 and 64.5–74.3%, respectively

2.2.1.3 Multi-step

In this kind of device, particles are repeatedly trapped and released over the consequent pairs of a long array. Cells or particles move along different parabolic paths according to their different DEP mobility.

Aldaeus et al. present a noval design for separation of particles based on repetitive dielectrophoretic trapping and release in a flow system.[181] Polystyrene beads in deionized water and a micro-flow channel with arrays of interdigited electrodes have been used for separation demonstration. Their result shows that to separate particles with a size difference of 0.2%, about 200 trap-and-release steps would be required.

2.2.1.4 Travelling wave (TWDEP)

A travelling AC field is generated by energising the sequential electrodes with phase-quadrature signals (0 °, 90 °, 180 °, and 270 °, for example). The particles experience a negative DEP force ~Re[f_{CM}] that levitates them, and simultaneously experience a travelling wave DEP force ~Im[f_{CM}] that moves them parallel to the substrate.

Talary et al. demonstrated a multi-layer micro-electrode structure for the selective manipulation and separation of bioparticles using travelling field dielectrophoresis effects. Specially, in the separation process, the selected particles move in a stationary supporting fluid. Stationary suspensions of viable and non-viable yeast cells were used as a model system to demonstrate the general application of this device for the selective retention or transport of bioparticles in suspended mixtures.[182]

2.2.1.5 Multiple frequency

Provided by neighbouring electrodes, particles are exposed to two or more electrical fields of different frequencies. The DEP force is proportional to effective Clausius–Mossotti factor which depends on the frequency as well as the particles' location. This strategy enables the trapping of cells with opposite dielectric responses at the different locations of the system.

For example, Urdaneta et al. present a method of using multiple frequencies to counteract electric field distortions that interfere with the dielectrophoretic (DEP) manipulation of particles or cells.[183] They firstly performed a simulations for a scenario in which cells were to be loaded into a cage whose walls created parasitic trapping sites that prevented cells from entering it. By employing negative DEP on one

electrode in conjunction with positive DEP on another, these traps could be almost completely cancelled.

2.2.1.6 Pulsed DEP

By turning the AC signal on/off with a 50% duty-cycle square wave with a frequency of <10 Hz, which is much lower than the ~10 MHz DEP signal, one can achieve pulsed DEP force. It provides a time-varying DEP force that competes with the constant drag force, under which the particles can be pushed forward or oscillated between two points depending on their dimensions, over successive on–off cycles

Cui et al. present a microfluidic particle-trap array that utilizes negative dielectrophoresis (nDEP) force and hydrodynamic force.[184] The traps are located at the stagnation points of cylindrical pillars arranged in a regular array, and they can function as both single-particle traps (capable of discriminating particles based on size) and multiparticle traps (capable of controlling the number of particles trapped). By adjusting the relative strength of the nDEP and hydrodynamic forces, they are able to control the number of trapped particles accurately. They have used 5 μm polystyrene beads to validate and demonstrate the capability of this new particle-trap design. Pulsed nDEP was used to increase the selectivity and stability.

Above we briefly reviewed some of recently developed DEP based cell/particle manipulation/separation designs. There are many other designs also have been developed by many other researchers. However, according these works, cells are usually considered as a simple single shell particle. To explain this reasonable simplification, here we introduce the common used single shell model.

2.2.2 DEP model of biological particles

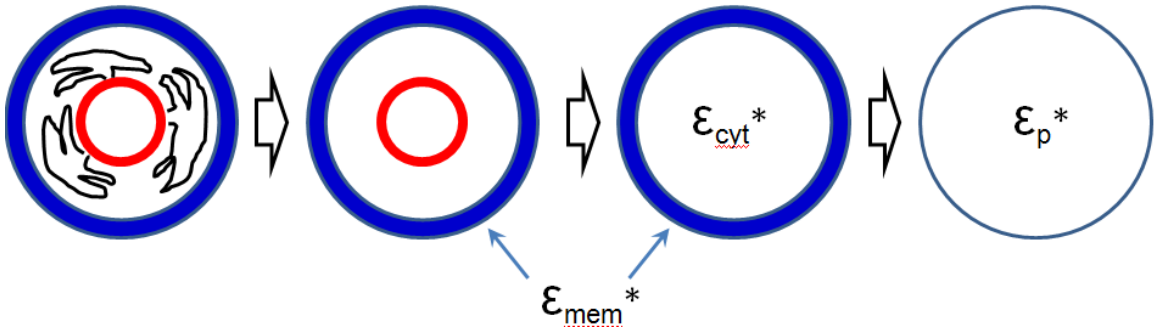

Figure 2.3 A nucleated cell simplified to a homogeneous sphere of effective permittivity ε_p^*, given by Eq. (4). First, the endoplasmic reticulum is represented as a topographical feature that increases the effective capacitance of the nuclear envelope. Second, the cell is represented as a smeared-out cytoplasm surrounded by a membrane of complex permittivities ε_{cyt}^* and ε_{mem}^*, respectively. Finally the cell is represented as a homogeneous sphere surrounded by a thin shell of relative complex permittivity ε_p^*.[150]

For a homogeneous sphere of radius R, the time-averaged DEP force in an AC electric field can be expressed as:[50]

$$\vec{f}_{DEP} = 2\pi R^3 \varepsilon_m \,\mathrm{Re}\left[K(\omega)\right] \nabla \left|\vec{E}_{rms}\right|^2 \tag{2.8}$$

where ε_m is the surrounding media dielectric constant, K is the Clausius-Mossotti factor. $\vec{E}_{rms}$ is the root mean square value of the electric field. The Clausius-Mossotti factor K can be expressed in terms of complex permittivity:

$$K(\omega) = \frac{\varepsilon_p^* - \varepsilon_m^*}{\varepsilon_p^* + 2\varepsilon_m^*} \tag{2.9}$$

$$\varepsilon^* = \varepsilon + \frac{\sigma}{j\omega} \tag{2.10}$$

where ε is the dielectric constant, σ denotes the electrical conductivity, ω is the field frequency, and j is the imaginary number. The subscript p refers to the particles suspended in a medium and m represents the medium.

Generally, most cells are not homogeneous, however, which can be modeled to take account of their heterogeneous structures using the so-called multi-shell model. For instance, erythrocytes are usually discoid in shape, however, they often take the form of a spherical particle when suspended in an electrolyte, and can be represented as a thin spherical membrane (i.e., a single shell) surrounding the cytoplasm. When represent cells such as leukocytes, which possess a nucleus, a three-shell model (first shell the plasma membrane; second shell the cytoplasm; and third shell the membrane envelope surrounding the nucleoplasm) is required. The multi-shell model has been extended to describe nonspherical shells and to account for the dielectric anisotropy of the plasma membrane.

By evaluating effective values for the effective permittivity ε_p^* or conductivity σ_p^* of the cell, the $K(\omega)$ factor for a multi-shell particle can be obtained. The term effective means that a heterogeneous (multi-shell) particle could be replaced conceptually with one having homogeneous smeared-out bulk properties, therefore substitution of one particle with the other would not alter the electric field in the surrounding medium. Fig. 2.3 shows the progressive simplification of a nucleated cell to a simple, homogeneous sphere, and a method for achieving this that employs equations readily adaptable to computer modeling

has been formulated.[185] Thus, we can use the single-shell model on a cell, and its effective complex permittivity is given by[150]

$$\varepsilon_p^* = \varepsilon_{mem}^* \left[\frac{\left(\frac{R}{R-d}\right)^3 + 2\left(\frac{\varepsilon_{cyt}^* - \varepsilon_{mem}^*}{\varepsilon_{cyt}^* + 2\varepsilon_{mem}^*}\right)}{\left(\frac{R}{R-d}\right)^3 - \left(\frac{\varepsilon_{cyt}^* - \varepsilon_{mem}^*}{\varepsilon_{cyt}^* + 2\varepsilon_{mem}^*}\right)} \right] \tag{2.11}$$

in which ε_{mem}^* is the effective permittivity of the plasma membrane, ε_{cyt}^* is the effective permittivity of the cell interior (i.e., the cytoplasm for an erythrocyte), R is the outer radius of the cell, and d is the plasma membrane thickness.

Then From Equation (2.8), we can see that when we apply a constant electric field (constant $\vec{E}_{rms}$, ω) on a constant media (with a constant ε_m^*), the DEP force on different cells will mainly depends on their different R or ε_p^* . By these differences, we can separate different cells by dielectrophoresis associate with additional forces (hydrodynamic force, for example).

There are several possible cellular properties of different cells may result in different R or ε_p^*: cell size and shape,[186] different nuclear-cytoplasmic ratio,[187] different surface charge on cell membrane,[188]and different DNA,[189, 190] etc.

Size effects on Relative DEP response

Fig. 2.4 shows that, the first cross-over frequency f_{xo} is sensitive to the cell size, with all other dielectric factors for cells remaining constant. This result could be explained by that, the cross-over frequency f_{xo} is inversely proportional to the

characteristic time required for the outer cell membrane to fully polarize with its induced accumulation of charge. The bigger the cell, the longer it needs to fully charge the cell membrane using the fixed ion charge density in the suspending medium. A longer period in the time-domain leads to a lower frequency in the frequency-domain. Thus, a large cell will exhibit a lower first cross-over frequency value than a smaller cell.[191]

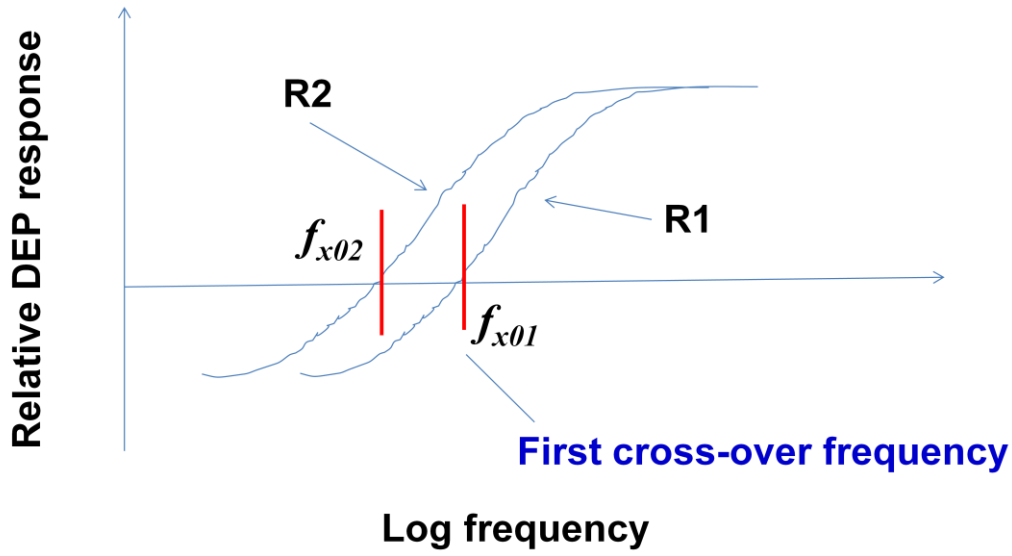

Figure 2.4 DEP response models for different size cells (radius $R2>R1$). The first cross-over frequency f_{xo} is sensitive to cell size, but higher cross-over frequency f_{hxo} is not sensitive to cell size (all other dielectric factors for cells are the same).[150]

Suspending medium's conductivity effects

This result could be explained by that, the relationship between frequency f_{xo}, cell radius R, surrounding electrolyte conductivity σ_m and membrane capacitance C_{mem} is given by:[191]

$$f_{xo} = \frac{\sqrt{2}\sigma_m}{2\pi R C_{mem}} \quad (2.12)$$

This equation indicated that, with all the other factors remaining the same the higher medium conductivity, the higher cross-over frequencies f_{xo}.

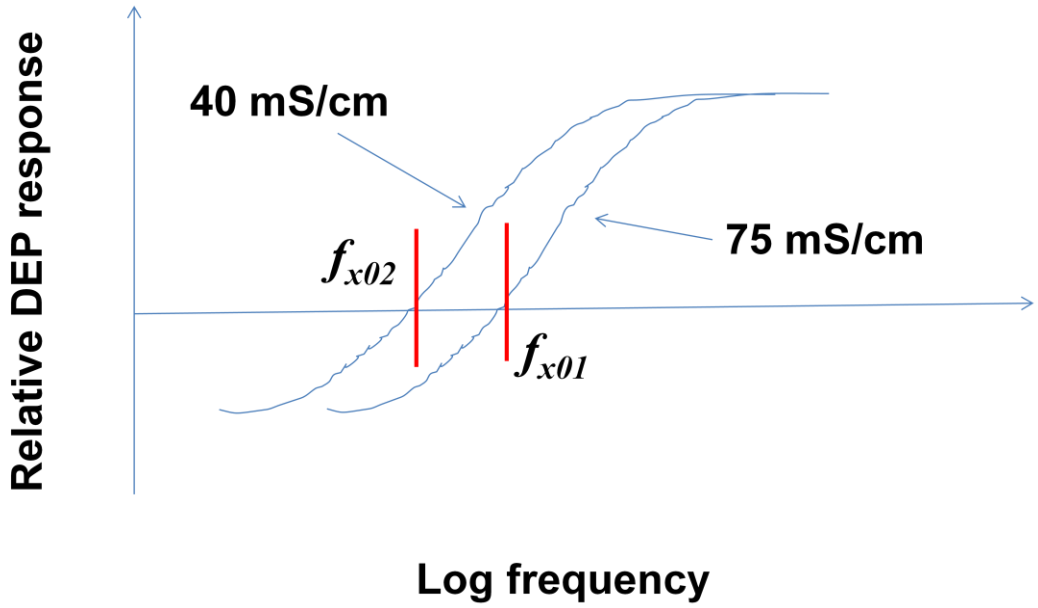

Figure 2.5 DEP response models for a viable cell for different conductivities of the suspending medium. The DEP cross-over frequency f_{xo} increases with increasing medium conductivity, but the higher cross-over frequency f_{hxo} is not sensitive to the medium conductivity.[150]

Surface electric characters (surface capacitance, surface charges)

This result could be predicted by equation (2.12), with all the other factors remaining the same the higher membrane capacitance C_{mem}, the lower cross-over frequencies f_{xo}.

In practical applications, for a fixed cell radius, the effective membrane capacitance of a smooth cell will be less than that for a cell having a complex cell surface topography associated with the presence of microvilli, blebs, membrane folds, or ruffles, for

example.[192] This will influence the value observed for f_{xo1}, and this effect is shown in Fig. 2.6.

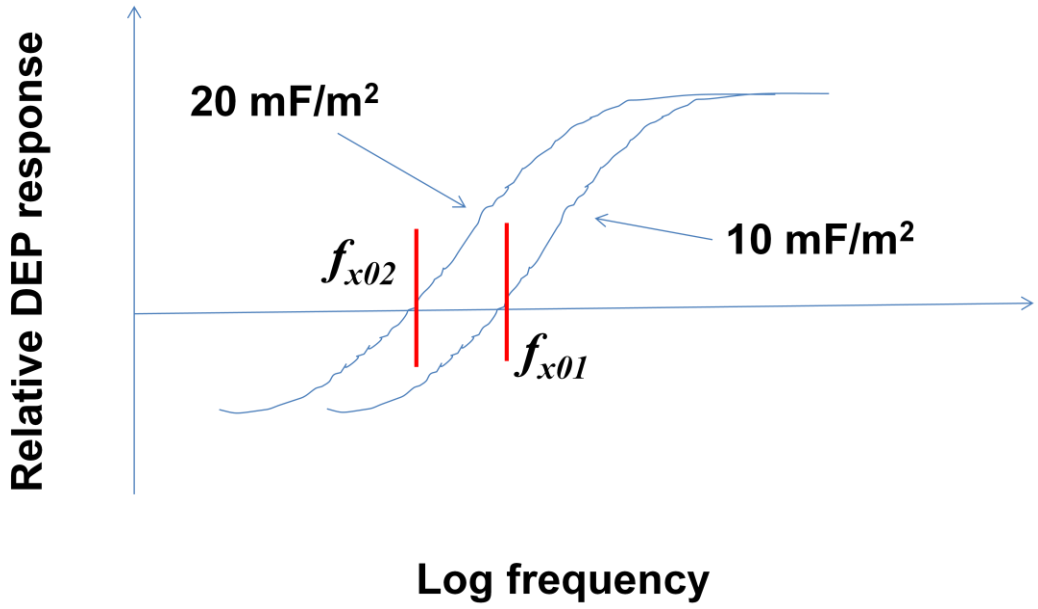

Figure 2.6 different membrane capacitance (surface charges) results in different cross-over frequencies f_{xo}. The first cross-over frequency increases with decreasing membrane capacitance.[191]

Nucleus-cytoplasm (N/C) ratio.

Fig. 2.7 shows a modeling of the effect of changes of the N/C ratio. It indicated that the second cross over frequency is highly influenced by N/C ratio, in a higher frequency domain. This result indicating the fact that the dielectric properties of the nucleoplasm and nuclear envelop are notably different from those of the cytoplasm and cytoplasmic membrane. The dielectric parameters derived by Asami et al. [193] for mouse lymphocytes have been employed in this modeling. The conductivity of the nucleoplasm (1.35 S/m) is modeled to be larger than that of the cytoplasm (0.32 S/m), due to the fact that in general the nucleoplasm has a greater hydrated free ion content than

the cytoplasm. The nuclear envelope is given a large specific conductance value (1.5 × 105 S/m2) to reflect the presence of nuclear pores,[193] whereas the cytoplasmic membrane exhibits a much smaller conductance of ~100 S/m^2.

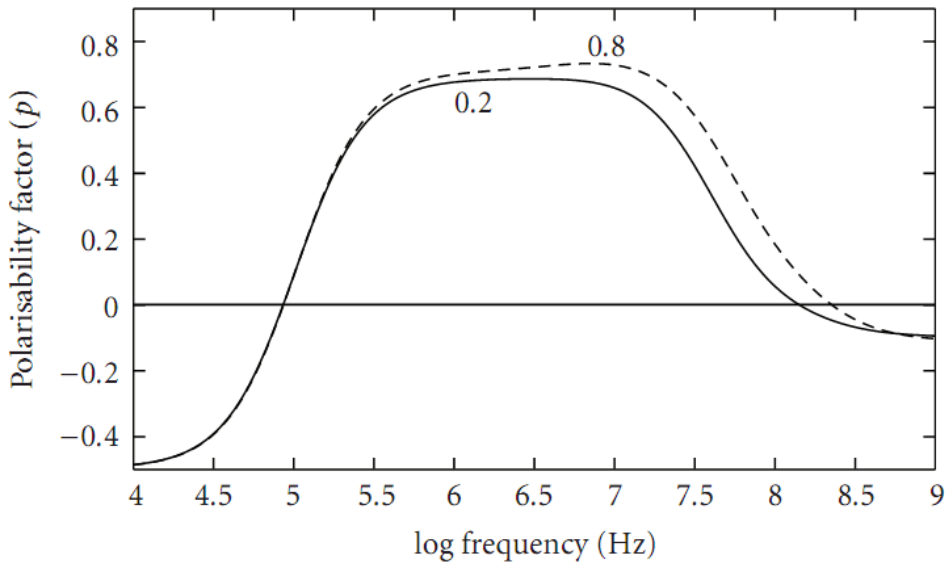

Figure 2.7 Theoretical modeling of the polarisability factor, for different values of the nucleus-cytoplasm (N/C) ratio. The first cross-over frequency is not sensitive to the N/C ratio change, but the higher cross-over frequency increases with the increasing N/C ratio.[191]

2.2.3 Guidance for application of separating similar cells

Here, we report a DEP-based cell sorter capable of continuous cancer cell isolation from other cells. The present device is developed in a microfluidics-based format, which would facilitate ease of integration with current and next-generation lab-on-a-chip system [194, 195] and biodetection platforms.

For the clinical application, usually it is more challenging to separation the colon cancer cells from normal epithelial cells. It is also important to be able to separate cancer cells from bacteria to purify the target sample. For these reasons, we firstly tested our

system by isolating HTC116 colon cancer cells from Human Embryonic Kidney 293 cells (HEK 293) and *Escherichia coli* (*E. coli*) bacterium.

Secondly, DEP separation depends on the cell size and dielectric property. Since most cancer cells have similar size and morphology in solution, distinguishing different types of cancer cell according to their DEF property may have a potential application in isolating and identifying CTCs. We isolate LNCaP prostate cancer cells from other epithelial cancer cells, i.e. HCT 116 colorectal cancer cells as an example to demonstrate that these two types of epithelial cancer cell can be distinguished by DEP microfluidics despite the fact that they have the similar cell size and shape in the solution. Specially, to our knowledge, DEP has not been used for prostate cancer separation.

However, by our cell sorter's nature, this DEP sorter has a limited capability to achieve a high purity of target cells with only one sorter. Furthermore, like all other microfluidics based cell sorters,[110, 155, 171, 172] the microfluidic DEP sorter handles normally only small volume of sample because of the small size of the microchannel, and the enrichment factor decreases with the increased throughput (i.e. flow rate Q). (Note some other DEP based systems have reported significant enrichment/concentration of bioparticles under particular conditions).[196-198] Increasing Q will cause large hydrodynamic force, which can compete with DEP force and reduce the DEP effect for cell separation at high Q.

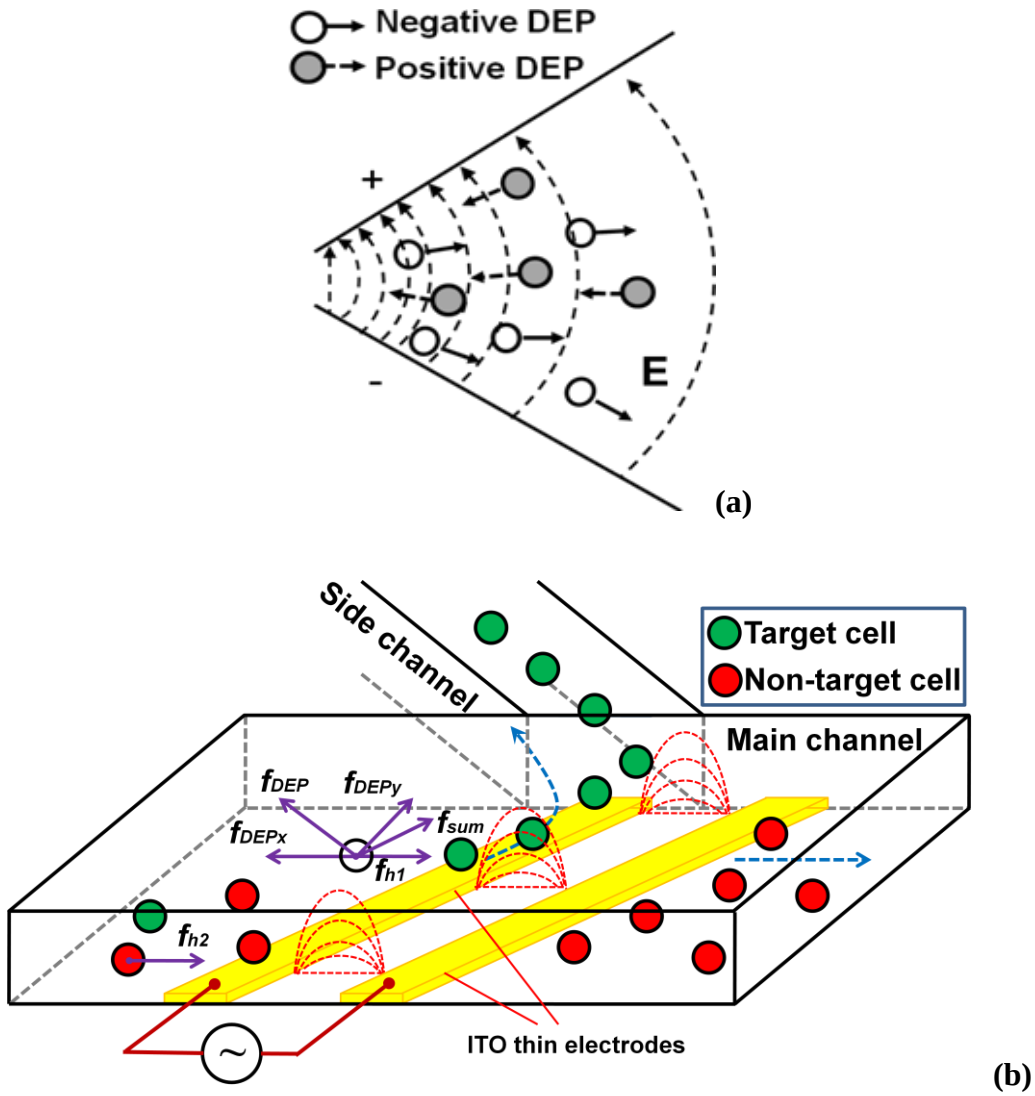

Figure 2.8 (a) DEP force acting on two different particles in a non-uniform electric field. (b)A schematic of a cell suspended in the electric field generated by thin ITO electrodes in the DEP sorter.

In reality, many applications require not only highly purified target cells, but also a high throughput of samples. Hence, in the present work, we introduce a microfluidic cascade DEP sorter to increase the purity of the target cells and a staggered side channel DEP cell sorter to increase throughput without compromising the enrichment factor of cells.

In Fig. 2.8(a), DEP forces acting on two different kinds of particle in a non-uniform electric field. Grey particles are attracted toward the strongest field area. The driven dielectrophoresis force they experience refers to pDEP. Meanwhile, the white particles are directed away from the strongest field region due to their low polarization. The dielectrophoresis force they experience refers to nDEP.

For a homogeneous sphere of radius a, the DEP force is described as:

$$\vec{f}_{DEP} = 2\pi a^3 \varepsilon_0 \varepsilon_m \,\mathrm{Re}\left[K(\omega)\right] \nabla \left|\vec{E}_{rms}\right|^2 \tag{2.13}$$

where ε_0 is the vacuum permittivity, ε_m is the surrounding media dielectric constant, σ denotes the electrical conductivity, $\vec{E}_{rms}$ is the root mean square value of the electric field. The subscript *p* refers to the particles suspended in a medium and *m* represents the medium. $K(\omega)$ is the Clausius-Mossotti (CM) factor.

In many practical systems, at frequencies below 100 kHz, the CM factor can be approximated in terms of the real conductivities:[199]

$$K(\omega) = \frac{\sigma_p - \sigma_m}{\sigma_p + 2\sigma_m} \tag{2.14}$$

pDEP occurs when the polarizability of the particle is larger than the suspending medium (Re[$K(\omega)$]> 1) and the particle moves towards regions of high electric field strength.[200] Negative DEP occurs if the polarizability of the particle is smaller than the suspending medium (Re[$K(\omega)$]<1) and the particles are repelled from regions of high field strength.

Under these low frequency AC electric fields, the DEP force is described as:

$$\vec{f}_{DEP} = 2\pi a^3 \varepsilon_0 \varepsilon_m \,\mathrm{Re}\left[\frac{\sigma_p - \sigma_m}{\sigma_p + 2\sigma_m}\right] \nabla \left|\vec{E}_{rms}\right|^2 \tag{2.15}$$

Under high frequency AC electric fields, dielectrophoresis is under the dielectric regime and the polarization of the particles will be dominated by the differences between the permittivity of the particle and that of the surrounding medium. In dielectric regime, the DEP force is given as:

$$\vec{f}_{DEP} = 2\pi a^3 \varepsilon_0 \varepsilon_m \,\mathrm{Re}\left[\frac{\varepsilon_p - \varepsilon_m}{\varepsilon_p + 2\varepsilon_m}\right] \nabla \left|\vec{E}_{rms}\right|^2 \tag{2.16}$$

Indicated by these equations, the DEP force mainly depends on a particle's radius a, its complex dielectric constant ε_p^*, dielectric constant of surrounding medium ε_m^*, and the electric field $\vec{E}_{rms}$. Based on this, we could predict, when a constant electric field (constant $\vec{E}_{rms}$, ω) is applied to a medium (with a constant ε_m^*), the particles with different a or ε_p^* (i.e. different types of cancer cells in the present work) in this medium, may experience varying magnitudes and directions of DEP force depending on the frequency response of the dielectric permittivity of the particles versus the medium. . Hence, different types of cells will experience different DEP forces under the same electric field. Consequently, selective separation can be achieved by applying an additional force such as gravity or hydrodynamic force by fluid flow.

Based on the aforementioned concept, we have designed a DEP cell separation system, as shown in Fig. 2.8(b). It has a main channel and a side channel on one sidewall. In this design, there are two electrodes on the bottom surface of the microchannel. The electrodes are geometrically parallel to each other and have an angle of 45 degree to the streamwise direction in the main channels, as shown in Fig. 2.8(b). Two AC electric

signals having a phase shift of 180° are applied to both electrodes, The operational principle is as follow. As the target particles driven by the hydrodynamic force approach the electrode pair, they experience a strong negative DEP, which repels them against the hydrodynamic force in the direction with a certain angle to the flow direction in the main channel. The hydrodynamic force is obtained from Stokes equation as:[201]

$$\vec{f}_h = 6\pi\mu\bar{u}a \tag{2.17}$$

where μ is the coefficient of viscosity and $\bar{u}$ is the relative velocity of the fluid with respect to the particle. While most non-target particles will keep their motion to the end of the main channel by the hydrodynamic force f_{h2}, the sum force resulted from DEP f_{DEP} and hydrodynamic force f_{h1} push the target particles (*i.e.* prostate cells) to the side channel, and could be described by equation:

$$\vec{f}_{SUM} = \vec{f}_h + \vec{f}_{DEP} \tag{2.18}$$

Moreover, we can further divide this sum force into x direction and y direction:

$$\vec{f}_{SUM} = \vec{f}_{SUMx} + \vec{f}_{SUMy} = \vec{f}_{hx} + \vec{f}_{hy} + \vec{f}_{DEPx} + \vec{f}_{DEPy} \tag{2.19}$$

We define the sum force along x direction as:

$$\vec{f}_{SUMx} = \vec{f}_{hx} + \vec{f}_{DEPx} \tag{2.20}$$

Fig. 2.8(b), indicates that, when the target cells are experiencing nDEP force, the direction of $\vec{f}_{DEPx}$ which is opposite to the direction of $\vec{f}_{hx}$, and $\vec{f}_{DEPx}$ slows down the target cells moving with the flow. Meanwhile, cells are pushed up by $\vec{f}_{hy}$, to the side channel entrance. On the other hand, when $\vec{f}_{DEPx}$ is not strong enough, cells may be pushed through the electrodes pair by $\vec{f}_{hx}$, before they are pushed into the side channel.

Hence, $\vec{f}_{DEPx}$ has to be sufficiently stronger compared to $\vec{f}_{hx}$. In addition, because the flow direction is along the x direction in our case, therefore, $\vec{f}_{hy}$ could be approximately considered as zero if the cells are sufficiently far away from the entrance of the side wall.

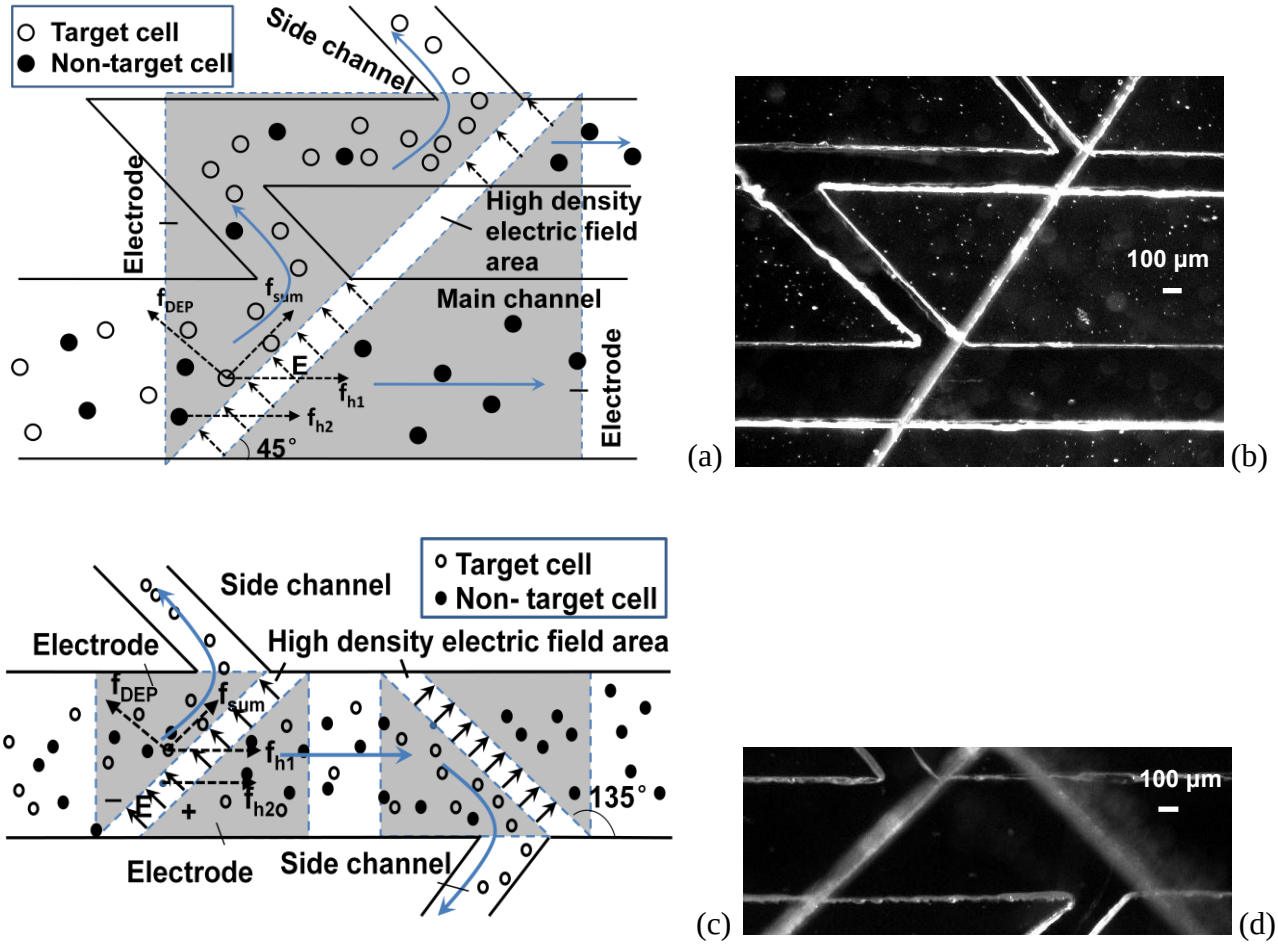

Figure 2.9 Cascade and staggered DEP sorter. (a) Schematic of the cascade DEP cell sorter. (b) Picture of the fabricated cascade DEP cell sorter under a microscope. (c) Schematic of the staggered side channel DEP sorter; (d) Picture of the staggered side channel DEP sorter.

Enrichment factor To quantify the presented DEP sorter performance for the target cell separation and isolation, we define the cell enrichment factor as the ratio of

target particles blocked and flow into the side channel by the nDEP force to the total target particles or cells that flow into the sorter:[198]

$$\eta = A/(A+B) \tag{2.21}$$

where A is the number of the total target cells that are blocked and flow into the side channel, B is the number of total target cells flowed through the gaps in the main channel. η is calculated based on movie obtained from the visualization.

Purity However, the side channel must have a small portion of flow to carry the isolated target cells to a collection well. Thus, there will always be a small portion of non-target cells that follows this portion of fluid and flows into the side channel. This will limit the purity of the target cells isolated in the side channel.[202] The purity P was defined as the ratio of target particles number T collected in the side channel to the total particles number $T + N$, collected in the side channel, where N is the number of non-target particles.

$$P = T/(T+N) \tag{2.22}$$

To avoid this problem, one can make the entrance of side channel as small as possible, but this method has the risk of leading to the block of the side channel. Moreover, this method could also raise the difficulty of the fabrication of the chip. In the present work, we use the cascade configuration to solve this problem. As shown in Fig. 2.9(a), the first side channel is directly connected to the second main channel. Therefore, repelled target cells and a small portion of non-target cells will flow into the second main channel. As there is an electrode pair located at the second main channel with the same gap between them, the target cells will be repelled again by the nDEP force before the second electrode pair, and will move to the second side channel, but the non-target cells will pass over the electrode

pair along the second main channel by the hydrodynamic force. The sorting process is repeated in the second main channel. Consequently, the cells are further purified. Fig. 2.9(b) is a picture of the fabricated cascade chip under a microscope. The fabrication method is given in a previous work.[202]

In a DEP separation process, sample throughput is limited by the strength of the DEP force, i.e. as the throughput increases, the hydrodynamic force will be increased as well, and the percentage of DEP repelled cells will decrease.[203] A straight forward way to solve this problem is to increase the electric field strength, which will enhance the DEP force on the cells. However, high electric field could result in Joule Heating, which is potentially harmful to the cells. It is expected that the targeted cells near the side wall (on the bottom side in Fig. 2.9(c)) opposite to the side channel have to move a longer distance, and thus, need longer time to deflect to the first side channel, than those cells near the side channel do. As cells approach the electrode pair, the cells near the side wall opposite to the side channel are more difficult to be repelled to the side channel. Therefore, they are most likely be pushed to the main channel without being repelled to the first side channel.

In order to solve this problem, we introduce a second DEP sorter downstream the original one along the main channel. In the second DEP sorter, another side channel is designed on the side wall that is opposite to the first side channel, and another electrode pair is placed right downstream the second side channel as the first electrode pair is, but in an angle of approximately 135 ° to the main flow direction, as shown in Fig. 2.9(c). In this case, those cells that are not collected in the first side channel will be collected in the second side channel. As a result, the throughput will be increased without reducing the

enrichment factor. Picture of the fabricated staggered DEP sorter under a microscope is shown in Fig. 2.9(d).

3. EXPERIMENTAL SETUP AND MATERIALS

3.1 EKI Mixing

3.1.1 Experimental setup

Fig. 3.1 shows the schematic of the experimental setup for EKI mixing. The microchip was placed on the test bed of an inverted fluorescent microscope (Olympus-IX70). A syringe pump (Harvard, Model PHD2000 Programmable) was used to pump fluorescent dye solution and water from the inlet ports respectively through the micromixer toward the outlet port. Initial velocity ratio of the two streams was kept 1:1 for all experiments. To study mixing, fluorescein sodium salt ($C_{20}H_{10}Na_2O_5$) and Rhodamine B was used as the fluorescent dye trace for qualitative flow visualization and quantitative concentration measurements. A conductivity meter (EXTECH ISTRUMENTS, ExStik II) was used to measure the solvent conductivity. Specially, conductivity are measured after adding fluorescein sodium into the solvent, therefore, conductivity in total will be not change after measurements. A function generator (Tektronix, Model AFG3102) was used to apply AC electric signal between these two electrodes.

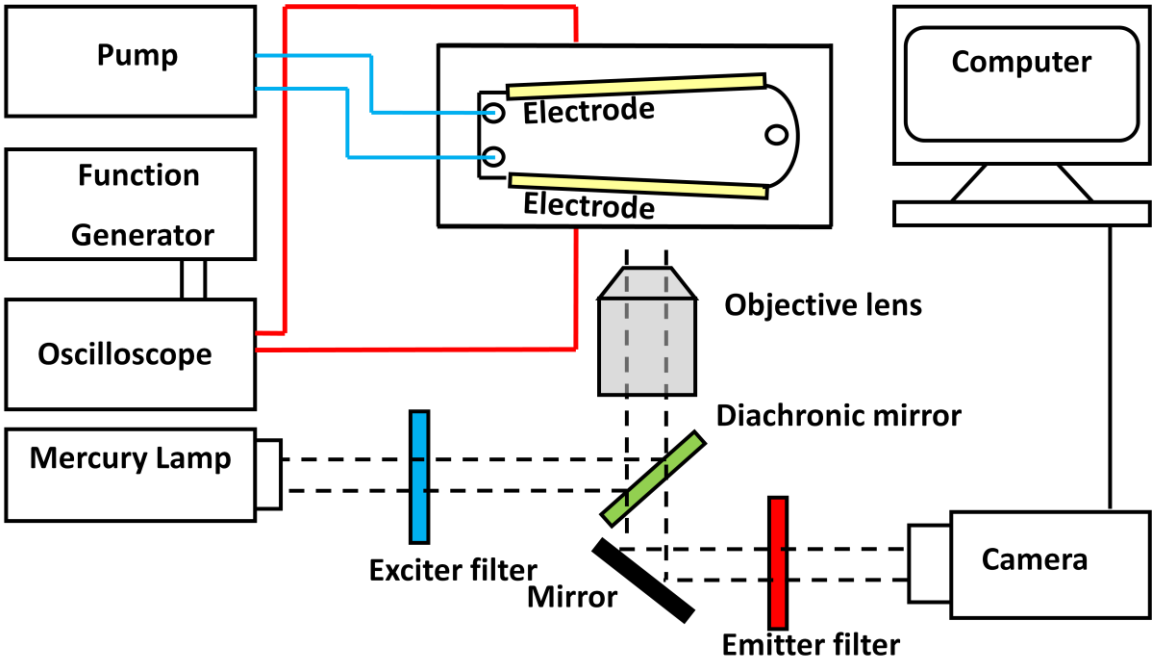

Figure 3.1 Schematic diagram of the experimental setup for EKI mixing.

3.1.2 Fabrication of micromixer

The schematic of the micromixer is given in Fig. 2.1. It is a quasi T-channel made of acrylic plates, gold sheets and gasket. The sidewalls of the microchannel, which can be parallel or non-parallel with an angle, consisted of two gold sheets between the acrylic plates. The parallel mixing channel had a rectangular cross section of 120 μm in width and 230 μm in height, with the length of 5 mm. There were two inlets and one outlet. The diameter of both inlet and outlet holes was 1 mm.

To investigate the effect of non-uniform electric field in axial direction on mixing, we changed the geometry of the microchannel by designing quasi T- channels with non-parallel sidewalls. In this case, the only change was the angle between the two gold electrodes. Fig. 2.1(b) shows an example of the non-paprallel microchannel with an angle

of 5 ° between the two sidewalls. The width of the microchannel at the entrance was kept the same, i.e. 120 μm, for both the parallel and non-parallel microchannels.

Instead of fluorescent dye, fluorescent particles of 1 μm in diameter in one of the two streams was also prepared, in order to visualize the flow pattern more clearly for the understanding of the mixing enhancement mechanism. Green light was used to excite the red fluorescence particles.

3.1.3 Measurement

3.1.3.1 Concentration measurement by LIF

A mercury lamp was used as the illumination source in the present study. Passing through an epi-fluorescent cube, the bright light from the mercury lamp went through a filter and was used to excite the fluorescent dyed solution in the microchannel. Upon excitation, the fluorescent solution would emit fluorescence with its emission peak at about 550 nm. A 10X objective lens (NA = 0.25) was used for the fluorescence imaging. The fluorescence signal was captured by a sensitive and high-resolution CCD camera (SensiCam-QE, Cooke Corp). The concentration was quantitatively determined by measuring the fluorescence intensity within each pixel of the camera using the software analytical tools (MATLAB, MathWorks Inc.). The concentration was proximately proportional to the fluorescence intensity, which was normalized by the maximum value among all pixels along a transverse line at each streamwise position. Hence, the concentration was in the range from 0 to 1. Mixing was measured and compared based on visualization qualitatively and concentration profiles of the fluorescent dye quantitatively

along a transverse line that is perpendicular to flow direction of the microchannel at a given streamwise position.

For the scalar turbulence measurement, a self-developed cw laser based confocal LIF system was used for measurement. UV laser (405 nm in wavelength for excitation) was used to excite the Coumarin 102 dye solution. The fluorescent signal was captured by a photomultiplier tube (HAMAMATSU R928). The focused laser beam was, as the spatial resolution, estimated to be approximately 200 nm. The temporal resolution of the system is measured to be about 10 μs.

3.1.3.2 Turbulence velocity measurement by LIFPA

3.1.3.2.1 Review of other fluid velocimetries

There are many excellent velocimetries in fluid dynamics, but they all have difficulties to measure turbulence in microfluidics. Classical micro Particle Imaging Velocimetries (μPIV)[204] could have difficulty in measuring statistical property of turbulence having high frequency signal, e.g. about 2 kHz in the present work (see Fig. 4.9). Laser Doppler Velocimeter (LDV)[205] suffers from spatial resolution (~ 200 nm is required for present study) and hot-wire anemometer[206] is invasive and difficult to use in microfluidics for point measurement away from walls. Other molecular tag velocimetries[207] also have low temporal resolution. Since turbulent flows have multiscale structures, velocimeter with ultrahigh spatiotemporal resolution is required in microfluidics. To overcome these issues, we developed a molecular tracer based confocal submicroscopic velocimeter, i.e. Laser Induced Fluorescence Photobleaching

Anemometer (LIFPA)[208, 209] to measure flow velocity with unprecedented ultrahigh spatiotemporal resolution in this work. The principle of LIFPA is similar to that of a hot-wire anemometer, but is a noninvasive optical method. Relevant data of the LIFPA for present work is given in supplementary material.

3.1.3.2.2 Principle of Laser induced fluorescence photobleaching anemometer (LIFPA)

The mixing process was also measured by laser induced fluorescence photobleaching anemometer (LIFPA). LIFPA is based on a simplified model illustrating the relationship between fluorescence intensity I_f and fluid velocity u for a given dye concentration due to LIFP. In this model, when the bleaching time t is approximated as the dye residence time within the laser beam of the detection point, I_f increases with u, i.e.

$$I_f = I_{f0} e^{-t/\tau} = I_{f0} e^{-d_f/(u\tau)} \tag{4.1}$$

where I_{f0} represents I_f at t = 0, τ denotes photobleaching time constant, e.g., half decay time, d_f, is beam width. In reality, τ as a system parameter depends on laser wave-length and intensity at the detection point, type of dye and buffer, etc. For a given bleaching time, the smaller τ, the lower I_f. Thus, lower τ causes faster bleaching, and higher dI_f/dt, i.e., higher temporal resolution. τ decreases with reduced laser wavelength and increased laser intensity. The parameter τ can be determined through experiment.

It is important to note that, at the detection point, molecular diffusion will cause fluorescence recovery of the bleached dye molecules. However, unlike some of other photobleaching-based velociometers, LIFPA here does not measure the recovery. In LIFPA, a calibration curve between u and I_f is measured first, if quantitative measurement of u is required. In this case, the recovery effect has already been included

in the calibration relation. This is the main reason why LIFPA has high temporal resolution.

3.1.3.2.3 Current LIFPA velocity measurement

For the current LIFPA velocity measurement, a self-developed cw laser based confocal LIFPA system was used for measurement. UV laser (405 nm in wavelength for excitation) was used to excite the Coumarin 102 dye solution. The fluorescent signal was captured by a photomultiplier tube (HAMAMATSU R928). The focused laser beam was, as the spatial resolution, estimated to be approximately 200 nm. The temporal resolution of the system is measured to be about 10 μs. Since LIPFA is very similar to Hotwire anemometer, but a non-invasive with ultrahigh spatial resolution, we can use data processing method used in hotwire for the LIPFA. Apparently if the flow is not one dimensional, the measured signal should be the norm of two components of velocity, i.e. u (streamwise component) and v (transverse component). This will not significantly affect the statistical analysis of the measured velocity for demonstration that the flow is turbulence.

Since the transient velocity fluctuation can have high frequency in the order of 1000 Hz, high temporal resolution is required for LIFPA, in order to ensure that the high frequency single will not be lost. The rise time of DC electroosmotic flow (EOF) is measured to validate the ultrafast time resolution of LIFPA, since this is one of the most basic transient electrokinetic flows and a very fast dynamic process. This detailed results are given in Appendix 4.

3.2 DEP cell separations

3.2.1 Experimental setup

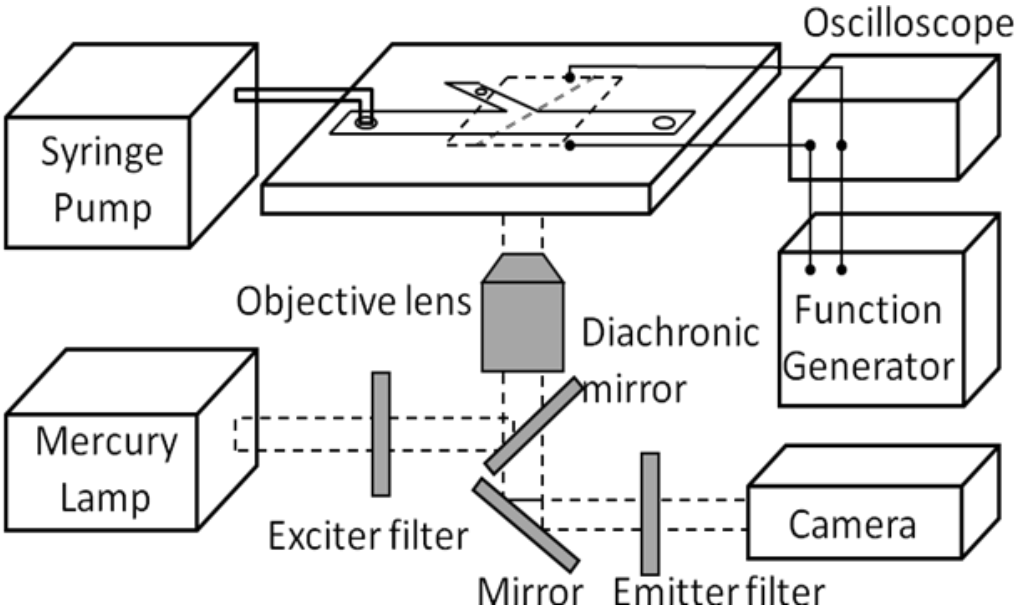

Figure 3.2 Schematic of the experimental setup for cell separation.

A schematic of the setup used for the DEP separation is shown in Fig. 3.2. The DEP cell sorter was placed on the test bed of an inverted epi-fluorescent microscope (Olympus-IX70). A syringe pump (Harvard PHD 2000) was used to deliver the sample to the chip, and the flow rate was kept between 0.1μL/min to 0.8 μL/min in our experiments. A function generator (Tektronix, Model AFG3102) was used to supply AC electrical signal to these two ITO electrodes. In our experiments, amplitude of applied AC signal was kept between 0 $V_{p\text{-}p}$ to 20 $V_{p\text{-}p}$. A 10X objective lens (NA = 0.25) was used for magnification of the imaging. UV light (350 nm in wavelength) was used to excite the

labeled cells. The cell motion was captured by a high-resolution CCD camera (SensiCam-QE, Cooke Corp).

3.2.2 Sample preparation

3.2.2.1 Sample for the separation of HCT116 cells from HEK293 cells and *E. coli.*

The human colorectal cancer cell line HTC116 was used for the experiments. For the clinical application, usually it is more challenging to separation the colon cancer cells from normal epithelial cells. It is also important to be able to separate cancer cells from bacteria to purify the target sample. Furthermore, DEP force depends on particle size and its dielectric property, and separation of the same size, but different dielectric property could often be more challenging. For these reasons, we tested our system by mixing HTC116 colon cancer cells with Human Embryonic Kidney 293 cells (HEK 293) and *Escherichia coli* (*E. coli*) bacterium. Both HCT 116 cells and HEK 293 cells have almost the same diameter of about 20 μm. It is difficult to discriminate between the HCT 116 cells and HEK 293 cells under microscope. To be able to distinguish cells with visualization under the microscope, we labeled the kidney cells with dye Hoechst 33342. The *E. coli* cells are typically rod-shaped and are about 2 μm long and 0.5 μm in diameter, and are much smaller then HCT 116 cells. Then these three kinds of cells were mixed in a Phosphate-buffered saline (PBS) buffer (P0195 - PBS Solution, TEKnova, Inc.), and the medium's conductivity was 790 μs/cm.

3.2.2.2 Sample for the separation of LNCaP cancer cells from HCT116 cells.

The human prostate cancer cell line LNCaP (ATCC) was used as the separation target. LNCaP cells are androgen-sensitive human prostate adenocarcinoma cells. They are adherent epithelial cells growing in aggregates.[210] Human colorectal cancer cell line HCT 116 (ATCC) was selected for LNCap separation. Both LNCaP and HCT 116 cells were in the shape of sphere in suspension and have almost the same diameters of about 20 μm.[211] Equation (2.8) indicates that the DEP force is highly affected by the radius of the cells, therefore this could be more challenge and difficult to separate these two types of cell. If we could separate these two types of cell, it would be more convincing that the technique could have a high potential to isolate prostate cancer cells from other cancer cells and normal epithelial cells. We mixed LNCaP cells with HCT116 cells, in a phosphate-buffered saline (PBS, TEKnova, Inc.) solution, with approximately the same concentration of 1.5×10^6 cells/ml. To distinguish LNCaP from HCT 116 cells under a microscope, we labeled HCT116 colorectal cancer cells with dye Hoechst 33342 (Invitrogen), whose peak absorption and emission are around 350 and 461 nm, respectively).[212] After labeling, cells would emit fluorescence when excited by UV light. Particularly, the labeling of HCT 116 is only for observation of the separation process. In real applications, the HCT 116 cells are not necessary to be labeled. Our test indicated that at the frequency of 2.5 MHz used for the DEP separation, the labeling did not change the DEP behavior of HCT 116 very much, which could be seen in following DEP spectra. In this work, different concentrations of PBS buffer were used to control medium conductivity.

3.2.2.3 Sample for the cascade and staggered DEP sorter

To demonstrate the feasibility of these two types of DEP sorters, two kinds of fluorescent particles with different sizes were used in the experiments. Diameters of the particles were 6 μm (Fluoresbrite® YO Carboxylate Microspheres), with wavelength of excitation max of 529 nm and emission max 546 nm and 3 μm (Fluoresbrite® YG Carboxylate Microspheres), with wavelength of excitation max of 441 nm and emission max 486 nm, respectively. Both kinds of the particles were mixed in DI water with approximately the same concentration of 2.0×10^7 particles/ml. Conductivity and pH of DI water were about 2 μS/cm and 7, respectively. Under a microscope, 3-μm particles were seen as the small dark spheres, and 6-μm particles as large bright spheres.

Two types of biological cells were selected for demonstration of capability of separation of different biological cells separation. A human prostate cancer cell line LNCaP (ATCC^{TM}) was used as the target cells to be separated from a human colorectal cancer cell line HCT116 (ATCC^{TM}). To distinguish LNCaP from HCT 116 cells under microscope, we labeled HCT 116 cells with dye Hoechst 33342 (InvitrogenTM, whose peaks of absorption and emission are around 350 and 461 nm, respectively).[212] Thus, under a microscope, the LNCaP cells were seen as dark spheres, and the HCT116 cells as bright spheres. Both types of the cells were mixed in a suspending medium, Phosphate-buffered saline (PBS) buffer (TEKnova, Inc.) with approximately the same concentration of 1.5×10^6 cells/ml. The conductivity of the medium was 3000 μS/cm.

3.2.3 Microfabrication of microfluidic cell sorter

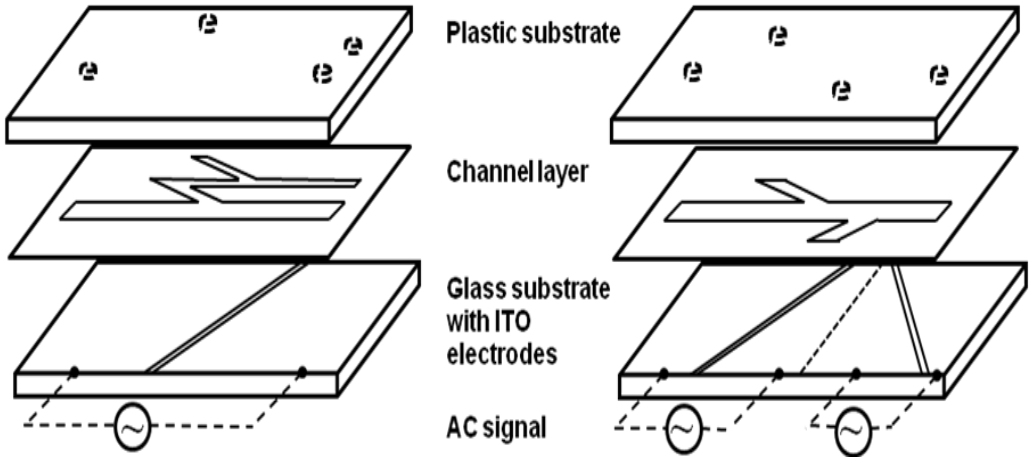

Figure 3.3 Schematic of layered DEP sorter. Inlet and outlet wells are drilled on the top layer. Main and side channels are formed on a middle layer. A pair of indium tin oxide (ITO) thin film electrodes is placed on the bottom of the channel with a gap, these layers are bonded together by pressure sensitive adhesive.

A brief structure description of the microfluidic DEP sorter is shown in Fig. 3.3. The separation chip was made using plastic lamination based microfabrication.[213] The benefits of using lamination techniques to build complex, three dimensional devices include the use of a variety of inexpensive, high quality, bio-compatible materials that easily accommodate the incorporation of other planar structures.[214] Two transparent acrylic plastic substrates of 24 mm x 20 mm x 1.25 mm were used as top (cap) and bottom layer respectively. Inlet and outlet wells are drilled on the top layer. The diameter of all the wells is 1/16 inch. Main and side channels are formed on a middle layer, with the same height of 40 μm. For the cascade cell sorter, widths of the first and second main channel are 550 μm and 300 μm, respectively. The width of side channel is 150 μm. For staggered side channel cell sorter, the main channel width is 600 μm, the side channels' width is 260 μm. A pair of indium tin oxide (ITO) thin film electrodes is placed on the bottom of the channel with a gap of 20 μm. The transparent ITO is 5 μm in thickness and

consists of indium (III) oxide (In_2O_3), tin (IV) oxide (SnO_2), typically 90% In_2O_3, and 10% SnO_2 by weight. We use pressure sensitive adhesive to bind these layers together. The chip is optically transparent to ensure the visualization of the cell motion.

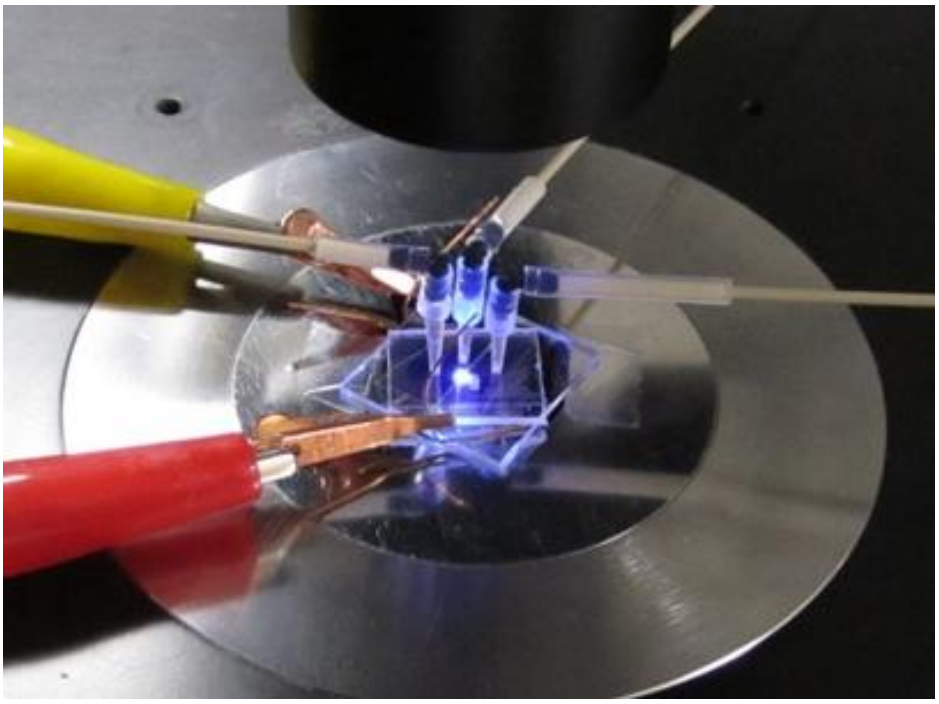

Figure 3.4 Cancer cell separation chip lies beside a standard AA battery on the test bed of a microscope. Tubing is used to connect the inlet of the chip to a syringe pump and the other two outlets to reservoirs respectively.

Fig. 3.4 shows the actual microfluidics DEP sorter we have fabricated. The sorter lies beside a standard AA battery on the test bed of a microscope. Tubing is used to connect the inlet of the chip to a syringe pump and the other two outlets to reservoirs respectively. Two cuprum electrodes have been used to connect the ITO electrodes inside the DEP sorter for applying electric signal on both of them.

4 EXPERIMENTAL RESULTS

4.1 EKI mixing

4.1.1 Characterization of μEKF turbulence velocity by LIFPA

4.1.1.1 Fast diffusion

Fig. 4.1 shows the fast diffusion capability without and with AC forcing, when Re (Re = *UD/v*, where *U* is bulk flow velocity, *D* is the hydraulic diameter and *v* is the kinematic viscosity) at the entrance is 0.4 without forcing. Fig. 4.1(b) is the case without forcing, and the top and bottom stream is buffer solution and fluorescent dye solution, respectively. Clearly, the flow is laminar and there is almost no mixing except for the negligible molecular diffusion at the interface between the two streams. With forcing at 8 $V_{p\text{-}p}$, mixing is decidedly enhanced, but not as dramatically as shown in Fig. 4.1(c). However, at V = 20 $V_{p\text{-}p}$, the mixing becomes extraordinarily fast even near the entrance, as shown in Fig. 4.1(d), where the mixing is so rapid that the visualization cannot display the corresponding detailed kinematic process. Apparently this indicates that there are relatively strong disturbances and vortex motions in the flow, which cause large convection in the transverse direction between the two electrodes. Note in Fig. 4.1(d) that there is no mixing at all a little upstream of the trailing edge. Hence, the flow under goes

a sudden transition from laminar to turbulent motion once the two streams converge. After merely 65 μm downstream of the entrance, the concentration almost becomes uniform (at least on a "large scale") in the entire *y* direction. The mixing time under forcing is estimated to be 33 ms, about 10^3 times faster compared to mixing only by molecular diffusion in the unforced case. Normally, such a rapid mixing only happens in turbulence. Since one feature of turbulence is that there are vortices of different sizes, polystyrene particles were also used as tracers to visualize the corresponding vortex motion of Fig. 4.1(b) and 1d as shown in Fig. 4.1(e) and (f). Clearly there are vortices of different sizes in Fig. 4.1(f), which correspond to the flow of Fig. 4.1(d).

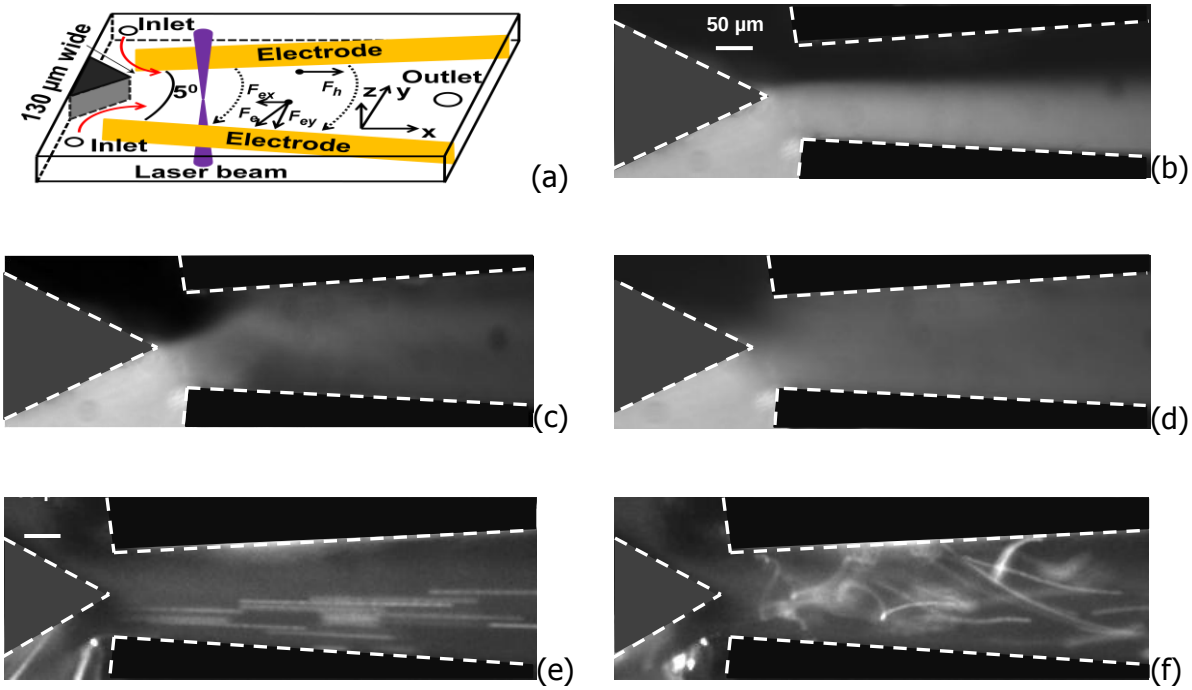

Figure 4.1 Visualization of diffusion process using Laser-Induced Fluorescence. (a) Setup of the microfluidic chip. AC electric voltage is supplied to the conductive sidewalls to force the flow. (b) Flow without forcing. The top flow stream is pure buffer solution and the bottom stream is a dye solution. The flow is laminar, and there is almost no mixing except for negligible molecular diffusion at the interface between the two streams. (c) Forcing under 8 $V_{p\text{-}p}$. The flow is stirred and the diffusion process is partially enhanced.

(d) The flow becomes turbulent, and the diffusion is dramatically enhanced when forced at 20 $V_{p\text{-}p}$. (e) Visualization of the flow (b) with polystyrene particles of 1 μm in diameter. The particles are premixed with only one stream (the bottom one). Straight pathlines in (e) indicates the flow is laminar. (f) The corresponding violent vortex motion of the particles with various sizes of vortices for the flow of (d). The curved pathlines display the random vortices in the flow. The camera exposure time was 0.1 s. Turbulent diffusion in (d) is significantly enhanced due to the vortices shown in (f).

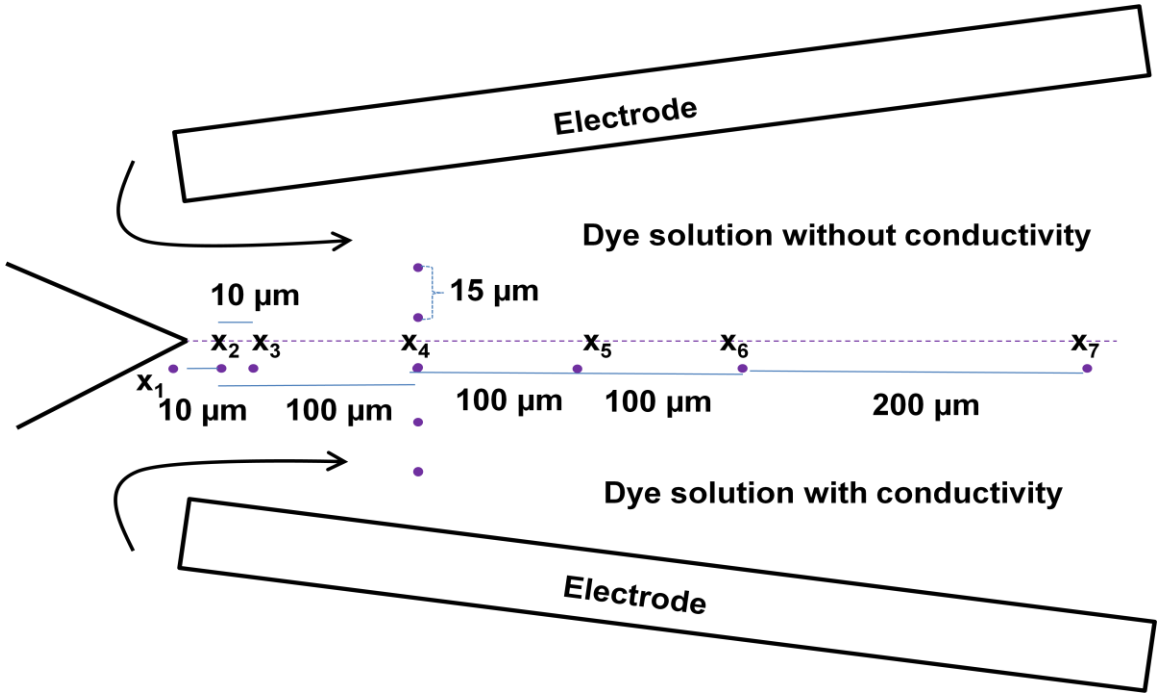

Figure 4.2 The detection positions inside the microchannel. The measuring positions along streamwise direction relative to the entrance are, x_1 = -5 μm, x_2 = 5 μm, x_3 = 10 μm, x_4 = 100 μm, x_5 = 200 μm, x_6 = 300 μm, and x_7=500 μm, respectively. The measuring positions along transverse direction at two different z (spanwise) positions at x_4, for the 3D-flow measurement.

4.1.1.2 High dissipation

A high turbulent diffusion rate normally is accompanied with high turbulent dissipation caused by viscous shear stresses at small scales. In macroflows, right beyond Re_c, the turbulent dissipation (or pressure drop) will start to increase rapidly and nonlinearly. Since turbulent kinetic energy eventually will be dissipated, we used the

velocity fluctuation square as turbulent energy $e = \langle {u_s}'^2 \rangle$ (which is easy to measure) to represent the dissipation feature qualitatively, where $u_s = \sqrt{u^2 + v^2}$ is the instantaneous velocity measured by LIFPA, *u* and *v* are the instantaneous velocity components in the *x* and *y* direction respectively. The prime means velocity fluctuations, and "< >" indicates ensemble averaging. Since here it is the electrokinetic force that causes the turbulence and corresponding high dissipation, we use the relationship between *e* and voltage *V* to describe the feature of the dissipation in the flow as shown in Fig. 4.3(a). The critical *V* is about 6-8 $V_{p\text{-}p}$, below which, *e* increases slowly from 1.2×10^{-10} m^2/s^2 to 1.6×10^{-10} m^2/s^2 (negligible due to laminar flow), i.e. increases about 1.4 times when *V* is increased from 0 $V_{p\text{-}p}$ to 4 $V_{p\text{-}p}$. However, beyond the critical point, *e* increases much faster from 2×10^{-7} m^2/s^2 to 1.6×10^{-6} m^2/s^2, i.e. about 8 times, as *e* increases also 4 $V_{p\text{-}p}$ from 16 $V_{p\text{-}p}$ to 20 $V_{p\text{-}p}$. The relation between *e* and *V* is very similar to the relation between pressure drop and Re around the transitional regime. In general, Fig. 4.3(a) indicates that, similar to macroflows, as V is increased, the electrokinetically-forced microflow also has a dramatically nonlinear increase in dissipation in the turbulent flow compared with that of the laminar flow. Fig. 4.3(a) shows the typical high dissipation feature of turbulence at $V = 20$ $V_{p\text{-}p}$.

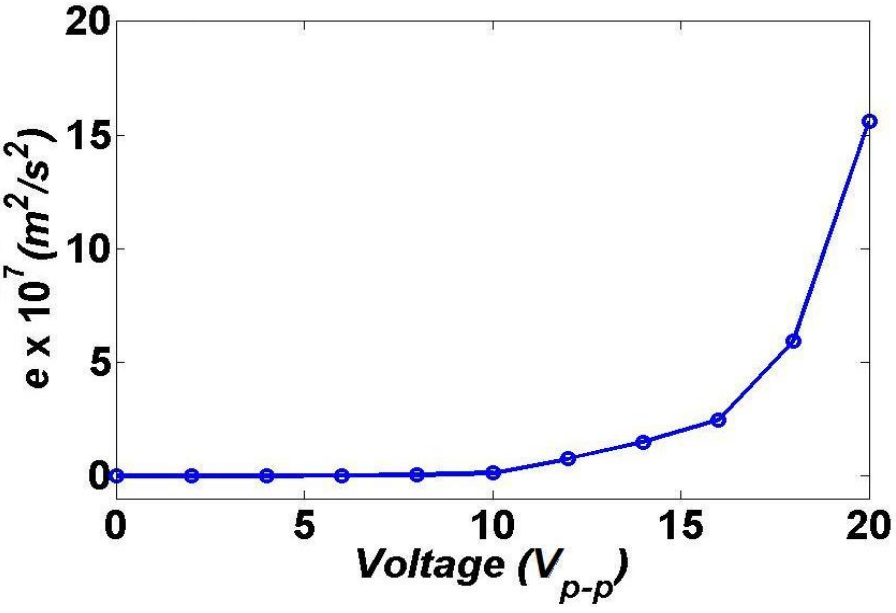

(a)

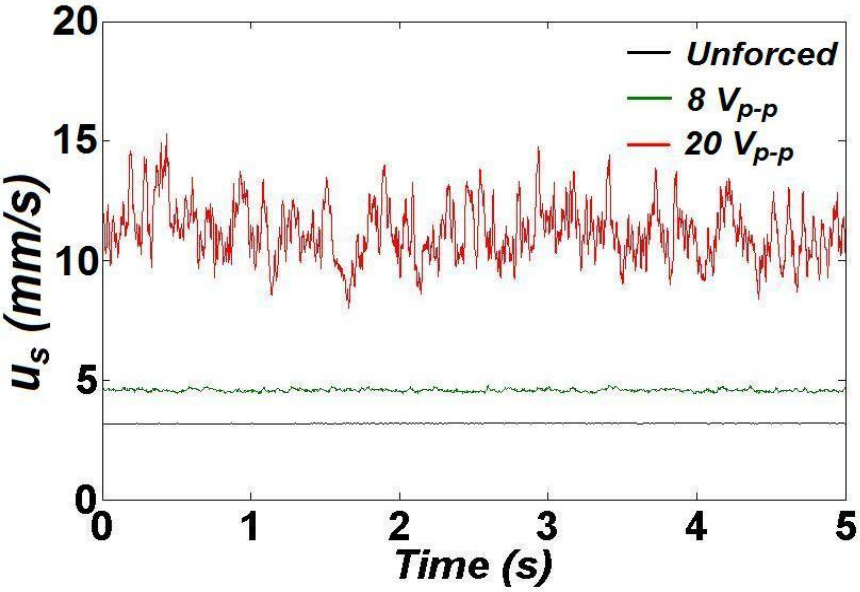

(b)

Figure 4.3 (a) Relationship between turbulence energy e (as a surrogate of dissipation rate) and applied AC voltage V. Compared with laminar flow when V is lower than 8 $V_{p\text{-}p}$, turbulent energy e is radically increased at V = 20 $V_{p\text{-}p}$. e was measured at y = 0, z = 0 and x = 100 μm. (b) Time trace of instantaneous flow velocity u_s at position x_4 = 100 μm. Apparently, strong and random velocity fluctuation can be found at 20 $V_{p\text{-}p}$, for which, based on the measured calibration curve between flow velocity and fluorescence intensity, the measured mean velocity is about 11.2 mm/s, i.e. 5.3 times larger than the bulk flow velocity. Therefore, Re based on this forced mean velocity and the hydraulic diameter of channel at x_4 is about 2.

4.1.1.3 Irregularity

Another feature of turbulence is the irregularity, which can be characterized by time trace of velocity at a fixed spatial point**.** Time traces of u_s in Fig. 4.1(b), (c) and (d) at x_4 = 100 μm are recorded in Fig. 4.3(b). Without forcing, u_s is almost a constant. With forcing of V = 8 $V_{p\text{-}p}$, u_s has clearly been enhanced. In this case, u_s already shows some slight irregularity, but not strong. However, as V is further increased to 20 $V_{p\text{-}p}$, the flow pattern becomes quite different, and u_s becomes quite large. Clearly, the velocity and its pattern are not regular but absolutely random. Note the forced velocity is much higher than the unforced velocity. This is because current LIFPA cannot distinguish flow direction, and what LIFPA measured directly is the magnitude of velocity.

4.1.1.4 Multiscale eddies:

One of the biggest challenges in the intrinsic features in turbulence is that a turbulent flow has multiscale eddies (i.e. a large number of degrees of freedom). Eddies can be described in the spectral space by the power spectrum density $E(f)$ of u_s, where f is the fluctuation frequency of u_s. $E(f)$ at various forcing levels (i.e. V) at x_4 is given in Fig. 4.4(a). Without forcing, $E(f)$ is flat as background noise, since there is no fluctuation of the velocity. The reason that $E(f)$ at low frequency is not completely flat could be caused by the shot noise of the detector and vibration of the syringe pump. With forcing of 10 $V_{p\text{-}p}$, $E(f)$ has significantly increased. However, $E(f)$ at high f, i.e. "small" scale eddies, is weak. As V is further increased up to 20 $V_{p\text{-}p}$, $E(f)$ at high f, the bandwidth and cut-off frequency f_c of $E(f)$, where noise starts to dominate, also increases and $E(f)$ gradually displays a similar form and slope. In particular, at 20 $V_{p\text{-}p}$ from 3-60 Hz, $E(f)$ is about 3-5

orders higher in magnitude than that of the unforced flow. This could indicate that the forcing generates velocity fluctuations that produce relatively "large scale" eddies, which in turn cascade into small scale eddies and down to Kolmogorov scale, where viscous force dominates. The energetic large velocity fluctuations also induce a high dissipation rate and a smaller Kolmogorov scale. This could explain why the cut-off frequency moves toward high frequency regime under forcing of high *V*. Furthermore, the spectrum varies continuously with *f*. Hence, there are multiscale eddies in cascade for the flow of Fig. 4.1(d), another typical feature of turbulence.

Of particular interest is that at 20 V_{p-p} the spectrum is not only continuously spanned in *f*, but also exhibits a -5/3 slope roughly from 3 to 60 Hz in a span of more than one decade! This is really a surprise, since in conventional turbulence, the -5/3 slope corresponds to the well-known Kolmogorov spectrum, which is one of the most important theories in exploring universal law in turbulence and can only be achieved at very high Taylor Reynolds number (Re_λ) on the order of 3000 [215]. However, the Re_λ corresponding to the spectrum of V = 20 V_{p-p} in Fig. 4.1(a) is estimated to be only 0.032, about five orders lower! Since the -5/3 spectrum corresponds to isotropic flow, we assume the flow is isotropic beyond approximately x_2 = 5 μm at 20 V_{p-p}. Therefore the slope of the spectra should be the same as the typical -5/3 Kolmogorov spectrum of a 1-D velocity fluctuation.

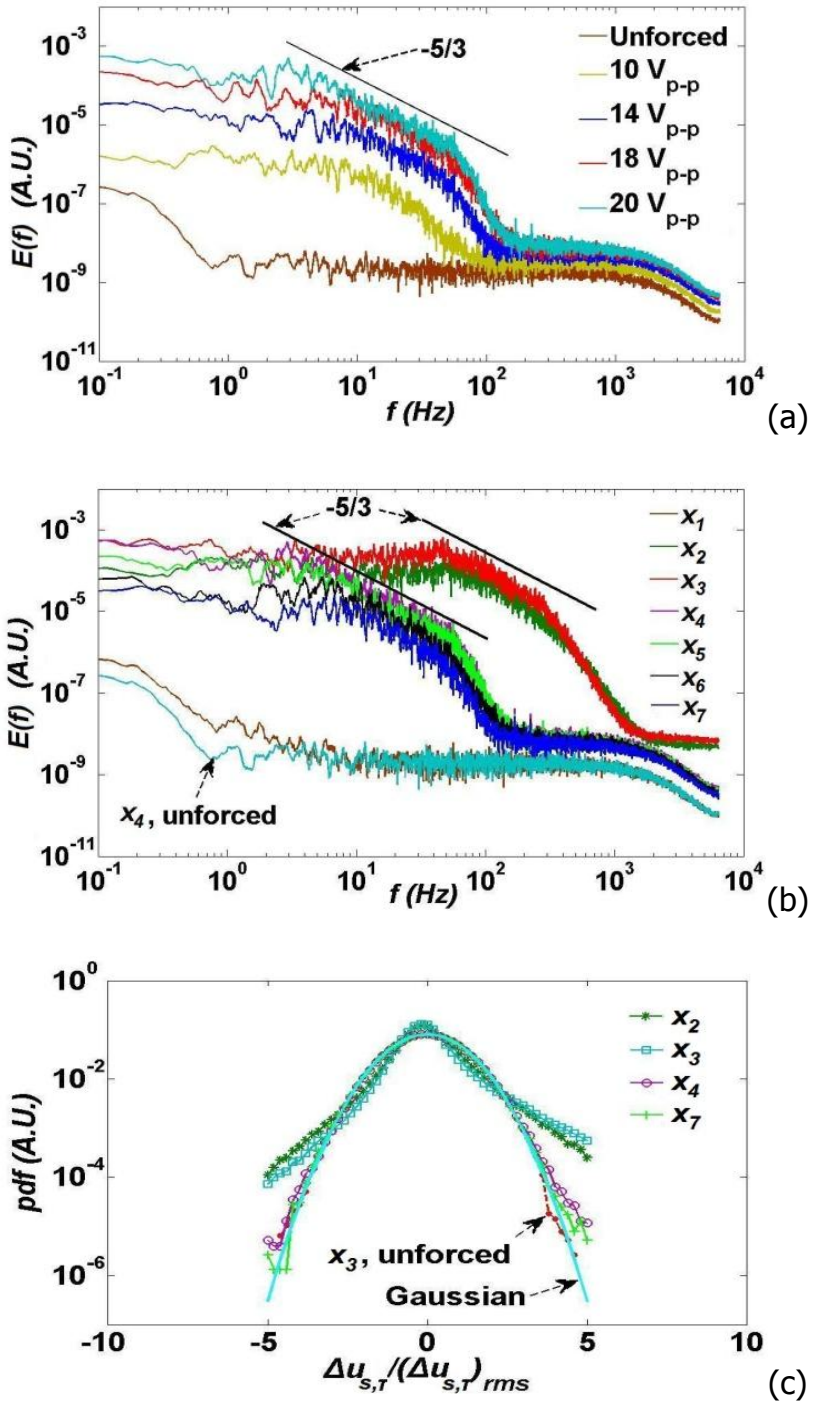

Figure 4.4 Power spectra of velocity *E(f)* under various conditions. (a) *E(f)* under various voltages at a fixed position. A -5/3 slope of *E(f)* is obtained when V = 20 $V_{p\text{-}p}$. The span of the -5/3 slope increases with V. (b) Spectra at various streamwise positions under V = 20 $V_{p\text{-}p}$. The measuring positions along streamwise direction relative to the entrance are, x_1 = -5 μm, x_2 = 5 μm, x_3 = 10 μm, x_4 = 100 μm, x_5 = 200 μm, x_6 = 300 μm, and x_7=500 μm, respectively. The unforced spectrum is used for reference. -5/3 spectrum starts at x_3 and persists in at x_7. (c) pdf of velocity increment with τ = 0.5 ms. The pdf

exhibits an exponential tail at x_2 and x_3, which can generally be achieved only at very high Re in macroflows. The pdf exhibites almost no exponential tail at x_7. Without forcing, the noise exhibits a normal distribution. Both -5/3 spectrum and exponential tail are features of high Re turbulence in macroflows.

To ensure the -5/3 spectrum is not simply an occasional behavior but a feature of the flow, the evolution of the *E(f)* along the streamwise direction was also measured as shown in Fig. 4.4(b), where V is 20 $V_{p\text{-}p,}$. At x_1 = -5 μm upstream of the entrance, the flow remains laminar and the *E(f)* is almost flat. However, at x_2, the spectrum changes dramatically and f_c rapidly increases to about 2000 Hz. Again this indicates a sudden transition from laminar to turbulence. At x_3 = 10 μm, there is already a narrow subrange with -5/3 slope from 45 to 300 Hz. Beyond f = 1500 Hz, the noise begins to dominate. At x_4 = 100 μm, the *E(f)* developed into a -5/3 spectrum with a time span of more than one decade. However, f_c and *E(f)* are all lower than that at x_3 position. At this position f_c is about 200 Hz. This could be because (1) the fast diffusion would decrease the conductivity gradient at the interface of the two fluids, which then decreases the driving force that causes the turbulence. (2) At x_2, the flow has already generated smaller eddies and the corresponding scalar (conductivity here) structures, which decay rapidly by molecular diffusion to smear the fine structures, since Re is low and the viscous dissipation is high. However, with additional development the random flow persistently possesses the -5/3 slope. Further downstream at x_5 = 200 μm and x_6 = 300 μm, *E(f)* continuously decays, and f_c decreases as well, but the -5/3 slope is kept. In this sense, the flow behavior is similar to that of free shear flows. Note: to ensure that the -5/3 slope is measured accurately, $E(f)*f^{5/3}$ versus f is also plotted and given in the supplementary.

Power Spectrum Density measured here is the spectra of velocity of u^2+v^2. We approximately assume the flow is isotropic for flow beyond x_2 at 20 Vp-p. Therefore the slope of the spectra should be the same as that of 1-D velocity fluctuation. As we know, accurate measuring the -5/3 slope directly in *E(f)* and *f* curve can be very difficult and cause larger error. Therefore, it is more accurate to draw a horizontal line. (Warhaft) to investigate whether the slop is -5/3. For this reason, to ensure that the -5/3 slope is measured accurately in Fig. 4.4(a) and (b), we use product $E(k)k^{5/3}$,instead of energy *E(k)* alone, to represent the vertical coordinates of the power spectra, as presented in Fig. 4.5(a) and (b). Clearly, both figures show flat spectra corresponding to the -5/3 slope in Fig. 4.4(a) and (b).

Normally a power spectrum with -5/3 slope ends at $k*\eta$ = 0.1 - 0.2 [216, 217] (k= $2\pi f/U$represents the wave number and η is the Kolmogorov scale), and beyond -5/3 spectrum, *E(f)* decays exponentially due to the intermittency at small scale. Based on this argument, we estimated that η is on the order of 0.2 μm at x_3, and 1 μm at x_4. These scales are at least one order smaller than the transverse dimension of the microchannel. This could support why the span of *E(f)* can be one decade long. It also display that beyond -5/3 spectrum, *E(f)* has an averaged slope of -6.3, which is within the range between -5.2 [217] and -7.2 [218] in very high Re turbulent flows. To evaluate the continuity of the flow, we use the ratio of mean free path ξ of water and the estimated smallest structure η, as the criterion[56]. ξ is about 0.02 nm[57]. Thus the ratio $\xi/\eta << 1$. This indicates that the flow in Fig. 4.1(d) is still continuous, although the channel is microscale in size.

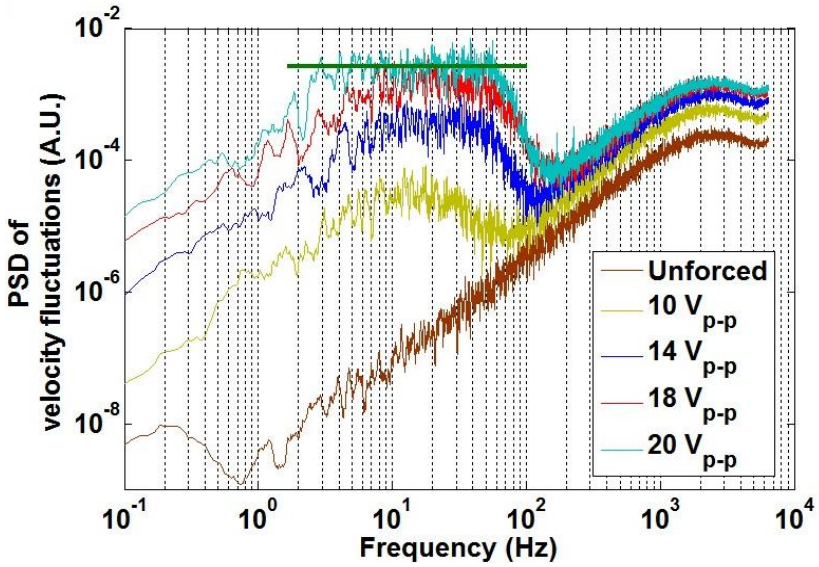

(a)

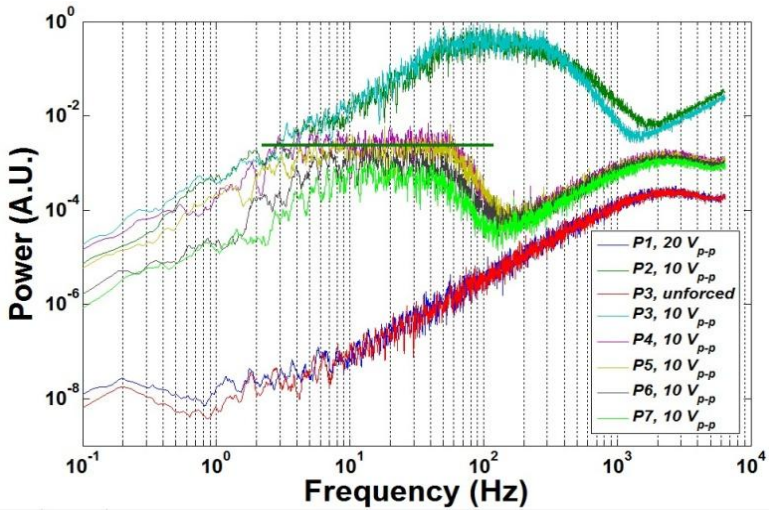

(b)

Figure 4.5 Power spectra of velocity $E(f)*f^{-5/3}$. (a) Corresponding $E(f)*f^{-5/3}$ from Fig. 4.4(a); (b) Corresponding $E(f)*f^{-5/3}$ from Fig. 4.4(b). There are clearly horizontal lines that represent -5/3 slope of $E(f)$. Therefore there are indeed -5/3 slope for the electrokinetically forced flow under V = 20 Vp-p at positions along streamwise direction.

Another feature of high Re turbulence is the existence of an exponential tail of probability density function (pdf) of velocity increments, $\Delta u_{s,\tau} = u_s(t+\tau) - u_s(t)$ (τ is the time interval) due to intermittency at small scale. This phenomenon is also amazingly observed in the flow of Fig. 4.1(d) as shown in Fig. 4.4(c), where, τ = 0.5 ms. Clearly, there is an exponential tail at x_2 and x_3, probably corresponding to the small scale eddies

shown in Fig. 4.4(b). At x_7, however, the exponential tail is negligible, indicating again that fast diffusion has smeared the smaller structures.

4.1.1.5 3-D flow

To explore if this electrokinetically forced flow is 3-D, we measured the distribution of the turbulent kinetic energy *e* of velocity fluctuations along the transverse direction at two different *z* (spanwise) positions at x_4, as shown in Fig. 4.6. While *e* of velocity fluctuations (caused by the low frequency noise, such as pump vibration) in the unforced flow is very small and negligible, *e* in the forced flow (when V = 20 $V_{p\text{-}p}$ is applied) is increased by 3-4 orders, and the flow becomes highly fluctuated and 3-D. From Fig. 4.6 we can find that *e* varies in the *y* direction: for z = 0 μm, *e* at y = 0 μm is about 30 times larger than that at y = 30 μm. This is reasonable as the flow disturbance is generated by $\vec{F}_e = -\frac{\varepsilon \vec{E}\cdot\vec{\nabla}\sigma}{\sigma}\vec{E}$, and $\vec{\nabla}\sigma$ reaches maximum at the centerline. The variation of *e* at in the *z* direction can also be found in Fig. 4.6, e.g. for y = 0 μm *e* at z = 0 μm is about 2.7 times larger than that at z = -100 μm. However, the variation in the *z* direction is much smaller than that in the *y* direction. It implies the influence of viscosity is conquered by the electrokinetic force, since $\vec{\nabla}\sigma$ and $\vec{E}$ are both in the *y* direction. Clearly, the visualizations in Fig. 4.1(d) and Fig. 4.4(b) already show that the flow is not homogeneous in the *x* direction. Thus, the flow is 3-D.

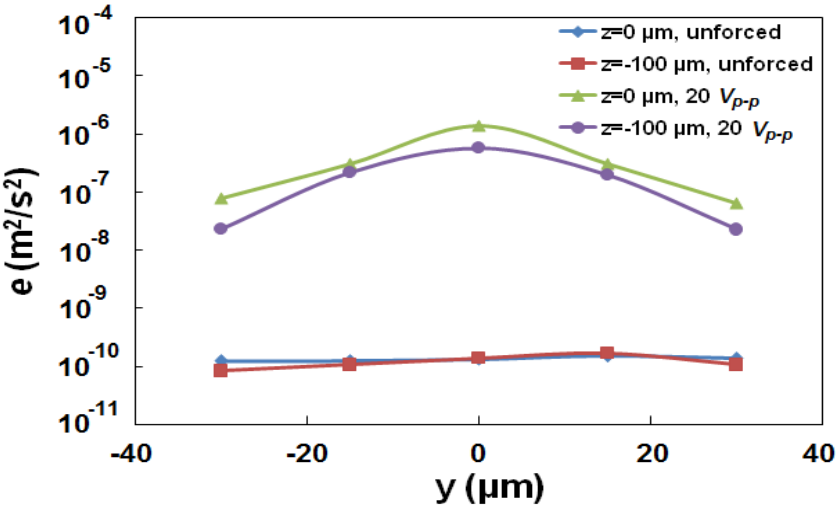

Figure 4.6 Turbulent energy *e* distribution along the transverse direction at two vertical positions without and with forcing at 20 V_{p-p} and at x_4. *e* is not homogeneous in both *y* and *z* directions, indicating that the forced flow is 3-D, when Fig. 4.4(b) is also concerned.

4.1.2 Characterization of scalar turbulence

Visualization of ultrafast turbulent diffusion of scalar is already given in Fig. 4.1(d). Fig. 4.7 shows the quantitatively measured time trace of the concentration *c* corresponding to the flow in Fig. 4.1(b) and (d) at x, y and z are 10 μm, 60 μm and 120 μm respectively, where *x*, *y* and *z* is the downstream distance from the entrance, vertical and transverse position. Without forcing, concentration *c* is a constant of about 1 μM, the pure initial dye concentration, indicating the flow is laminar and no mixing occurs between the two streams. With forcing, however, c exhibits a significant fluctuation even at high frequency of 100 kHz, and almost reaches the mean concentration *C* of around 0.5 μM.

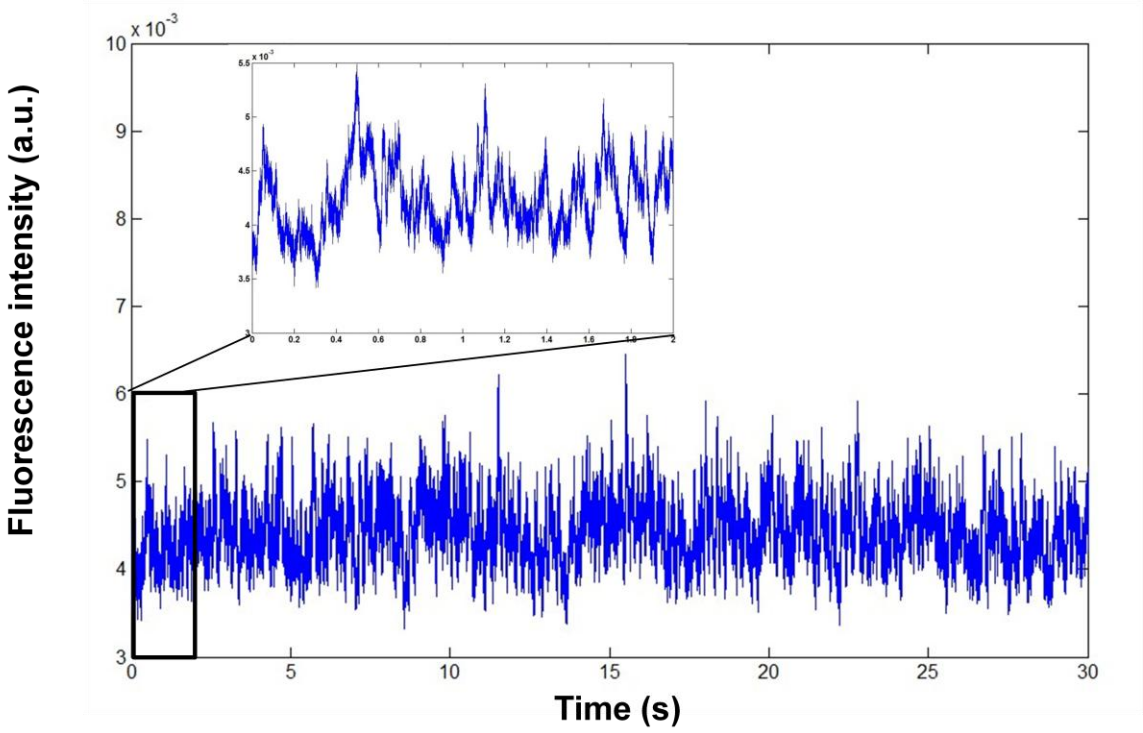

Figure 4.7 Time trace of concentration fluctuation at x=10 μm

The ensemble averaged concentration profile along y direction measured at x = 50 μm is shown in Fig. 4.8. The average time is 0.1 s. Without forcing, the mixing is controlled by molecular diffusion and is very slow. c is very low at the pure water stream and high at the dye solution stream, and there is a sharp increase of the c gradient near the interface between the two streams. Note the c gradient in the microchannel is not as sharp as those in macroflow, because of the relatively importance of molecular diffusion in microfluidics. With forcing at 8 V_{p-p}, c profile becomes more smoothed, and the mixing is increased. As the voltage is further increased to 20 $V_{p-p,}$ the flow becomes turbulent, and the mixing is so rapid that c profile become almost flat.

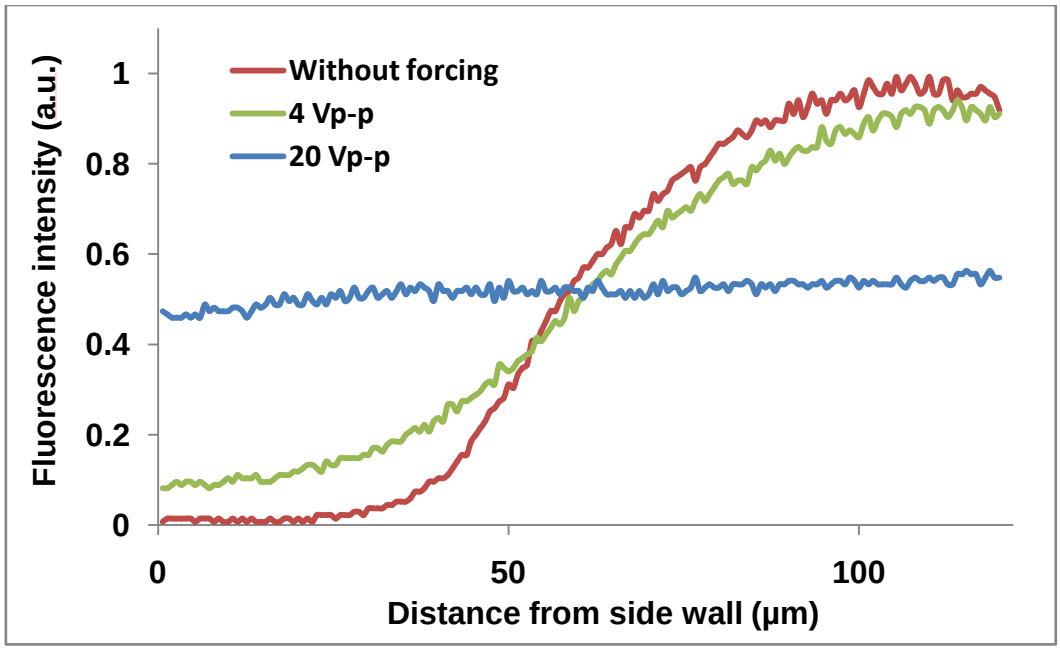

Figure 4.8 Concentration profile at 50 μm from the trailing edge

Evolution of segregation intensity of dye concentration, $C_{rms}/ < C >$, along streamwise direction with and without forcing is given in Fig 4.9, where C_{rms} is root mean square of c fluctuation, and $< C >$ is the ensemble average of concentration c. Without forcing, $C_{rms}/ < C >$ is low as expected. Note $C_{rms}/ < C >$ in the unforced flow is not zero, probably caused by the vibration of the two streams' interface. As the concentration gradient is high at the interface, any vibration in the interface will cause concentration fluctuation although the flow is still laminar. However, with forcing at 20 $V_{p\text{-}p,}$ $C_{rms}/ < C >$ increases both rapidly and significantly at the inlet of the channel. After achieving its maximum approximately at x = 10 μm, the $C_{rms}/ < C >$ decreases quickly as well downstream.

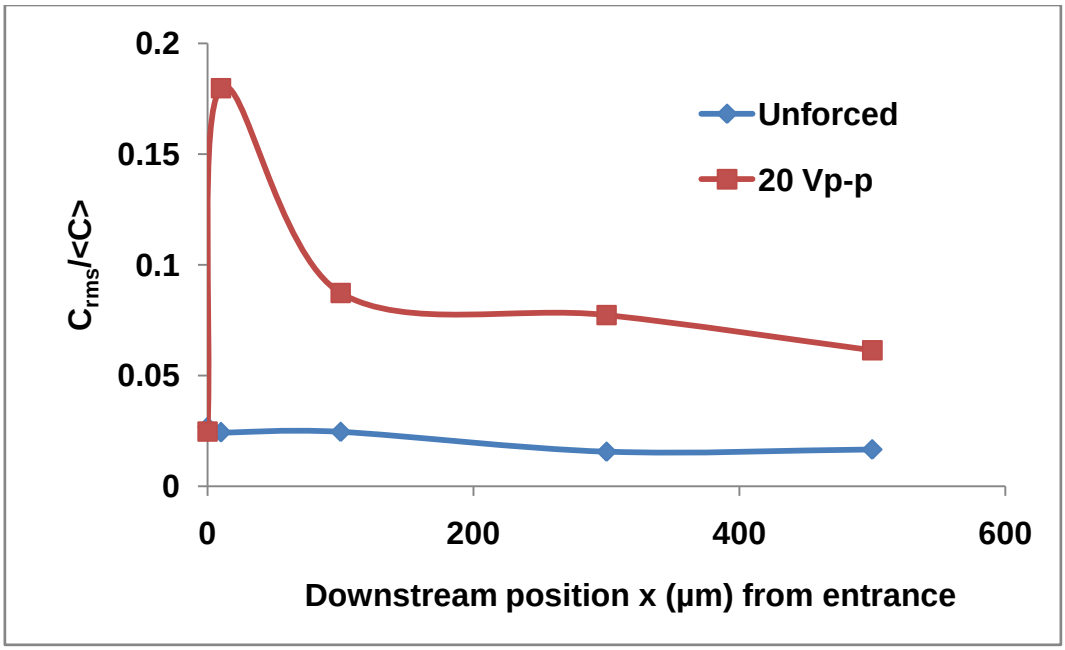

Figure 4.9 Concentration fluctuation evolution along x positions with and without forcing

The probability distribution function (pdf) of the concentration fluctuation at various position, $\Delta C'/(\Delta C)_{rms}$, where $\Delta C'=C'(t+\Delta t)-C'(t)$, and $(\Delta C)_{rms} = <\Delta C'^2>^{-1/2}$, is given in Fig. 4.10 for the unforced and forced flow. The forced flow corresponds to the flow of Fig. 4.1(d). Fig. 4.10 shows that the pdf of c is a Gaussian distribution as expected, but the pdf of the forced flow at 20 V_{p-p} do not display a Gaussian distribution, but an exponential tail. The exponential tail is usually resulted from the intermittency of the small scale structures. The highest exponential tail is near the position of 10 μm from entrance (x_2'), and the reason is probably that at this position scalar has the smallest structures (as spectrum in Fig. 4.11), and thus high scalar gradient. The exponential tail degraded along the streamwise position beyond this position. This could be explained by the fact that the molecular diffusion becomes very important at x_2' where small scale

structures have already been generated. Downstream of x_2', the small scalar structures are rapidly smeared by the molecular diffusion and concentration gradient decreases, and hence, the exponential tail also decreases.

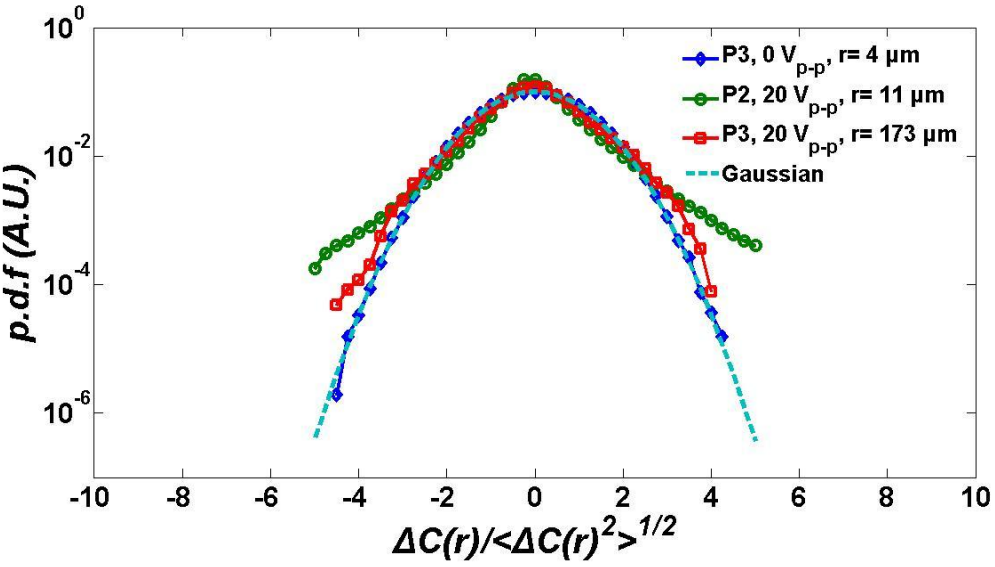

Figure 4.10 pdf of concentration fluctuation along x positions

As the scalar turbulence has multiple scale structures with difference sizes, power spectrum density (PSD) is often used to describe the scale distribution in frequency domain. Clearly the scalar turbulence strongly depends on the forcing voltage. The PSD of c for various forcing voltages at x = 100 μm is given in Fig. 4.11(a), which shows that both PSD and the cut-off frequency f_{cn} where noise starts to dominate increase with the voltage. Without forcing, the PSD is very low, although there are some peaks which could be caused by the vibration of the interface of the two streams. With forcing at 8 V_{p-p}, there are some fluctuation and PSD increases from 1 to 100 Hz. At 14 V_{p-p}, the PSD not only increases, but also starts to exhibits a slope of -5/3 within the range of 7-50 Hz. As voltage is further increased to 20 V_{p-p}, the bandwidth that possesses the -5/3 slope is

increased to the range of 4-60 Hz, i.e. more than one decade. In macroflows, the -5/3 spectrum is the so-called Obukhov-Corrsin spectrum, which normally can only be observed when Re is sufficiently high, e.g. the corresponding Taylor microscale Reynolds number $Re_\lambda > 2{,}000$ is required before the -5/3 spectrum occurs in shear flow [215], although it is possible to achieve it at lower Re_λ for shear-free grid generated turbulent flows [219].

The development of PSD of the forced flow along streamwise direction is also investigated and the result is given in Fig. 4.11(b). At $x_1' = 5$ μm, the PSD is similar to that of the unforced flow, indicating that the flow is still laminar. However, at $x_2' = 10$ μm, the PSD has dramatically increased, and is about three orders higher than that of the unforced one in the range of 30-100 Hz and the *fcn* is increased to more than 1 kHz. At $x_3' = 100$ μm, the PSD has developed the -5/3 spectrum. Further downstream at x_4' and x_5' is 300 μm and 500 μm respectively, both PSD and f_{cn} decrease, but there still are a small ranges of spectrum of -5/3 slope.

Note that it is difficult to accurately measure the slope of the spectrum in figure 4.11 directly based on coordinate $E(k) \sim k$. To ensure that the slope is -5/3, it is recommended [220] that the $E(k)*k^{5/3} - k$ should be used to evaluate if the slope is really -5/3. For this reason, to ensure that the slope is -5/3, $E(k)*k^{5/3} - k$ is also plotted in the Fig 4.11(c) and (d) respectively for Fig. 4.11(a) and (b).

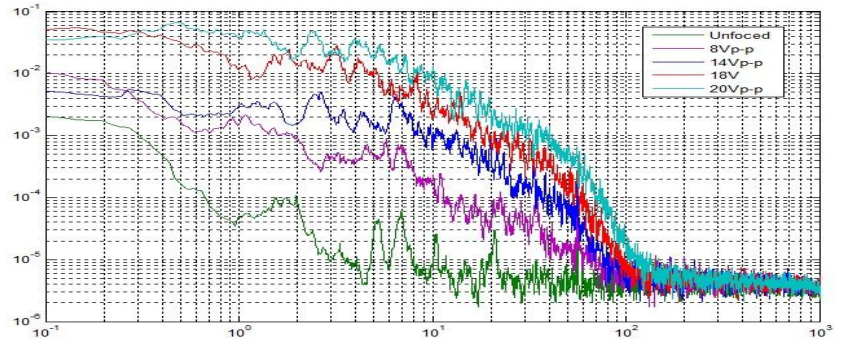

(a)

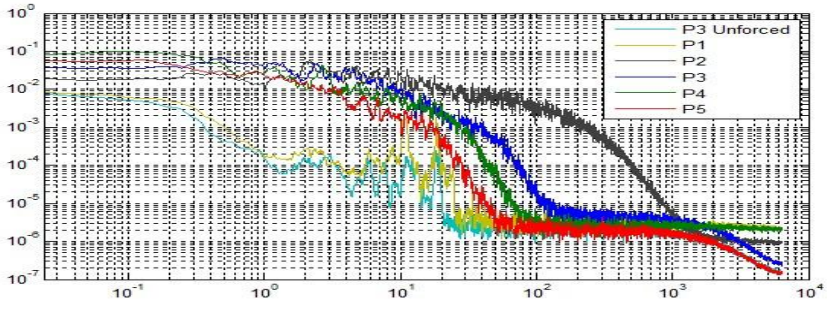

(b)

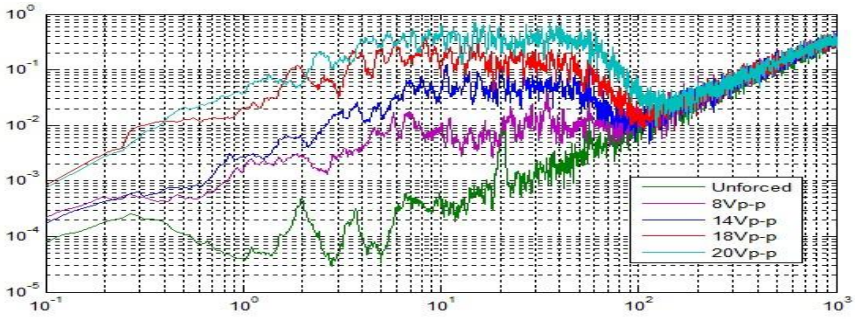

(c)

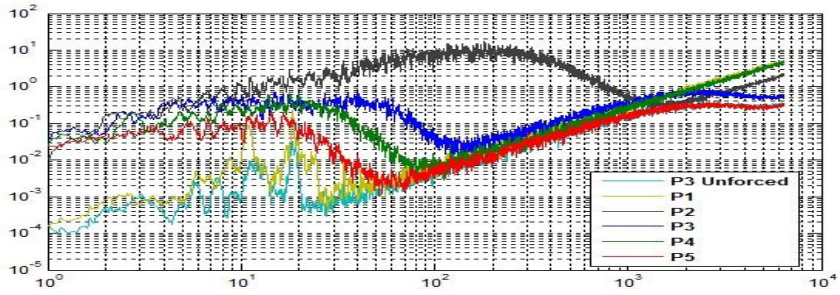

(d)

Figure 4.11 Power spectrum of concentration fluctuation at (a) different forcing, (b) x positions. And after E(k)×k5/3 adjustment of (c) different forcing, (d) x positions.

Another interest in this work is about the Batchelor –1 spectrum beyond the –5/3 spectrum. In our experiment, although the -5/3 slope is achieved, beyond it no -1

Batchelor spectrum of viscous-convective sub-range is observed in the forced flow. Spatial resolution of the measurement should not be the cause, although the spatial resolution may not be high enough for the entire Batchelor spectrum of the forced flow at x_3'. The Kolmogorov scale is estimated to be about 1 μm based on measured power spectrum of velocity, and the corresponding Batchelor scale is about 0.02 μm, since the Schmidt number is about 2000. The resolution of the measuring system is about 0.203 μm. Therefore, the measuring spatial resolution is sufficient to measure at least part of the Batchelor spectrum, if it at all exists.

4.1.3 EKI mixing

4.1.3.1 Fast mixing

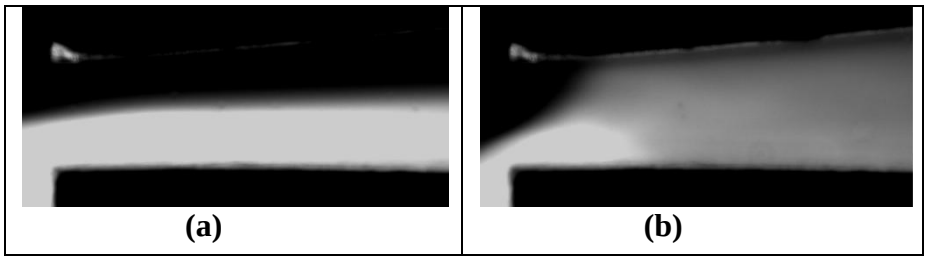

Figure 4.12 Top view of the fast mixing result in non- parallel microchannel. (a) Without electric field and; (b) with electric field.

We first present a visualized mixing result in the non-parallel microchannel with 5 °angle as shown in Fig. 4.12. The flow rate of the two streams was kept at 5 μL/min. The conductivity ratio γ of the two mixing streams and the frequency f of the applied voltage signals were 100 and 10 kHz respectively. The same AC voltage of 16 V_{p-p} was applied to the two electrodes, with a phase shift of 180 °.

Visualization in Fig. 4.12 shows that, without electric activation on the electrodes, the two streams flow through the channel with little mixing on their interface as shown in Fig. 4.12(a); However, when we applied voltage on the electrodes, the concentration in transverse direction was almost uniform at ~ 200 μm downstream from the entrance, and the two streams were mixed as shown in Fig. 4.12(b). It is indicates that, the presented micromixer has the capability for fast mixing of streams at even low voltage and relatively high AC frequency. The parametric study of this micromixer is given below.

4.1.3.2 Effect of electrode position

Mixing results in two cases were compared at first: electrodes are placed at the side walls and at the ends of the channel, respectively. To our knowledge, the former one is new and the latter one has been studied widely as electrokinetic micromixers.[24, 221]

Generally speaking, both management and control of flow play an important role for transport phenomena in conventional fluid dynamics.[222] Here the management of the location of the electrodes on mixing is compared to demonstrate the advantage of the presented mixromixer over the conventional one. In the experiment, we kept the same flow rate 5 μL/min and conductivity ratio (1:10) of the two streams, and applied the same $\vec{E}$ of 200 V/cm for the two devices. In the following experiments, the flow rate and conductivity ratio will be kept the same unless specifying. A relative low AC frequency (1 Hz) has been used, since the same $\vec{E}$ cannot be achieved at higher frequency in the plastic side walls micromixer.

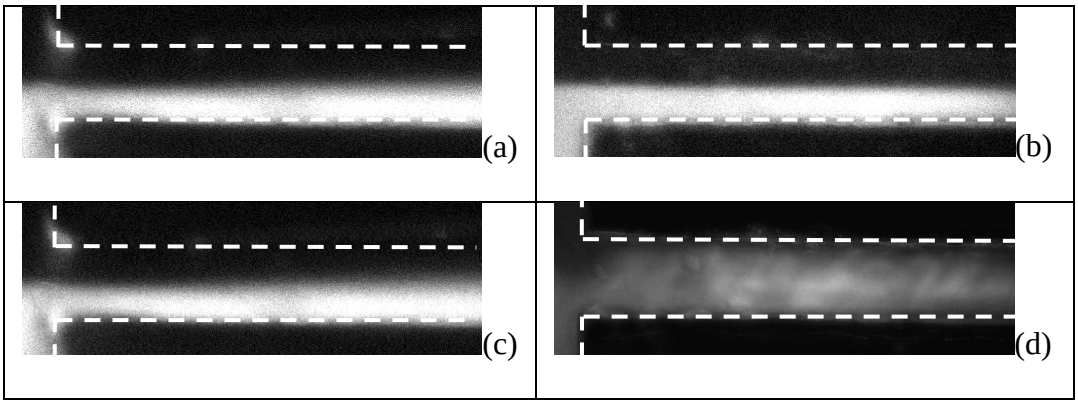

Figure 4.13 Comparison of mixing results under different electrode positions and corresponding electric fields. In (a) and (c) electrodes are located at the ends of the channel, and the electric field is parallel to the bulk flow direction. In (b) and (d) electrodes are placed at the side walls, and the electric field is in transverse direction.

As shown in Fig. 4.13, it is clearly illustrated that even though under the same $\vec{E}$, the mixing is much stronger when the electrodes are placed on the side walls than that when the electrodes are located at the ends of the microchannel. For the plastic side walls, to achieve the same $\vec{E}$ as that of the gold wall, we had to use a voltage amplifier on the electrodes located at the ends of the channel. In this case, it is difficult to apply high AC voltage and high frequency signal simultaneously on the electrodes. However, for the case with the gold side walls, no power amplifier is required for high $\vec{E}$ on the side walls electrodes. The single function generator can effortlessly supply sufficient $\vec{E}$ and high frequency on the electrodes simultaneously. Fig. 4.13 indicates that the management of the electrode can significantly affect the mixing as well.

The main reason for the faster mixing in the conductive side walls channel is that, in the case where two electrodes directly formed side walls, $\vec{E}$ is generated in the direction perpendicular to the flow direction, meanwhile, with the conductivity gradient between two mixing streams in the vertical direction to the flow direction, the mixing is

enhanced significantly. However, in the case where the electrodes are located at the ends of the micromixer, $\vec{E}$ is generated along the flow direction, and obviously there is no conductivity gradient between the two streams in this direction, consequently, the mixing result is reduced. In the following the electrokinetics micromixer with conductive will be characterized.

4.1.3.3 Conductivity effect

In our present experiments, two mixing streams with conductivity gradient were subject to an external electric field, mixing was directly influenced by the Coulombic force.[131] Consequently, the effect of conductivity gradient (i.e. conductivity ratio of the two streams in present work) on mixing performance was investigated.

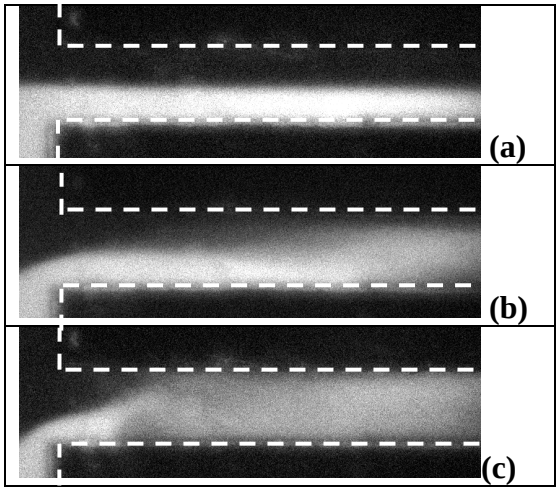

Figure 4.14 Visualization and comparison of mixing results in the micromixer with different conductivity ratios. (a) 1:1, (b) 1:2, (c) 1:10.

In order to conduct a parametric study to quantify the effect of the conductivity ratio of the two streams on the mixing performance, in this experiment, frequency of the

applied voltage signals are kept constant, i.e. f = 10 kHz. Applied sin signal voltage is kept at 10 V_{p-p}. Three conductivity ratios were investigated, i.e. 1:1, 1:2, 1:10.

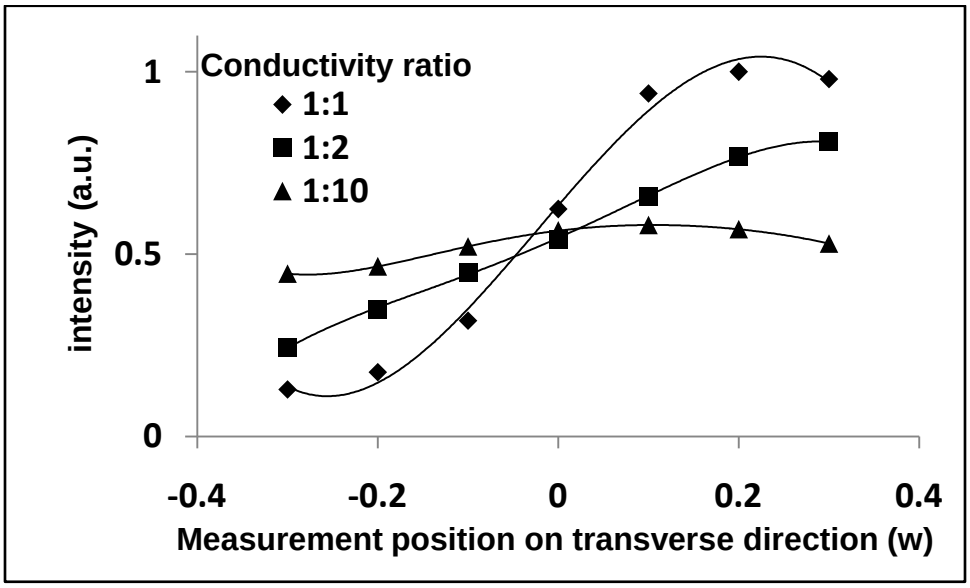

Figure 4.15 Comparison of concentration profile in transverse direction at x= 3 w from the channel entrance with different conductivity.

Mixing performances under different γ are shown in Fig. 4.14. When the conductivity ratio γ between the two streams is 10, the mixing performance is the stronger than that when γ are 2 and 1 respectively. In Fig. 4.15, the corresponding C distribution in the transverse direction was displayed. As we know, the stronger the mixing, the more uniform the concentration (i.e. the fluorescence intensity here) in the transverse direction at a given streamwise position. The curve should approach flat when the fluids are well mixed in the microchannel. According to Fig. 15, one can see that when the conductivity ratio γ is 10, concentration distribution reached a relatively uniform profile at 3 w (w is the entrance width of the microchannel) from the entrance,

while at the same x position, C distributions were still far away from a flat profile, when γ are 2 and 1 respectively.

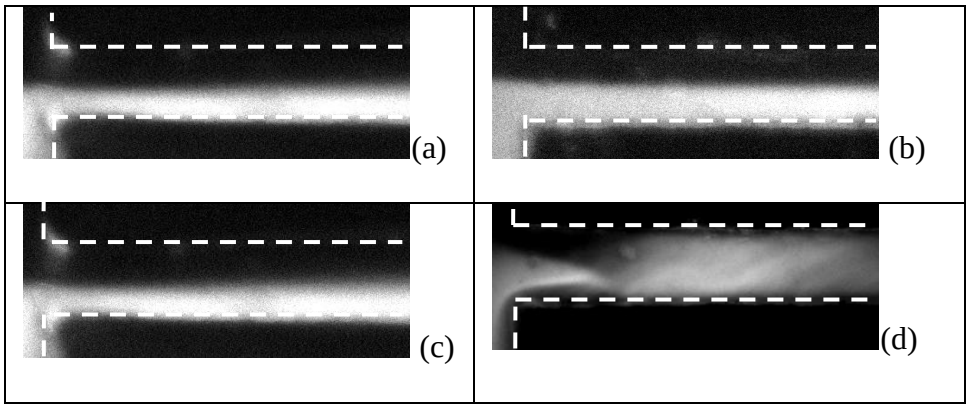

Figure 4.16 Visualization and comparison of mixing result in micromixer with electrodes located at ends of channel. (a) without voltage, (c) with voltage; and micromixer with conductive side walls (b) without voltage, (d) with voltage.

Specially, mixing results under low γ in both conductive side walls micromixer and plastic side walls micromixer with electrodes located at the ends of the channel have been measured and compared, as shown in Fig. 4.16. In this experiment, applied electric field are kept constant, i.e. 200 V/cm. For the plastic side walls micromixer, an alternative perturbation was added to the applied static electric field, to maximum the mixing enhancement, which were 20 $V_{p\text{-}p}$ in amplitude and 10Hz in frequency. γ was kept at 1:2 for both micromixers.

In Fig. 4.16, it clearly shows that, under 200 V/cm electric field, obviously strong mixing result is easily accomplished in the micromixer with conductive side walls. While in the micromixer with electrodes located at ends of channel, no obviously mixing is observed. One key reason of this conductive side walls micromixer can lead to better mixing is that, the electric field's direction as well as the Coulombic force direction are

always perpendicular to the streamwise direction (as shown in Fig. 2.1). This arrangement leads to the conductive fluid molecular motion in the direction perpendicular to the interface of two mixing fluids. This is the fluids motion which consequently leads to the mixing between two fluids. On the other hand, for the case of electrodes located at the ends of channel, electric field is parallel to the streamwise direction, which is hard to generate fluid motion perpendicular to the streamwise direction. Therefore, mixing cannot be achieved as easily as in the conductive side walls micromixer.

4.1.3.4 Frequency effect

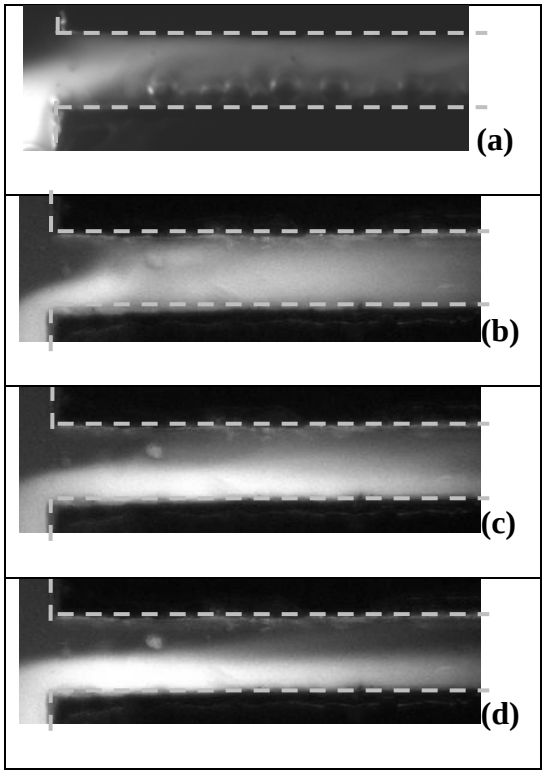

Figure 4.17 Visualization and comparison of mixing result in microchannels with different frequency and DC signal. (a) DC, (b) 10 KHz, (c) 1 MHz, (d) 2 MHz.

Influence of AC signal frequency on mixing has also been investigated. Frequency was varied in the range of 100 Hz to 2 MHz. Mixing result under DC voltage was also presented as a comparison. In this experiment, applied voltage signals are kept constant as well as in the DC situation, i.e. V =12 V_{p-p} .

Fig. 4.17 shows mixing results under DC voltage and different frequencies of applied AC signal. When the frequency is 10 KHz, the mixing performance is stronger than that when the frequencies are 1 MHz and 2 MHz. When DC voltage was applied on electrodes, strongest mixing was achieved in very short time. However, bubbles were also generated within 1 second since voltage was applied. The channel was finally blocked by these bubbles. C distributions in the transverse direction are shown in Fig. 4.18 for three different AC frequency mixing results. According to this quantitative C distribution, one can more easily see that when the applied AC signal frequency is 10 KHz, concentration distribution reaches the relatively uniform profile at 2.3 w from the entrance. While at the same x position, however, when applied AC signal frequency are 1 MHz and 2 MHz, the profiles of the concentration distribution are still far away from a flat profile.

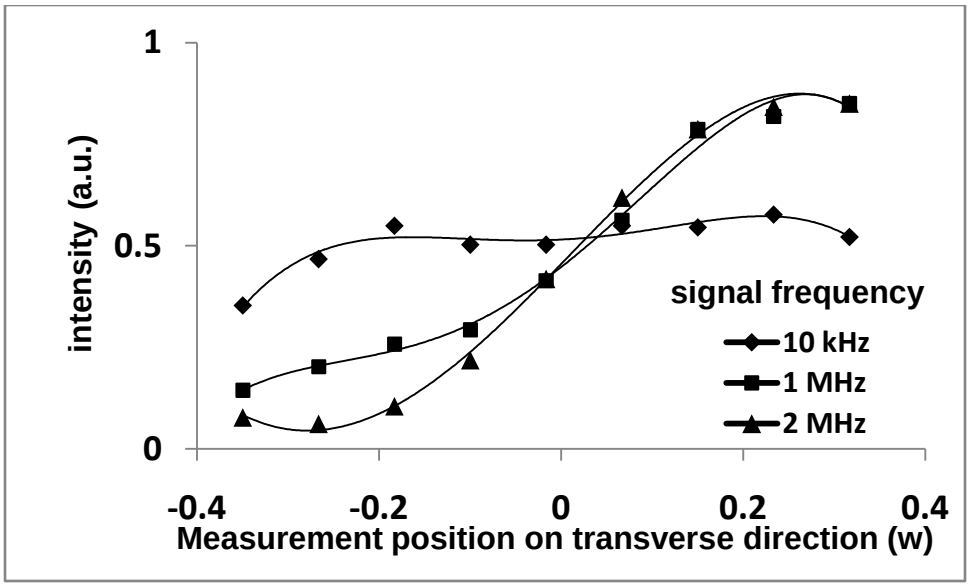

Figure 4.18 Comparison of concentration profile in transverse direction at x= 2.3 w from the channel entrance with AC signal.

However, mixing results under high frequency can be still achieved at higher conductivity ratio, which is 1:100 in this experitment. Results are shown as in Fig. 4.19. Applied frequencies vary from 30 MHz to 40 MHz. In this experiment, applied voltage signals are kept constant, i.e. V = 20 V_{p-p}.

Fig 4.19 shows mixing results under each frequency of applied AC signal. It is obviously showing that, when the applied AC signal frequency is 30 MHz, the mixing performance is the stronger than that when the frequencies are 35 MHz and 40 MHz. However, at our current applied voltage of 20 V_{p-p} (limitation of the function generator), 40 MHz was the highest frequency at which we can achieve mixing in the mixer. This is also an important advantage that mixing can be acquired under high AC frequency electric field. Since in many cases, low frequency AC signal could generate bubbles due to electrolysis in microchannels, especially when buffer is used, since buffer has relatively high conductivity. The present new design of the micromixer could

significantly reduce the risk of generation of the bubble in the microfluidic device, when the operation AC frequency is increased to higher than 10 kHz, even for fluids with relatively high conductivity (1000 μS/cm) without bubble generation.

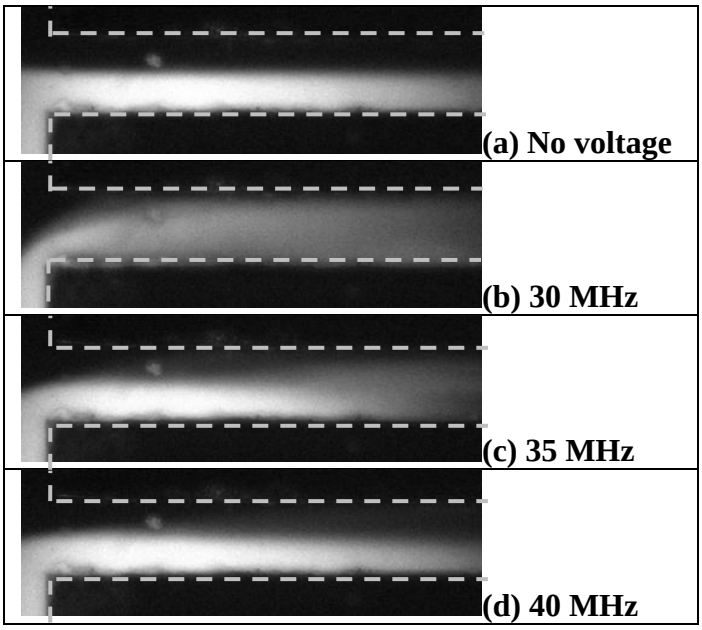

Figure 4.19 Visualization and comparison of mixing result in microchannels with different frequency of applied voltages. (a) without voltage, (b) 30 MHz, (c) 35 MHz, (d) 40 MHz.

To explain the result of poor mixing at high frequency, we firstly introduce the charge relaxation time τ, which, for a fluid with continuous electrical properties, is equal to

$$\tau = \frac{\varepsilon}{\sigma} \tag{4.2}$$

That is the ratio between the fluid permittivity ε and its conductivity σ. It measures the rate at which the free charges relax from the bulk of the fluid to the outer boundaries of a dielectric mass. For an AC electric field oscillating at frequency *f*, one can compare the charge relaxation time with the inverse of the electric field frequency *f*. This leads to the ratio of time scales:

$$T = \frac{\tau}{1/f} = \tau f \tag{4.3}$$

If this ratio *T* is less than 1, the free electric charges (or free charge density ρ_f) have enough time to build up in the fluid, and therefore can be acted upon by the electric field. In another word, the smaller *T* is, the more time flow has to fully develop between two electric signal pulses.

On the other hand, when this ratio *T* is much larger than 1, that is $f \ll 1/\tau$, the free electric charges do not have time to build up in the fluid, and therefore cannot be acted upon by the electric field. In this case, the first term $\rho_f \vec{E}$ is negligible. And it is obvious that last two terms in equation (2.2) depend on the variation of the fluid permittivity. According to the experiment result of Moctar et al.[49] the gradient of permittivity decrease along with the increase of applied AC electric field's frequency, and the gradient of permittivity becomes very low at high frequencies.

Due to the two situations above, it comes to the conclusion that, under high frequency AC electric field, the mixing became weaker than that under low frequency AC electric field.

It is known that, fluid mixing will start inside the microchannel when applied voltage exceeds a threshold voltage value under a certain frequency. This particular voltage value is called critical voltage. The relation between critical voltage and frequency was investigated to enhance our understand of frequency effect on mixing results in this conductive side walls channel. And results are shown by a curve in Fig. 4.20.

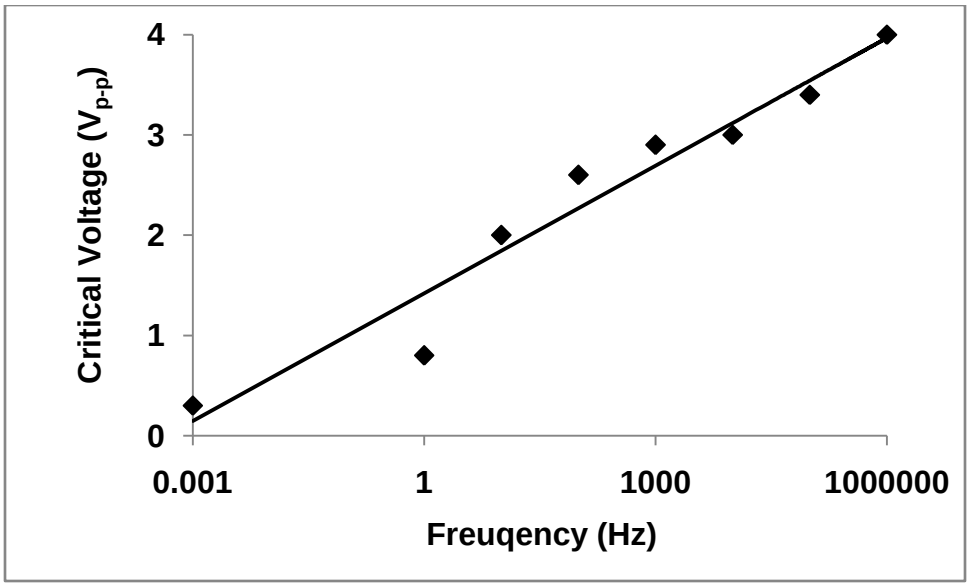

Figure 4.20 Critical voltage vs. the frequency of the applied AC electric field for mixing enhancement.

Fig 4.20 suggests that, along with the increasing of frequency, the critical voltage need to be higher and higher. For frequency of 1Hz, voltage of 0.8 V_{p-p} is enough to start a mixing process inside the microchannel, when the frequency goes to 1 MHz, voltage of 4 V_{p-p} is desired to start the mixing process. This phenomena could be explained by that, when the frequency is increasing, the period of each wave in becoming shorter and shorter for moving the charged molecules to the same distance as the low frequency, consequently, to achieve an equivalent mixing result, a larger columbic force is required, then a high voltage is need to be applied.

4.1.3.5 Voltage effect

As the Columbic force plays a key role in the currently designed mixing process, mixing should be directly related to $\vec{E}$. Therefore, voltage effect on mixing result was

investigated. In this experiment, frequency of the applied voltage are kept constant, i.e. *f* = 10 kHz. Applied voltages varied from 0 V_{p-p} to 14 $V_{p-p.}$

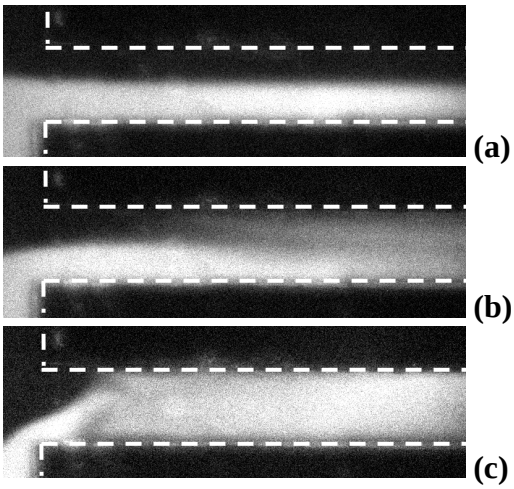

Figure 4.21 Visualization and comparison of mixing result in microchannels with different voltages. (a) 0 V_{p-p}; (b) 6 V_{p-p}; (c) 14 V_{p-p}.

Fig. 4.21 shows mixing performance under different applied voltages. As visualized in Fig. 4.21, despite the molecular diffusion, there is no obviously mixing on the interface of the two streams when no voltage is supplied, 0 V_{p-p}. However, the mixing is significantly enhanced under the applied voltages of 6 V_{p-p} compared with that without AC signal, i.e. 0 V_{p-p}. With further increasing voltage to 14 V_{p-p} the mixing becomes the strongest.

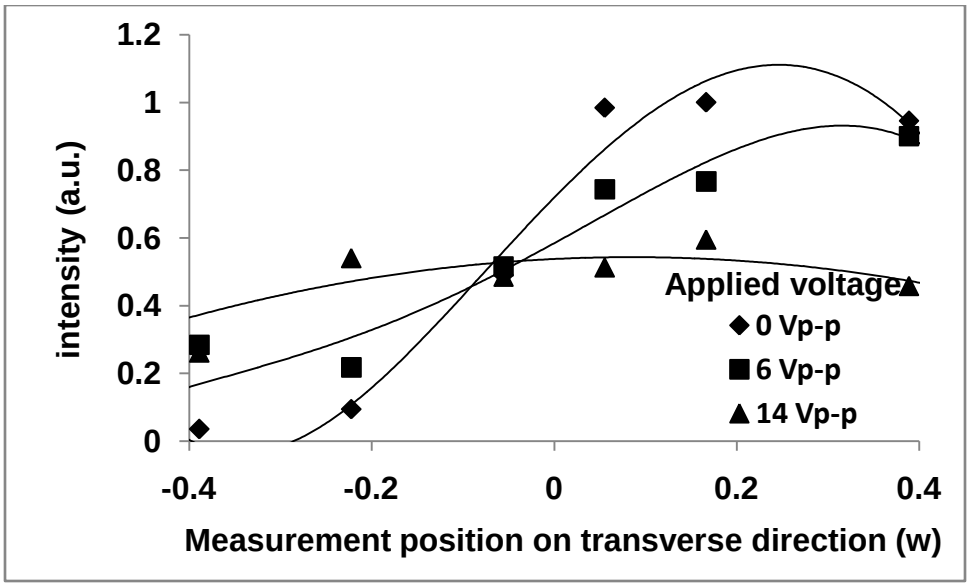

Figure 4.22 Comparison of concentration profile in transverse direction at x= 3 w from the channel entrance with different AC voltages.

Fig. 22 shows the quantitative concentration C distribution in the transverse direction, at streamwise position 3 w away from the entrance. In Fig. 4.22, it shows that, C distribution under 14 V_{p-p} reaches the most uniform profile at 3 w from the entrance, while at the same x position, the profile of the concentration distribution under voltages of 0 V_{p-p} and 6 V_{p-p} are still far away from a flat profile. This quantitative result indicates that mixing is enhanced rapidly with increased voltage in the conductive side walls micromixer.

4.1.3.6 Mixing of two fluids with equivalent conductivity

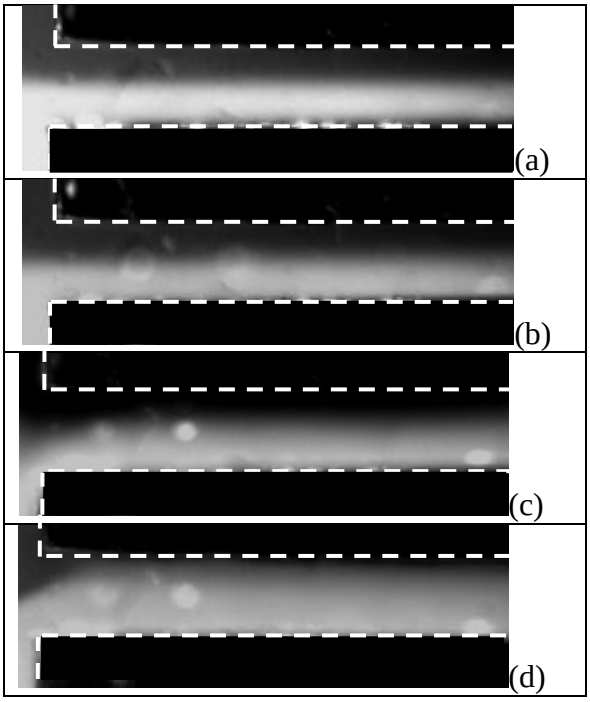

Figure 4.23 Visualization and comparison of mixing result in the micromixer with equivalent conductivity of the two fluids and comparison of different conductivity absolute values. (a) Without voltage, (b) 10 μS/cm, (c) 100 μS/cm, (d) 1000 μS/cm.

In realistic applications, it's not always convenient to require two mixing fluid have a conductivity ratio, on the other hand, the task of mixing two fluids with equivalent conductivity has more practical meaning and also is more challenging. In our conductive side walls channel, this demanding mission has also been accomplished. In present experiment, low flow rate has been used, i.e. 1 μL/min, voltage was kept at 20 $V_{p\text{-}p.}$ Frequency was set at 1 MHz. Electrically neutral dye Rhodamine B was used as the scalar marker, to minimize the possible conductivity difference between the two fluid streams. Moreover, with the conductivity ratio kept at 1, mixing results under different

conductivity absolute values of both mixing fluid have also been investigated, i.e. 10 μS/cm, 100 μS/cm, 1000 μS/cm, respectively. Results are shown in Fig. 4.23.

In Fig. 4.23, it can be clear see that strong mixing result has been accomplished in conductive side walls mixer, even there is no conductivity different between the two streams to be mixed. It is could also be seen in these figures that, the mixing result is weakest under the conductivity absolute value of 10 μS/cm, stronger in 100 μS/cm conductivity, and strongest in 1000 μS/cm conductivity. These results could be explained by that, from equation (2.2), in the higher conductivity situation, higher free charge density ρ_f leaded to a stronger Coulombic force, by which the mixing enhancement were increased.

This result has a very important realist meaning for bio-reaction and chemicals analysis applications. Because, in real applications, conductivity difference between two mixing fluid samples is not always exist. By our present conductive side walls mixer, mixing could achieve whether there is conductivity different between two mixing fluids, which means conductivity ratio is no longer an indispensable requirement for the two mixing samples. This achievement will certainly broaden the application of this kind of lab-on-a-chip mixing devices.

4.1.3.7 Re number effect

Different Re number effects on mixing results were investigated as well. In this experiment, frequency of the applied voltage are kept constant, i.e. f = 10 kHz. Applied voltage was kept at 6 $V_{p\text{-}p.}$ Flow rate were changed in the range of 1 μL/min to 5 μL/min.

three different Re number were compared, i.e. 0.1, 0.3, 0.5. Results are shown in Fig. 4.24.

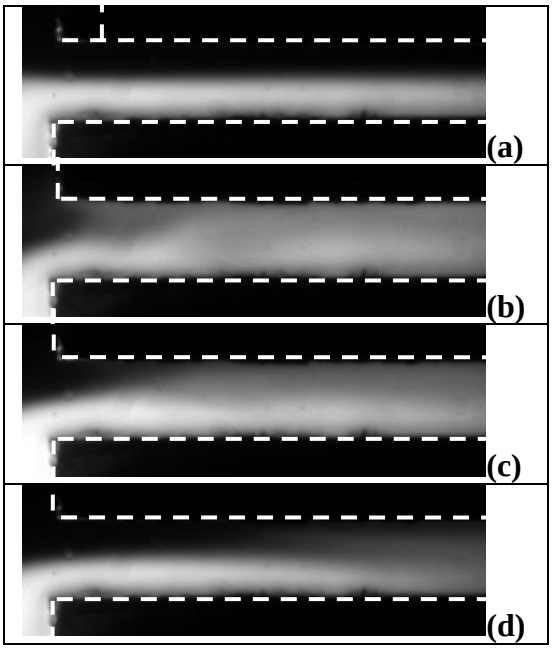

Figure 4.24 Visualization and comparison of mixing result in the micromixer with different Re numbers. (a) Without voltage, (b) Re = 0.1, (c) Re = 0.3, (d) Re = 0.5.

As visualized in Fig. 4.24, the mixing is strongest when the Re number was 0.1, compared with situations that Re number were 0.3 and 0.5. When low Re number was applied, i.e. low flow rate was applied, in our cases, mixing could be achieved much faster than Re number situation. It is due to the fact that, fluid molecular motion by Coulombic force was perpendicular to the interface of two fluids, when the applied voltage was remain the same, the Coulombic force in was remain the same. Therefore, in a low flow rate situation, the mixing could be achieved more close to the entrance. On the other hand, in high flow rate situation, same mixing will be achieved at further from the entrance compare with the low flow rate situation. Hence, mixing in our mixer could be much stronger under low Re number than that under high Re number.

4.1.3.8 Effect of the angle between the two electrodes

It is found that the mixing depends strongly on the angle between the two metal sidewalls, if the channel sidewall is changed from parallel to non-parallel. Furthermore, with a small angle between these two electrodes, the mixing can be surprisingly enhanced compared with that in the parallel channel. To investigate the angle effect, γ of the two mixing streams and the frequency of the applied voltage signals were kept constant, i.e. $\gamma = 100$ and f = 10 kHz respectively. The flow rate of the two streams was kept at 5 μL/min. The same AC voltage signal of 12 V_{p-p} was applied to both electrodes.

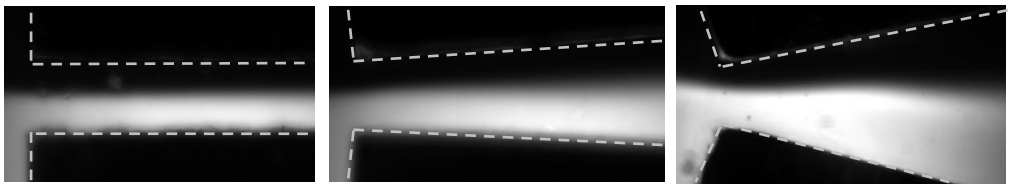

(a) 0 º0 V **(c) 5 º0 V** **(e) 30 º0 V**

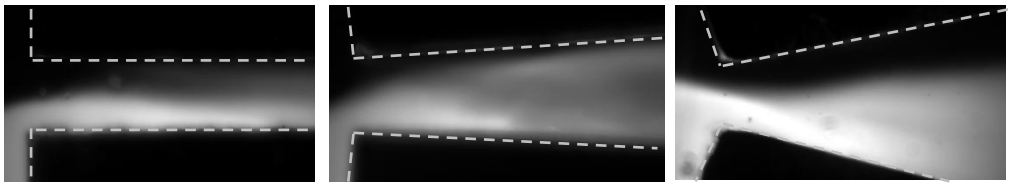

(b) 0 º12 V_{p-p} **(d) 5 º12 V_{p-p}** **(f) 30 º12 V_{p-p}**

Figure 4.25 Visualization and comparison of mixing result in microchannels with different angle.

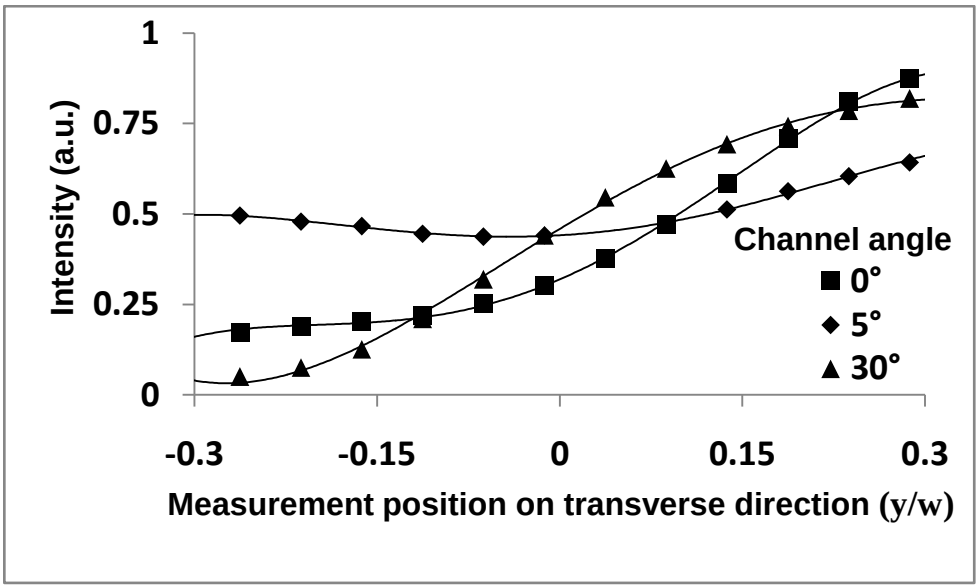

Figure 4.26 Comparison of concentration profile in transverse direction at x = 9/4 w from the channel entrance with AC signal.

Fig. 4.25 shows an example of mixing performance with and without AC signal for both parallel (0°) and non-parallel conductive sidewalls. There were two microchannels of non-parallel electrodes with 5° and 30° angles respectively. As visualized clearly in Fig. 4.25, the mixing in the channel of 5° was stronger than that in the parallel channel under the applied voltage. However, when the angle between the two electrodes was further increased to 30°, the mixing in the microchannel became much weaker than that in the parallel channel and 5° channel.

Fig. 4.26 shows the quantitative concentration distribution in the transverse direction with the AC signal. At streamwise position 9/4 w (w is the entrance width of the microchannel) away from the entrance (measured by pixel numbers in the image), Fig. 4.26, shows the concentration profiles for the three cases. The stronger the mixing, the more uniform the concentration (i.e. the fluorescence intensity here) in the transverse direction at a given streamwise position. The curve should approach flat when the fluids

are well mixed in the microchannel. In Fig. 4.26, the microchannel with $5°$ angle reached relatively uniform profile at 9/4 w from the entrance, while at the same *x* position the profile of the parallel channel was still far away from the flat profile. To achieve the similar uniform profile of the non-parallel micromixer, the parallel channel required a distance of 15/4 w from the entrance. In this sense, the data indicate that the mixing is approximately increased 40% in the microchannel with $5°$ compared with that in the parallel channel. Apparently the profile of the channel with $30°$ was much less uniform than that of the other two cases. Note that the concentration profile of the channel with $5°$ angle was not increased gradually from one side to the other. This could be due to the motion of the "large scale" vortex that generates convection transport of the scalar directly from one side to the other side of the channel.

This is a very interesting phenomenon. As we know that the mixing is increased with the increasing of the transverse electric field intensity, which is related to the ratio of voltage to the local distance between the electrodes. For a given voltage, the larger the distance, the smaller the strength of electric field $\vec{E}$. While in the case of parallel electrodes, the electric field strength is the same along the streamwise, it decreases along the streamwise direction in the case of non-parallel electrodes. Thus, it is supposed that the mixing should be weaker in the non-parallel microchannel, since it has lower electric field strength than the parallel microchannel does. However, with the same voltage, the non-parallel channel has a much more uniform distribution of concentration than the parallel channel does as shown in Fig. 4.26, which indicates that the non-parallel channel with $5°$ has stronger mixing than the parallel channel does.

From Fig. 2.1, we know that except $\vec{E}_y$ in the transverse direction there is a electric field $\vec{E}_x$ in the streamwise as well. Equations (2.4) and (2.5) show that there is electric force in streamwise direction if $\vec{E}_x$ is not zero. Consequently, the electric field distribution in the non-parallel channel was different from that in the parallel case. This implies that except $\vec{E}_y$ in the transverse direction, $\vec{E}_x$ in the streamwise direction plays a role as well for mixing enhancement. The experimental result confirms the prediction made in the theory section. The increase of $\vec{E}_x$ can prevail over the decrease of $\vec{E}_y$ for mixing enhancement. However, if the angle is further increased to $30°$, the electric field strength is so weak and the channel width is so wide that the mixing becomes poorer than that in the other two cases. Therefore, it is indicated that there is an optimized angle between the two electrically conductive sidewalls for mixing enhancement.

In addition, the flow in the expending channels is more unstable to small initial perturbations than that in the parallel channel as well recognized in fluid dynamics [223], because of the positive pressure gradient along the streamwise direction. Thus expending channel could enhance flow disturbance and hence, fluid mixing. This could be an additional reason why the mixing is stronger in the non-parallel channel with $5°$ angle, even if its electric filed is lower than that in the parallel channel. Thus, Fig. 4.25 and Fig. 4.26 provides us a new method to enhance mixing in microfludics based on electrokinetics, by using non-parallel channel with a small angle.

4.1.3.9 The effect of the AC signal phase shift between the electrodes

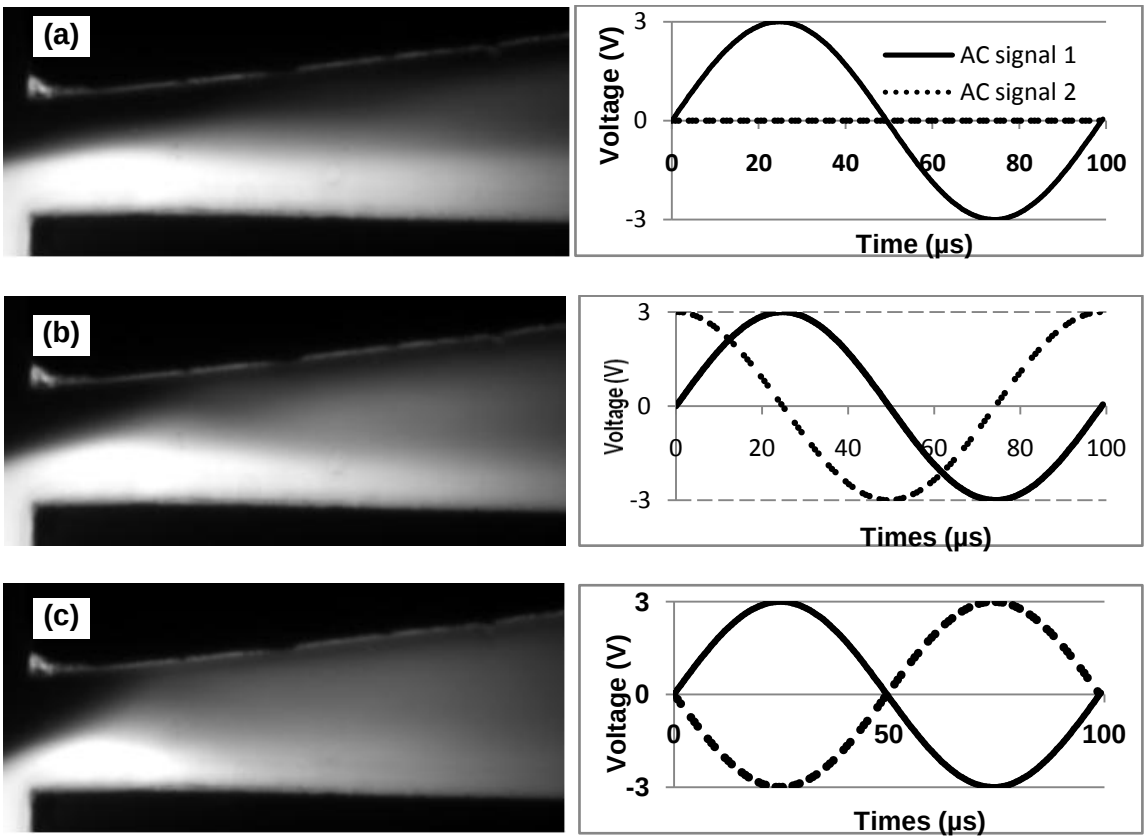

Figure 4.27 Comparison of mixing with different AC signal phase shifts. (a) One sine signal on one electrodes with another grounded; (b) 90 º; (c) 180 º.

The effect of the applied AC voltage phase shift between the two electrodes on the mixing process was also investigated inside the quasi T channel. In this experiment, γ of the two mixing streams and *f* of the applied voltage signals was kept constant, i.e. γ = 100 and *f* = 10 kHz. The flow rate of the two streams was kept at 5 μL/min. The effect of the phase shift difference between these two electrodes is displayed in Fig. 4.27, where there are three different cases. In the first case, one electrode was grounded and the other was supplied with an AC signal. In the second and third cases, the two electrodes were

provided with the same AC voltage signals, i.e. $V_A = V_B = 6\ V_{p\text{-}p}$, but different phase shifts of 90 ºand 180 ºrespectively.

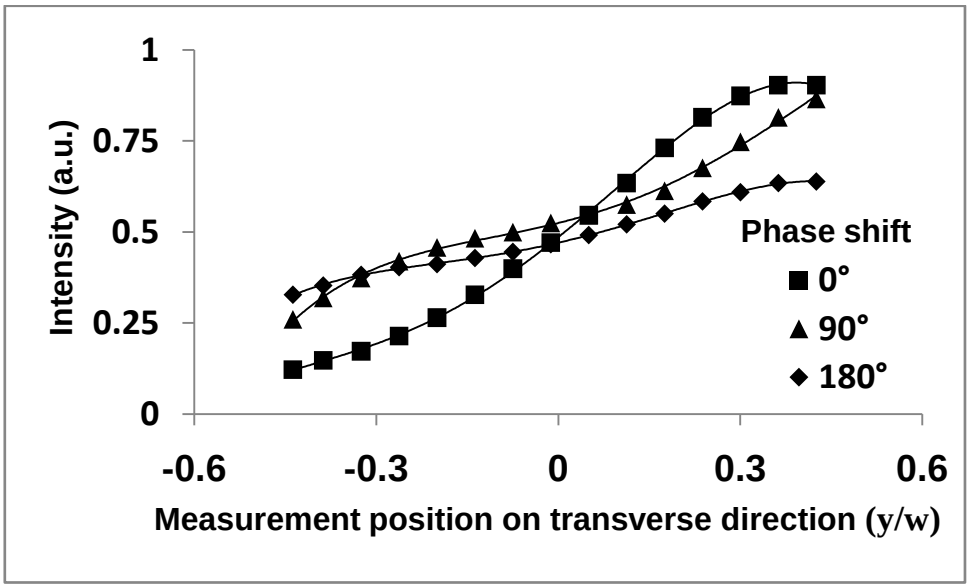

Figure 4.28 Comparison of concentration profile in transverse direction at x = 3/2 w from the channel entrance with different AC signal phase shifts.

Fig. 4.27(a) shows the fluorescence image with one electrode connected to the ground while the other to the AC voltage signal. Fig. 4.27(b) and (c) shows the fluorescence images under phase shift of 90 º and 180 º respectively. It is clearly shown that, the mixing was strongest under 180 º phase shift between the two electrodes. In comparison of these three cases, the mixing was relatively weak when AC signal was supplied to one electrode with the other one grounded. The mixing became stronger when AC signal was supplied to the two electrodes with 90 º phase shift. However, the mostly enhanced mixing was in the case with 180 º phase shift. Fig. 4.28 shows that the concentration profile became more uniform in the transverse direction under 180 º phase shift than that in the other two cases. Several other values of the phase shift between 0 and

180 º had also been tested, and none of them had stronger mixing than that under 180 º phase shift. This indicates that the mixing process is the strongest at 180 ºphase shift.

The higher the electric field, the stronger the electrokinetic force. Mixing will be increased with increased electrokinetic force. By applying voltage to both electrodes with 180 º phase shift, a stronger electric field can be achieved between the two electrodes as shown in Fig. 4.28. It can be seen that the maximum voltage difference in Fig. 4.27(a) – (c) is 3 V, 4.24 V and 6 V respectively. Therefore, the, strongest mixing is achieved under 180 ºphase shift. With one electrode grounded, the electric field turned to be much weaker than the one with voltage applied on both electrodes having 180 º phase shift. Hence, the mixing with one electrode grounded is not as strong as that with 180 ºphase shift. For the electric field with 90 º phase shift between the two electrodes, the maximum electric field is weaker than that with the 180 º phase shift, but stronger than that with one electrode grounded. Therefore, its mixing is weaker than that with 180 º phase shift, and stronger than that with one electrode grounded. This is another interesting phenomenon for mixing enhancement in microfluidics. In practice, the peak to peak voltage of a power supply may have limited value, especially if a function generator is used alone to provide the electric field. With phase shift of 180 º, the real AC electric field strength can be increased for mixing enhancement. To our best knowledge, this is the first study of the phase shift effect on mixing enhancement based on electrokinetics.

4.2 DEP cell separation

4.2.1 DEP separation of Colorectal cancer cell

The cell separation process in our DEP cell sorter is described as below. As target cells flow along the main channel and approach the gap between the electrodes pair, they experience a strong negative DEP force. On the one hand, the hydrodynamic force drives the cells in the flow direction of the main channel. On the other hand, the nDEP force repels the cell in the direction perpendicular to the electrodes in the gap. The effective net force of the nDEP and hydrodynamic force pushes the responsive cancer cells to the side channel. Without electrode activation, 90% of the cancer cells move downstream of the main channel and the other 10% flow through the side channel due to hydrodynamic splitting. Similarly, without electrode activation, 90% of normal HEK293 cells move downstream of the main channel and the other 10% flow through the side channel. However, when the electrodes are electrically activated, the cancer cells will be pushed only to the side channel, whereas the other cells keep their motion in the main channel. Thus, isolation of the cancer cells from other cells can be realized.

4.2.1.1 DEP spectrum measurement

Before the isolation of the cancer cells from others in the DEP sorter, we need to know whether the colorectal cancer cell has a negative DEP. To answer this question, we firstly measured the DEP spectrum using a wedge microfluidic chip, as shown in Fig. 4.29.

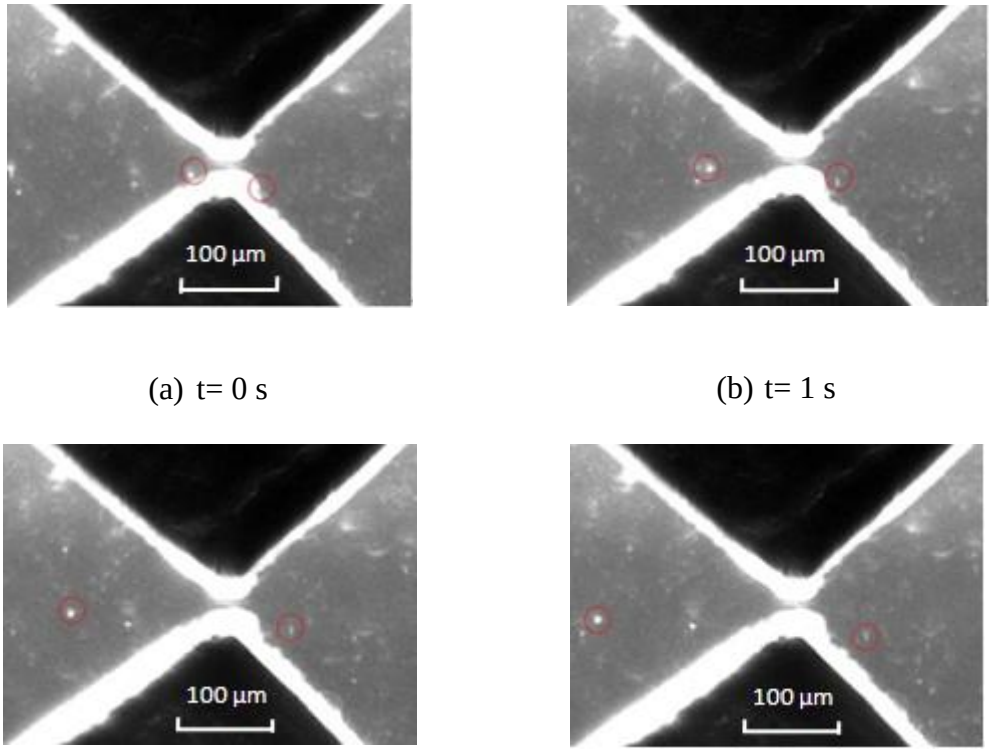

(a) t= 0 s (b) t= 1 s

(c) t= 2 s (d) t= 3 s

Figure 4.29 Motion of the colorectal cancer cells under nDEP force in a microfluidic chip with electrodes in wedge configuration for DEP spectrum measurement. (a) Two cells located near the electrodes tips are marked by red circles; (b) – (d) driven by the nDEP force, the two cells start moving away from the tips at different positions.

Since DEP spectrum is independent of the geometry of the electrodes and flow condition, a wedge chip was designed to measure the spectrum of the HCT 116 cells. The wedge was formed by two gold electrodes with thickness of 230 µm. The distance between their edges is 40 µm. With the sharp edges of the two gold electrodes, we can achieve a non uniform electric field required for the DEP. The HCT 116 cell solution will first be loaded into the wedge chip. The solution should be exactly the same as the one that will be used in the DEP sorter for cell separation. Since the solution in this chip is almost at rest, the effect of hydrodynamic force on the cells due to the pressure driven

flow is neglected. Hence, DEP force could become the major force on these cells, and could be easily observed and characterized, if it exists. For nDEP, the cells will move away from the tips, whereas for the pDEP, the cells will move towards the tips. The faster the motion, the stronger the DEP force. With this wedge DEP test microfluidic chip, a very small amount of sample (about 5 μL) is sufficient for measuring the DEP spectrum.

Fig. 4.29 shows the actual motion of the cells under the nDEP force, in the wedge microfluidic chip after electric activation of the electrodes. The time interval between consequence images, the AC frequency and voltage are 1 s, 100 kHz and 5 V_{p-p} respectively. It shows clearly that, when two sinusoidal electric signals with a phase shift of 180° are applied to the electrodes, the cells begin moving away from the two sharp tips, where the electric field intensity is the strongest. This means that these cells experience negative DEP force, which leads them move from the high electric field area to the low electric field region. The faster the motion, the stronger the nDEP force. Thus the DEP force can be estimated by measuring the cell flow velocity and the DEP spectrum can be obtained by measuring the velocity of the cell motion in the initial stage after the electric activation at various frequencies. Fig. 4.29 shows that cells were moving for relatively a long distance in a short period, *i.e.* 3 s in this case. In the light of the measured DEP spectrum, we could select the frequency to achieve either the nDEP force or pDEP force conveniently for the cell separation experiment. The HCT 116 cells' DEP spectrum is displayed in Fig. 4.30 for the given medium. Fig. 4.30 shows that in the frequency band of 1 Hz ~ 6 MHz and 31 MHz ~ 75 MHz respectively, the cancer cells experience a nDEP force, whereas in the frequency range of 6 MHz ~ 31 MHz the cells display a pDEP force. The motion of the cancer cells is sensitive to the AC frequency.

The cancer cells experience the approximately maximum nDEP at the frequency of 100 kHz, which was then selected for the DEP sorter to isolate the cancer cell.

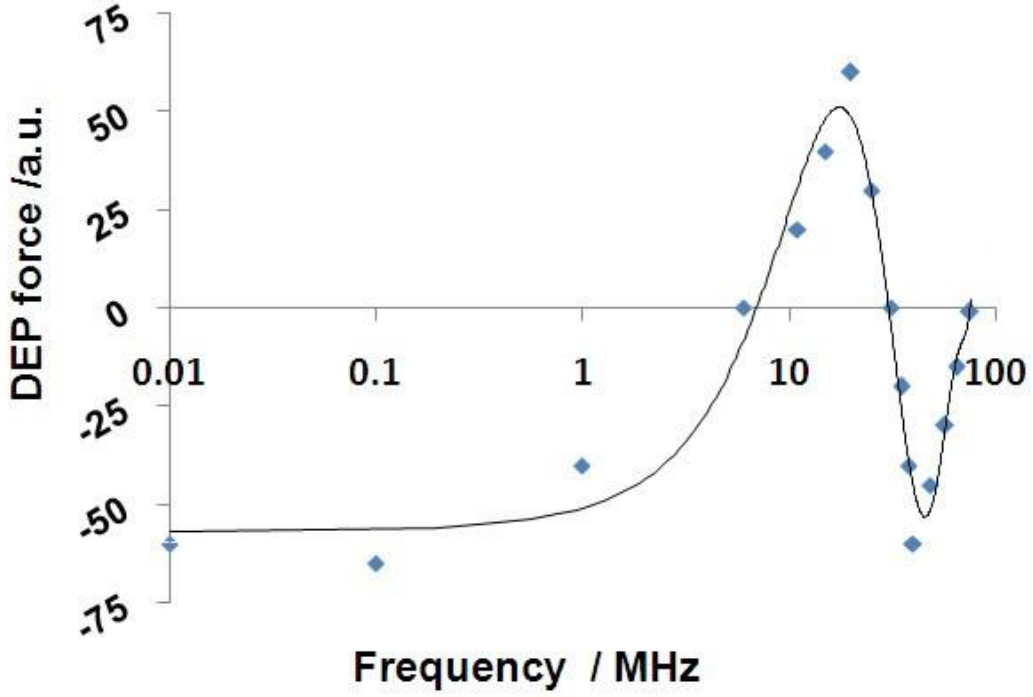

Figure 4.30 DEP spectrums of the HCT116 cells in a suspending medium with conductivity of 790 μs/cm. The cancer cells experience a nDEP force in the frequency band of 1 Hz ~ 6 MHz and 31 MHz ~ 75 MHz respectively, whereas in the frequency range of 6 MHz ~ 31 MHz they display a pDEP force.

4.2.1.2 Visualization of the DEP separation

Fig. 4.31 shows a visualization of the separation of HCT116 from the HEK 293 and *E. coli* cells due to DEP force in the microfluidic chip, with and without the electrical activation. The fluid flows from the inlet at the left side to the outlet at the right side in the main channel. In Fig. 4.31, the flow rate is 0.1 μL/min. In Fig. 4.31(a), approximately 90% of the colorectal cells flow through the gap between the two electrodes in the main channel without AC electrode activation. However, with the electric activation of the

electrodes at voltage of 16 V_{p-p} and frequency of 100 kHz, almost all colorectal cells migrate to the side channel under the nDEP force as shown in Fig. 4.31(b), whereas, the HEK 293 cells and *E. coli* remain the same motion through the gap as if there was no AC activation. Fig. 4.31 demonstrates that DEP has high specificity for cell separation and the HCT116 cancer cells can be separated from the HEK 293 and *E. coli* cells. Thus, DEP can provide an opportunity for cancer cell isolation from other cells.

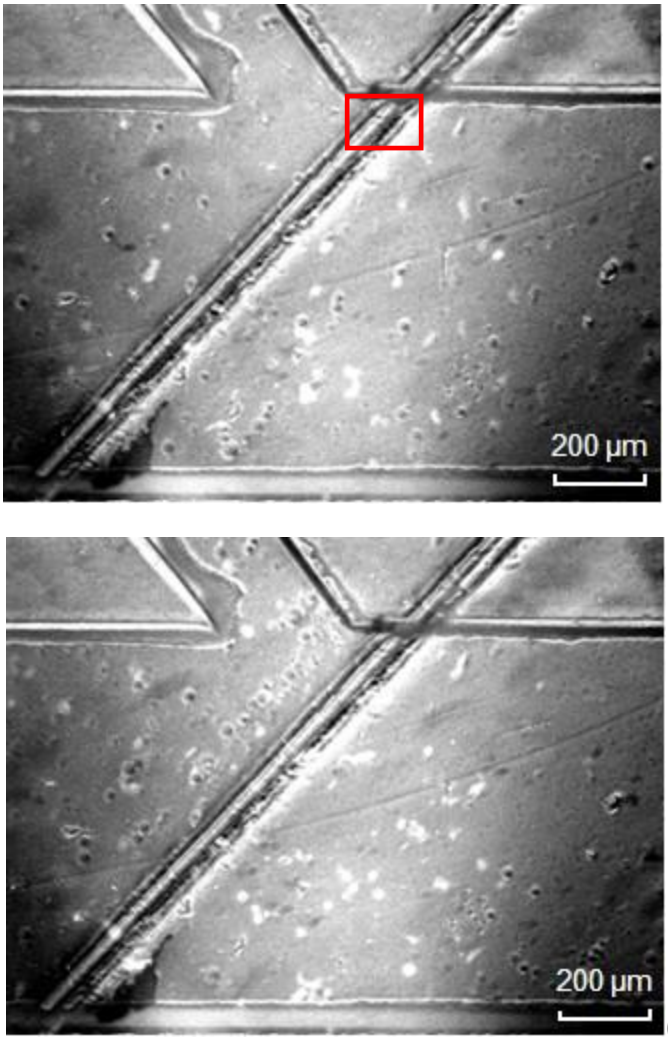

Figure 4.31 Experimental demonstration of the DEP deflection. (a) Without AC activation, most cells (colorectal cells, kidney cells and E. coli) flow through the electrode gap along the main channel. (b) With AC activation, almost all colorectal cells were repelled to the side channel due to negative DEP force, whereas the HEK 293 cells and E. coli retain the same motion through the gap as if there was no AC activation. The

dark spheres are the HCT 116 cells, and the white spheres are the HEK 293 cells. E. coli cells are too small to be seen in these images.

Due to their extremely small size compared with HCT 116 cells and HEK 293 cells, the *E. coli* cells cannot be seen in Fig. 4.31. Therefore, high magnification lens are needed to make the observation of the *E. coli* cell's behavior in the separation process unambiguous. The *E. coli* cells can be observed under 24X magnification, as shown in Fig.4.32, where the exposure time is 0.3 s and the time step between the two sequences is 1.5 s.

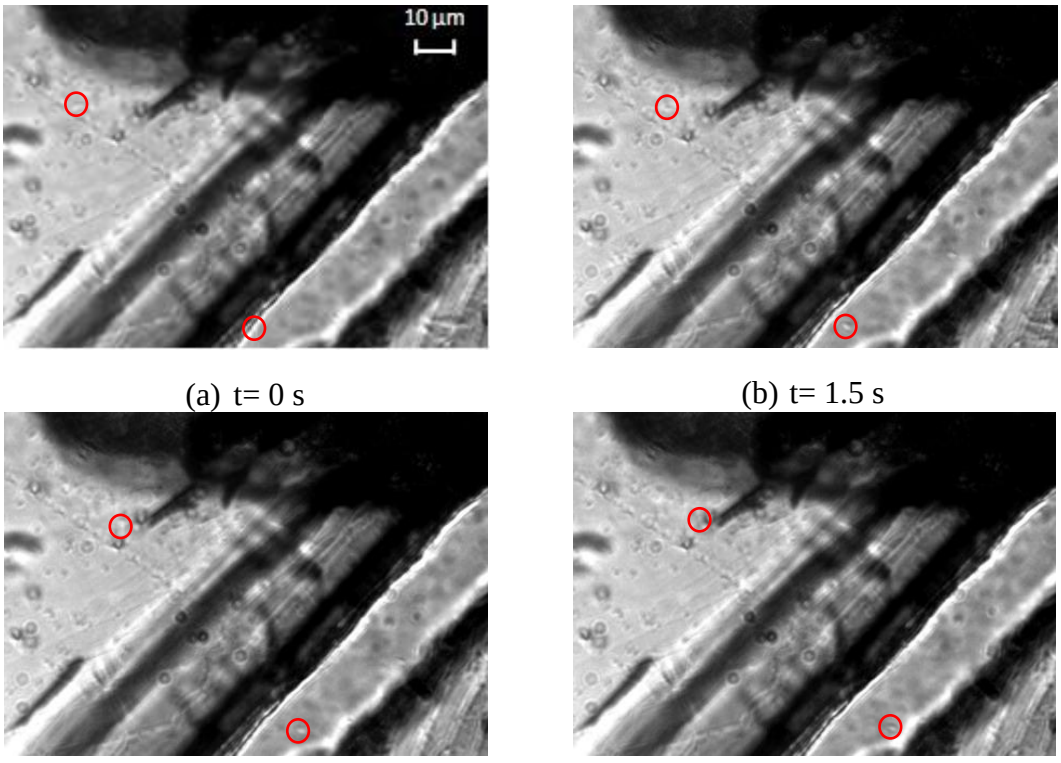

(a) t= 0 s (b) t= 1.5 s

(c) t= 3 s (d) t= 4.5 s

Figure 4.32 Experimental demonstration of the DEP deflection under 24X magnification. This is a zoom-in view for the field marked in Fig. 4.31(a).

As shown in Fig.4.32, the small *E. coli* cells flow along with the labeled HEK 293 cells. After the electric activation, the bacteria keep moving along the flow direction in the main channel with HEK 293 cells. This indicates that there is either no nDEP force or the DEP force is too small to deflect the *E. coli* to the side channel. This result matches our prediction that *E. coli* has negligible DEP force compared with cancer cells for separation that is based on cell size, since according to equation (2.8), DEP force is proportional to cube of the particle's radius and *E. coli* is much smaller than the cancer cell. This result also shows that with large differentiation in particle or cell's radius a, size based DEP separation could also be leveraged for separation. This is one of the traditional methods for DEP selectivity.

4.2.1.3 Enrichment factor

4.2.1.3.1 Flow rate effect

The measured enrichment factor as a function of the sample flow rate at constant voltage of $16V_{p\text{-}p}$, is shown in Fig. 4.33. It is noted that the enrichment factor decreases with the flow rate, since the hydrodynamic force experienced by the cancer cells increases with the increased flow rate. The total force that the cells experience is the sum of the vector forces of DEP and hydrodynamics. The hydrodynamic force mainly pushes the cells to flow along the main channel. At high flow rate, due to the large hydrodynamic force, it is very difficult to deflect the cells to the side channel. Thus, hydrodynamic force and DEP force are competitive. The higher the flow rate, the lower

the enrichment factor. When the flow rate is less than 0.1 μL/min, the enrichment factor is 98%, indicating that the DEP force is much larger than the hydrodynamic forces. However, when the flow rate increases to 0.2 μL/min, the hydrodynamic force overwhelms DEP with resultant minimal deflection of cancer cells.

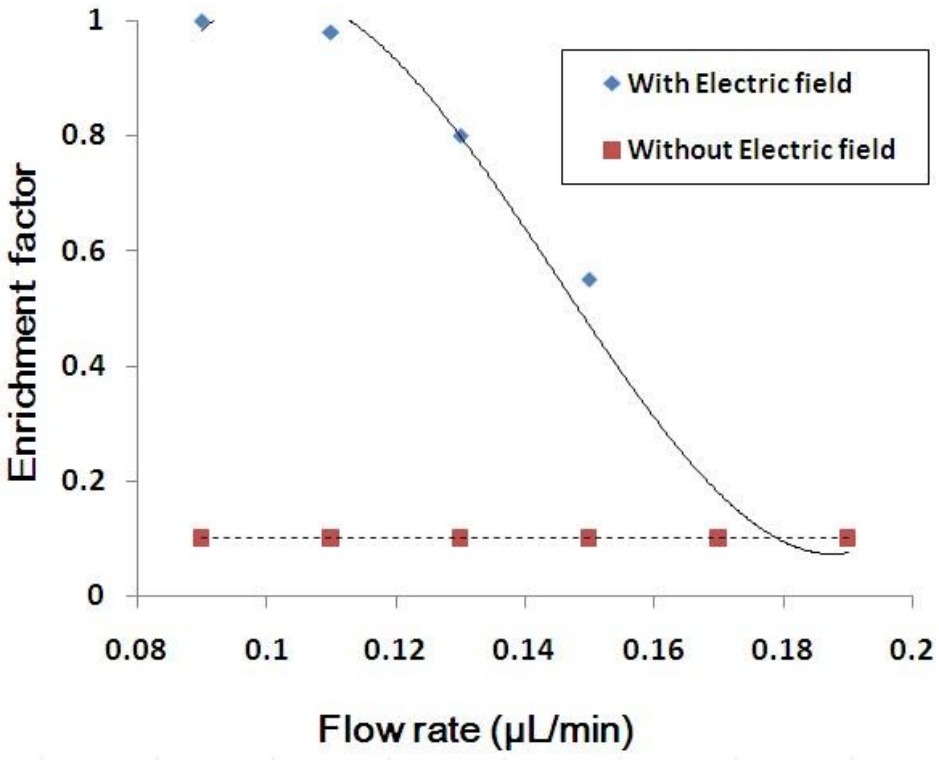

Figure 4.33 Enrichment factor as a function of the sample flow rate.

4.2.1.3.2 Voltage effect

The effect of applied voltage on the DEP separation is shown in Fig. 4.34, which indicates that the enrichment factor increases with increased electric field (or equivalently voltage). The flow rate in Fig. 4.34 was maintained constant at 0.1 μL/min.

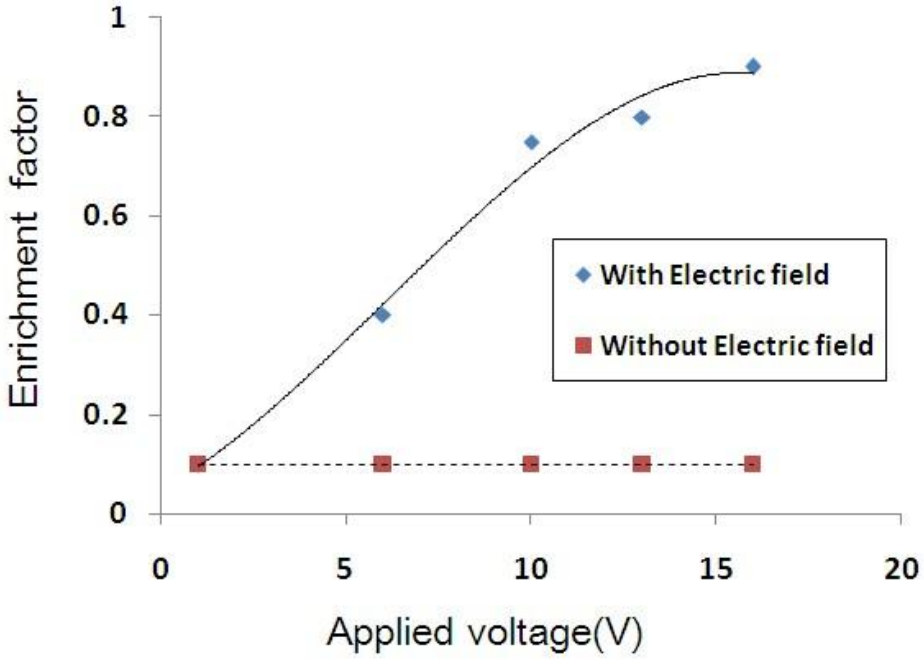

Figure 4.34 Enrichment factor as a function of applied voltage.

As we can see from equation (2.8), DEP force increases with the increased gradient of the square of the electric field (or equivalently voltage). Consequently, enrichment factor is rapidly increased with the increase of the voltage within the test range of the voltage. Fig. 34 indicates that increasing the voltage could be an easy way to enhance the DEP enrichment factor.

4.2.1.3.3 Purification

One of the objectives of the DEP separation is to purify the cancer cells for sample preparation in clinical diagnostics. To quantify the DEP purification of the colon cancer

cells, we estimated the concentration of the colon cancer cell in the side channel with and without the electrical activation. To simplify the calculation, we only focus on the HCT116 and HEK 293 cells, since *E. coli* is too small to see clearly. The result is given in Fig. 4.35, where the concentration of the HCT 116 cells is 57% before the electric activation. However, with the electric activation on the DEP sorter, the concentration of HCT 116 cell was increased to 95% in the side channel. Another way to quantify the purification is the ratio of cell number of HCT116 cell to that of HEK 293 cell. As shown in Fig. 35, the ratio in the side channel with and without the electric activation is 17.4 and 1.3 respectively, i.e. approximately increase of 13 folds. With such a simple device, Fig. 4.35 demonstrates the capability of the DEP sorter to separate and purify the cancer cells.

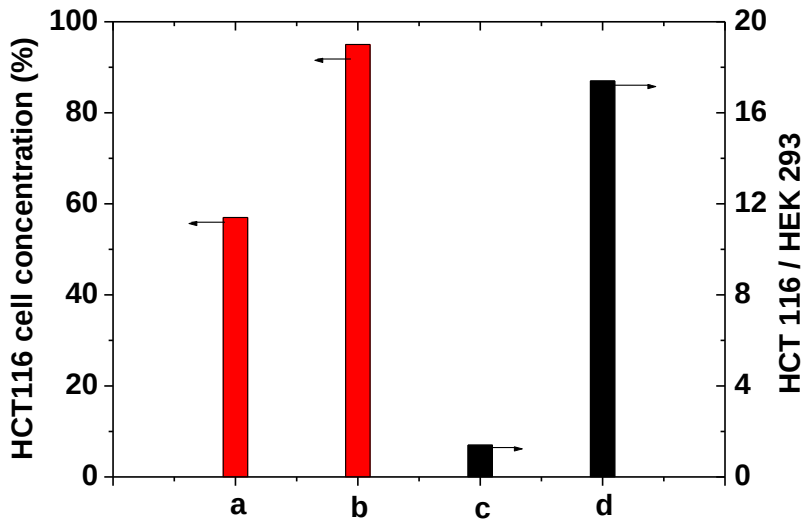

Figure 4.35 Quantitatively comparison of HCT116 cell purification at the entrance of the side channel. (a) HCT 116 cell concentration without electric field, (b) HCT 116 cell concentration with electric field, (c) cell number ratio of HCT 116 / HEK 293 without electric field, and (d) cell number ratio of HCT 116 / HEK 293 with electric field.

In above works, dielectrophoresis principle is applied to the isolate the HCT116 colorectal cancer cell from HEK293 kidney cell and E-coli bacteria based on cell dielectric property, e.g. permittivity, conductivity and size. A given cell may have a specific dielectric property that is different from that of other cells. Such a difference may be leveraged for DEP separation. Since the structure of our DEP sorter is very simple, it should be easy to be integrated and applied to other system as well, as long as the electrodes can be built in the channel. However, in clinical application, the separation of the colorectal cancer cells from other cancer cells or epithelial cells could be required and could be more difficult; as shown in Fig. 4.33, the enrichment factor decreases with increase of flow rate. In practice, often high throughput is required, which in turn, demands high flow rate. Fortunately, as shown in Fig. 4.34, the enrichment factor increases rapidly with the voltage. Therefore, both multiple parallel channels and higher voltage could be used in high throughput to ensure high enrichment factor, so that sufficient amount of interested cells can be isolated and collected for assays downstream. Another method is to add another electrode pair on the top side of the channel, opposite to the electrode pair on the bottom side. In this case, the electric field could be higher to increase the enrichment factor.

4.2.2 LNCaP prostate cancer cells separated from HCT116 colorectal cancer cells

4.2.2.1 DEP spectrum

Firstly, by using a simple wedge microchip [224], the dielectrophoresis character of LNCaP prostate cancer cell and HCT116 colorectal cancer cells under different

suspending medium conductivities were also measured. In another word, we investigated the DEP force's relative strength and direction (positive or negative) along with the applied AC frequencies (DEP spectrum), for both kinds of the cancer cell.

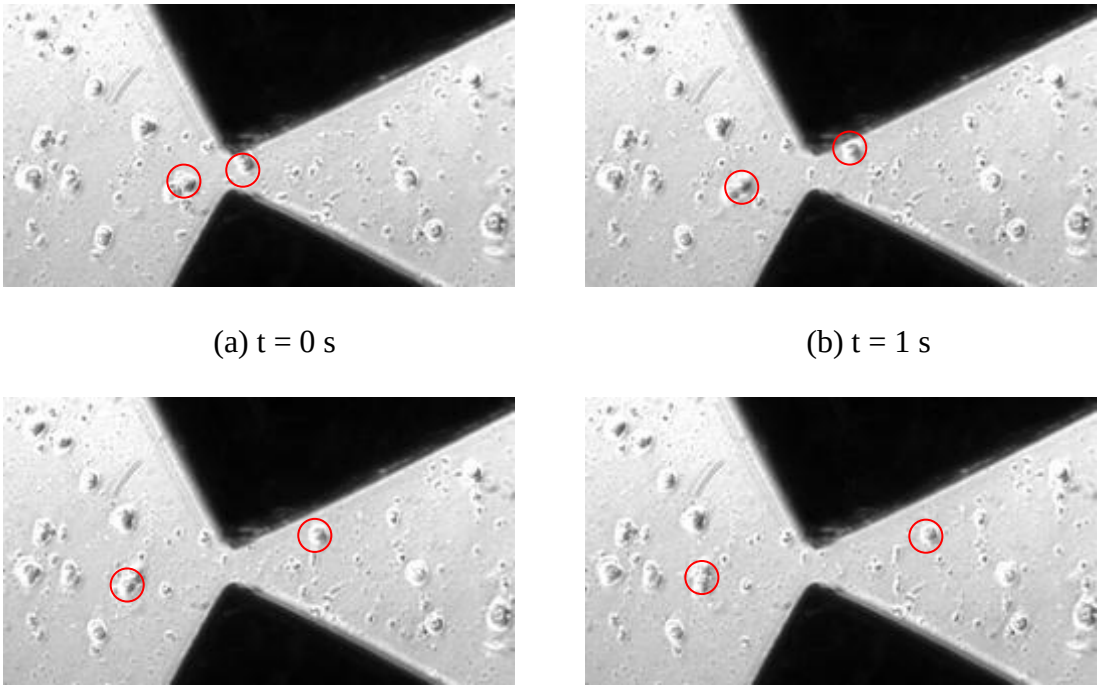

(a) t = 0 s (b) t = 1 s

(c) t = 2 s (d) t = 3 s

Figure 4.36 Prostate cancer cells moving under nDEP force in a wedge chip. (a) Two cells locate near the electrodes tips are marked by red circle. (b) Driving by nDEP force, these two cells start moving away from the tips. (c) These two cells are keeping move away from tips. (d) After three seconds, these two cells are far away from the tips.

The DEP spectrums of both kinds of cell were measured in the wedge chip, as shown in Fig.4.36. Two gold electrodes with thickness of 230 μm were used to form the wedge. The distance between their edges was 40 μm. A non-uniform electric field required for the DEP force was generated between the sharp edges of the two gold electrodes. Solution of each kind of cell was first loaded into the wedge chip. Since the solution in this chip was almost stationary, the effect of hydrodynamic force on the cells

due to the pressure driven flow was neglected. Therefore, DEP force can become the major force on these cells, and can be observed and characterized, as long as it exists. For nDEP, the cells will move away from the tips, whereas for the pDEP, the cells will move towards the tips, once an electric field is switched on. We recorded the movement by the CCD camera at a fixed frame rate and a fixed exposure time, and then by measuring the distance of the cell's movement in a fixed time period (50 frames for each measurement), we could calculate the mean velocity, which is directly related to the force. The highest velocity is used for normalization of the DEP force. The faster the motion, the stronger the DEP force. For each frequency, we repeat 3 measurements and the standard deviations of DEP force are shown in the spectra as error bars. With this wedge DEP chip, a very small amount of sample (about 5 μL) is sufficient for measuring the DEP spectrum.

Specially, from equation (2.9) and (2.10), the Clausius-Mossotti factor K is affected by the conductivity of the suspending medium and the cell. Consequently, suspending medium's conductivity could affect the DEP force on suspending cells. Therefore, DEP spectrums for each kind of cell suspended in medium with different conductivity have been also investigated.

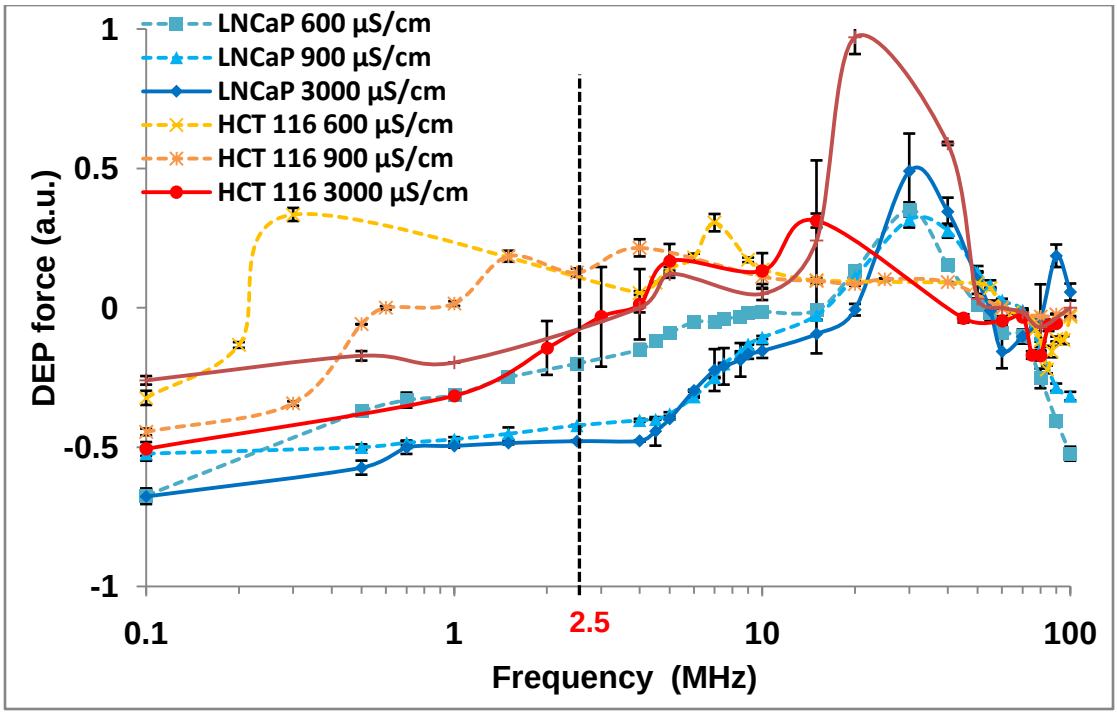

Figure 4.37 DEP spectrum of LNCaP prostate cancer cell and HCT116 colorectal cells.

Fig. 4.37 shows the DEP spectrums for both LNCaP cells and HCT116 cells, measured by the wedge DEP test chip. Three different concentrations of PBS buffer were used, 0.025X PBS, 0.05X PBS and 0.1X PBS, whose conductivity were 600 µS/cm, 900 µS/cm and 3000 µS/cm, respectively. However, further increasing conductivity of suspending medium will have high risk of generating bubbles in the solution when voltage is supplied, due to electrolysis. Result showed that, in our experiment, the DEP spectra were different in different suspending medium's conductivities. By comparing spectra of LNCaP cell with that of HCT 116 cell, one could see that in 0.1X PBS medium, the cross-over frequency where the DEP force was zero, was 2.5 MHz for HCT 116 cells. Meanwhile, LNCaP cells experienced an nDEP force at the same frequency. On the other hand, when we compared spectra in the media with three different conductivities, the

DEP force difference between LNCaP and HCT116 cells was largest in the medium of 3000 μS/cm (0.1X PBS). This suggested that by using this medium, LNCaP cells would experience the relatively stronger nDEP force at the cross-over frequency for HCT116 cells. Therefore, in the following experiments, we focused on the medium with conductivity of 3000 μS/cm.

In the medium with conductivity of 3000 μS/cm, , in the frequency band of 1 Hz ~ 20 MHz and 55 MHz ~ 70 MHz, the LNCaP cells experienced an nDEP force, whereas in the frequency range of 20 MHz ~ 55 MHz and 70 MHz ~ 100 MHz, the cells experienced a pDEP force. At the mean time, , in the frequency band of 1 Hz ~ 2.5 MHz and 60 MHz ~ 100 MHz HCT116 cells experienced an nDEP force, whereas in the frequency range of 2.5 MHz ~ 10 MHz, the cells experienced a pDEP force. By analyzing these two curves, we could see that at the frequency of 2.5MHz, LNCaP cells experienced a strong negative DEP force while the DEP force acting on HCT116 cells was around zero. This indicated that, by applying AC electric field with this particular frequency in the DEP sorter, LNCaP cells should be repelled by the nDEP force and flow to the side channel, and meanwhile the HCT116 cells would keep flowing to the end of main channel without blocking by either pDEP or nDEP force. Furthermore, DEP force of labeled HCT116 cells had also been measured to be almost zero at 2.5 MHz, which suggested the usage of dye on HCT116 cells had no influence on separation results for the current separation experiment at 2.5 MH. Therefore, 2.5 MHz, which was the cross-over frequency of the HCT116 cell, was selected for the DEP sorter to isolate the LNCaP cells from the HCT116 cells. Specially, although these is a spectral difference between HCT 166 cell and labeled HCT 116 cell, which could be caused by the permittivity

change of the HCT116 cell, the DEP response are luckily very close at the frequency we use to separate LNCaP cells from HCT 116 cells. Base on this fact, we can use labeled HCT 116 cells just for visualization purpose. In real applications, the HCT 116 cells are not necessary to be labeled.

4.2.2.2 Separation of LNCaP cells and HCT116 cells

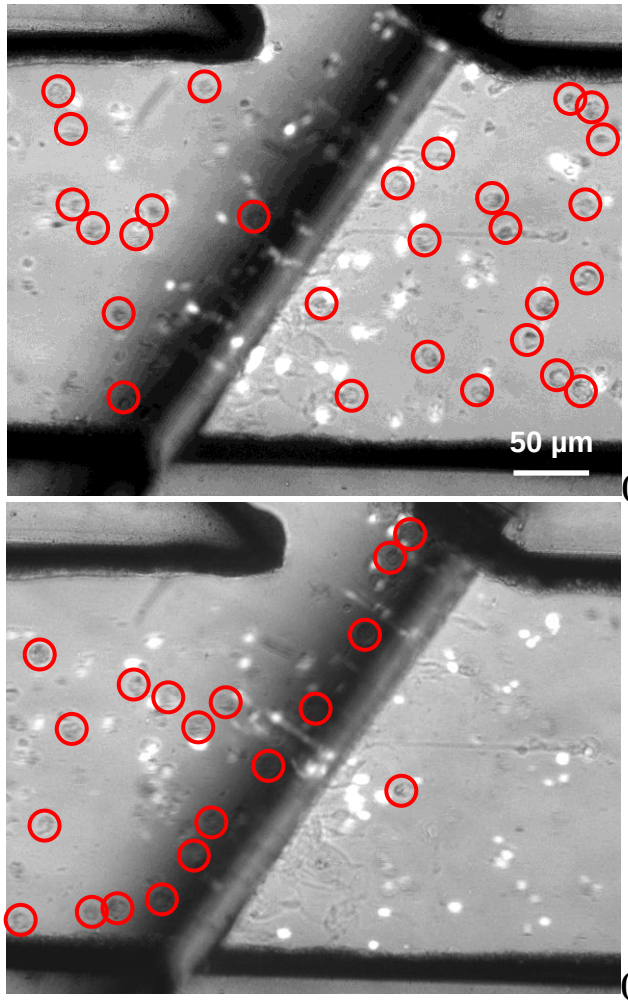

Figure 4.38 Experimental demonstration of the DEP deflection. (a) Without AC activation, most cells (LNCaP cells, HCT116 cells) flowed through the electrode gap along the main channel. (b) With AC activation, almost all LNCaP cells were repelled to the side channel due to negative DEP force, whereas only HCT116 cells could be seen retaining the same motion through the gap. The dark spheres are LNCaP cells, and the bright spheres are HCT116 cells.

Fig. 4.38 shows the visualization of the separation of LNCaP cells from HCT116 cells due to nDEP force in the DEP cell sorter, with and without the electrical activation. The fluid flowed from the inlet at the left side to the outlet at the right side in the main channel (about 80% of the inlet flow rate) and the side channel (about 20% of the inlet flow rate) at a total inlet flow rate of 0.15 μL/min. In Fig. 4.38(a), approximately 80% of LNCaP cells flowed through the gap between the two electrodes in the main channel without AC electrode activation. However, with the electric activation of the electrodes at voltage of 12 V_{p-p} and frequency of 2.5 MHz, almost all prostate cancer cells migrated to the side channel under the nDEP force as shown in Fig. 4.38(b), whereas, HCT116 cells remained the same motion through the gap. Fig. 4.38 demonstrates that DEP can be used for isolation of LNCaP cells from HCT116 cells. Thus, DEP could provide an opportunity for isolation of one type cancer cell from other similar epithelial and cancer cells.

4.2.2.3 Quantitative analysis of LNCaP cells separation

4.2.2.3.1 Flow rate effect

Sample flow rate effect on η is shown in Fig. 4.39. In this experiment, applied voltage was kept at 13 V_{p-p} under selected frequency of 2.5 MHz. 100 captured frames and a fixed frame rate were used to calculate η. For each flow rate, we repeat 3 measurement and standard deviations were represented as error bars. Fig. 4.39 indicates that η decreases with the increase of the flow rate Q. The enrichment factor was almost a constant of around 96%, as long as Q was less than about 0.4 μL/min, indicating that the

DEP force was much larger than the hydrodynamic forces. However, as Q was larger than 0.4 μL/min, η decreased rapidly with the increased Q. When Q reached 0.8 μL/min, the hydrodynamic force overwhelmed the DEP force, resulting in almost no deflection of LNCaP cells and the device had almost no effect of cell enrichment. Since the side channel must have a small portion of flow to carry the isolated target cells to a collection well, there will always be a small portion of the targeted cells (about 20%) that follow this portion of fluid and flow into the side channel. Therefore, the enrichment factor cannot be lower than 0.2, even the flow rate was further increased.

As we know the total force $\vec{f}_{SUM}$ on cells is the sum of $\vec{f}_{DEP}$ and $\vec{f}_{h}$, as shown in equation (2.18). $\vec{f}_{hx}$ mainly pushes the cells to flow along the main channel, while $\vec{f}_{DEPx}$ acts against the hydrodynamic force and $\vec{f}_{DEPy}$ pushes the target cells to the entrance of the side channel. $\vec{f}_{DEPx}$ counter balances $\vec{f}_{hx}$ so that there can be sufficient time for the target cells to be pushed to the entrance of the side channel by $\vec{f}_{DEPy}$. Once the cells arrive the entrance, they will move to the side channel due to the hydrodynamic force there. At high Q, due to the large hydrodynamic force, it is very difficult to deflect the targeted LNCaP cells to the side channel. Thus, hydrodynamic force and DEP force are competitive.

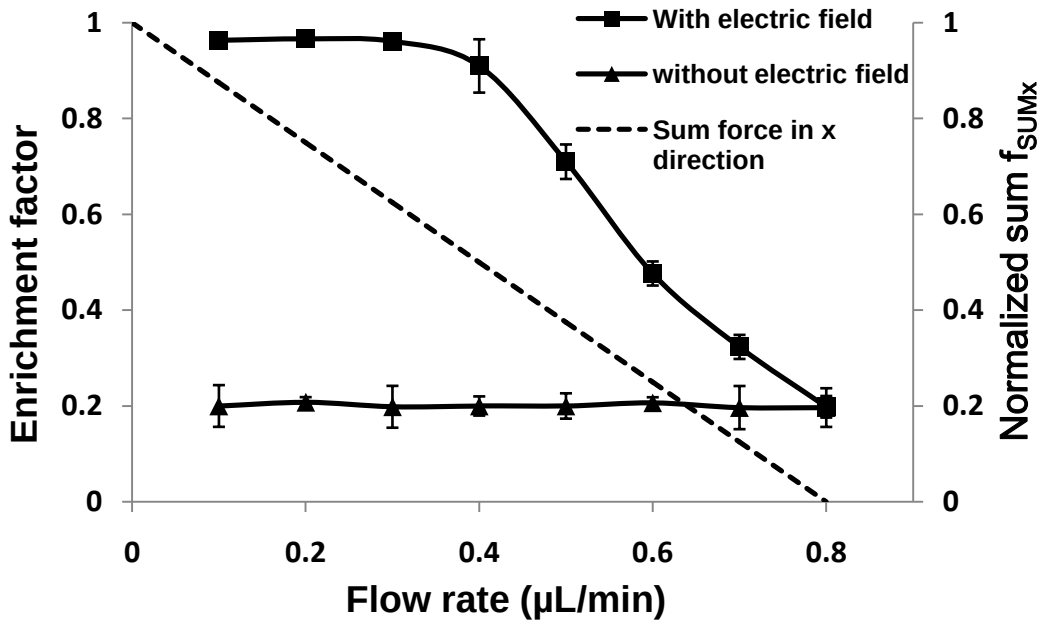

Figure 4.39 Enrichment factor and normalized f^*_{SUMx} as a function of the sample flow rate Q.

To explain the flow rate effect shown in Fig. 4.39 based on force, we normalize the f_{SUMx} by following equation:

$$f^*_{SUMx} = \frac{f_{DEPx} - f_{hx}}{f_{DEPx}} \tag{4.4}$$

According to this equation, when f_{hx} is zero (Q is zero), f^*_{SUMx} equals to 1. When $f_{DEPx} = f_{hx}$, f^*_{SUMx} become zero. During the experiment of characterizing flow rate effect, the DEP force should be kept constant. When f_{DEPx} is as large as f_{hx}, the target cells could be decelerated to zero along x direction from their initial velocity near the electrode pair, so that they can be pushed to the entrance of the side channel. However, since the cells are initially moving with the bulk velocity, f_{DEPx} has to be larger than f_{hx}, in order to ensure that cells near the side opposite to the side wall can be pushed to the

side channel entrance. Therefore, we assume that when Q is increased up to $f_{hx} = f_{DEPx}$, there will be no enrichment anymore, and when Q is decreased down to $f_{hx} = 0$, the enrichment will be the maximum, i.e. 1. Furthermore, since f^*_{SUMx} is linearly proportional to f_{hx} as shown in the equation (2.20), we can get the linear relation between f^*_{SUMx} and Q as shown in Fig. 4.39. For guidance in design and operation of the DEP sorter, Fig. 4.39 indicates approximately that if f^*_{SUMx} is lower than 0.5, η will decrease rapidly with Q. However if f^*_{SUMx} is higher than 0.5, η reaches nearly the highest, and further decrease of Q will not improve η significantly.

4.2.2.3.2 Voltage effect

The effects of applied voltage on the DEP separation under three different flow rates were investigated, which were 0.15 μL/min, 0.3 μL/min and 0.4 μL/min, respectively. 100 captured frames and a fixed frame rate were used to calculate η. For each applied voltage, we repeat 3 measurement and standard deviations were represented as error bars.The results are shown in Fig. 4.40, which indicates that, under each Q, η increases with increasing electric field (or equivalently voltage). On the other hand, it is also shown in Fig. 4.40, under the same applied voltage, the enrichment factor of a higher Q is lower than that of a lower Q. This is also because that a higher Q causes a stronger hydrodynamic force on cells, to push the LNCaP cells to flow along the main channel. Therefore at a higher Q, a stronger nDEP force is required to repel cells to the side channel.

At a relatively low flow rate, e.g. Q = 0.15 μL/min, Fig. 4.40 shows that η reaches a relative high enrichment factor 0.86 when applied voltage is 10 V_{p-p}. This means that for a low Q, a low voltage can be sufficient to achieve a high η. However, as shown in Fig. 4.40, for the higher Q of 0.3 and 0.4 μL/min, at the same applied voltage of 10 $V_{p-p,}$ η reaches only to 0.68 and 0.5 respectively. When we further increase applied voltage to 14 $V_{p-p,}$ η under these higher Q are increased to high level of 0.95 and 0.93 respectively. After all, Fig. 4.39 and 4.40 indicate that increasing the voltage and decreasing flow rate could be two easy ways to enhance the enrichment factor.

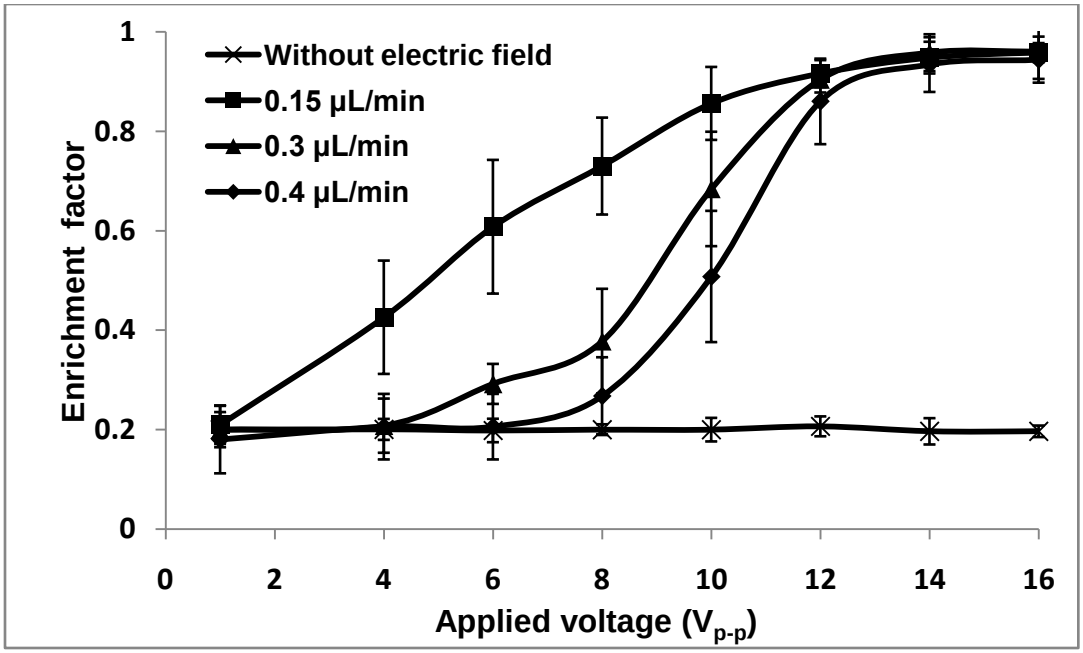

Figure 4.40 Enrichment factor as a function of applied voltage under different flow rates.

From equation (2.8), f_{DEP} increases with the increased electric field (or equivalently voltage), the higher voltage, the stronger f_{DEP}. The stronger f_{DEP} is, the

more cells near the side wall opposite to the side channel will be repelled to the side channel. This is not only because a strong f_{DEPx} can counterbalance the motion of cells due to f_h before they achieve electrodes pair in *x* direction, but also because a strong f_{DEPy} pushes up the cells to move faster to the side channel in *y* direction. Consequently, η rapidly increases with the increased voltage within the test range of the voltage for a given flow rate.

4.2.3 Cascade and staggered dielectrophoretic cell sorters

4.2.3.1 Separation of different size particles

Particle size is a key effective parameter, which influences the DEP force on a particle. Therefore separation of two kinds of particles with different sizes is relatively easy to achieve, due to their obvious DEP force difference at a certain applied frequency. Hence, to demonstrate the separation process in the cascade and staggered side channel DEP cell sorters, two kinds of different size fluorescent particles were first separated in both sorters.

4.2.3.2 Cascade chip to increase purity

In the experiment of the cascade DEP cell sorter, Q was kept at 0.3 μL/min, and a sinusoidal signal was applied to the two electrode pairs with a 180° phase shift. The voltage and frequency of the applied signal were 20 Vp-p and 10 MHz respectively (At this frequency, the particles experienced high nDEP force [51, 52], measured by a straight forward wedge DEP chip [39]). Under these conditions, the two kinds of particles

were separated in the cascade chip, as shown in Fig. 4.41. The fluid flowed from the inlet at the left side to the outlet at the right side in the main channel.

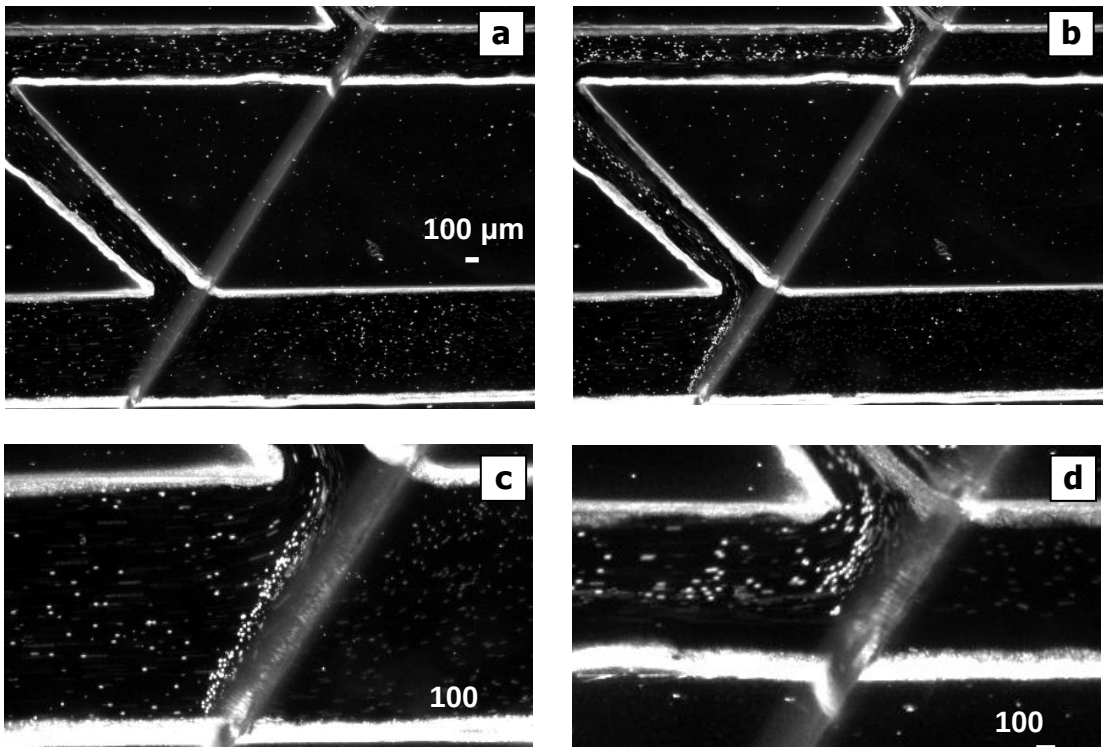

Figure 4.41 Visualization of DEP separation of 6-µm and 3-µm particles in the cascade DEP cell sorter. (a) Without AC activation, all particles flowed mostly through the electrode gap. (b) With applied AC signals, almost all 6-µm particles were repelled to the side channel due to the nDEP force. Then in the second main channel, 6-µm particles were separated again from the 3-µm particles before the second electrode pair. (c) Zoom-in view of particle separation near the first electrode pair. (d) Zoom-in view of the separation near the second electrode pair.

As shown in Fig. 4.41, 6-µm particles were isolated from the premixed solution of the two kinds of particles in the cascade DEP cell sorter. Fig. 4.41(c) and (d) give clearer view of the separation of both kinds of the particles near the electrode pairs in the first and second main channel. The results suggest that the cascade DEP cell sorter not only has the capability of isolating and enriching target particles, but also has the capability of improving P of isolated particles. Note that the streaklines between the two electrodes in

Fig. 4.41(d) were caused by the particles' light reflection from the side wall surface (facing the particles) of the glass gap. These particles that generated the streaklines were right upstream the electrode pair. Similar streaklines can be observed in other figures below.

4.2.3.3 Staggered side channels to increase throughput

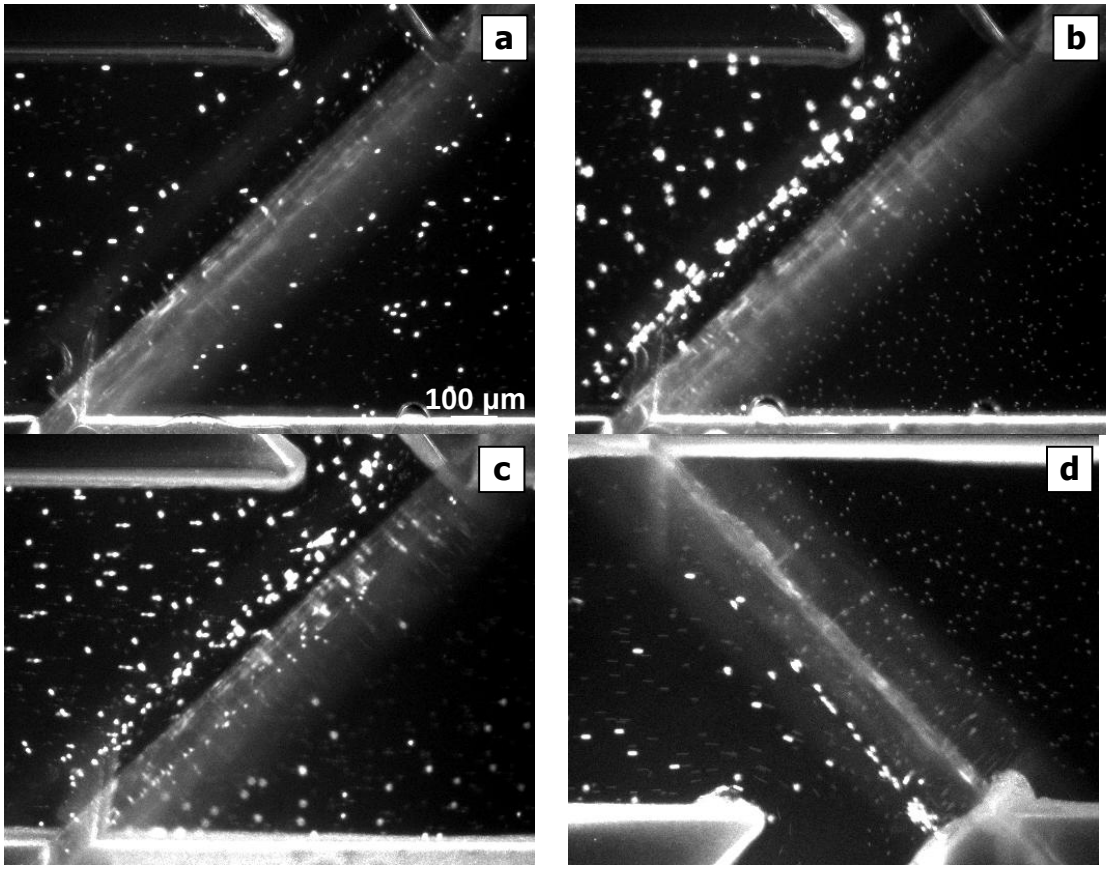

Figure 4.42 Visualization of separation of the 6-µm and 3-µm in the staggered side channel DEP cell sorter. (a) Without AC activation, all particles flowed through the electrode gap. (b) With applied AC signals, most of 6-µm particles were repelled to the first side channel due to the nDEP force, at low *Q* of 0.3µL/min. (c) While most of 6-µm particles were repelled to the side channel when the high *Q* of 0.6 µL/min was used, some 6-µm particles passed over the electrode gap and escaped to the main channel. (d) At the second electrode pair, those escaped 6-µm particles were repelled by the second electrode pair to the second side channel, but 3-µm particles remained flowing down to the end of the main channel.

In the experiment of the DEP cell sorter having two staggered side channels (each of which has an electrode pair), a relatively low Q of 0.3 μL/min and a relatively high Q of 0.6 μL/min were used. The voltage and the frequency of the applied signal were 20 Vp-p and 10 MHz respectively. Under these conditions, the two kinds of particles were separated in the DEP cell sorter, as shown in Fig. 4.42.

As shown in Fig. 4.42, 6-μm particles were separated from the 3-μm ones in the DEP cell sorter with the staggered side channels. These results suggest that this staggered side channel DEP sorter, compared with the single side channel sorter, has the capability of keeping high η, even though the sample throughput is increased.

4.2.3.4 Separation of prostate cancer cells (LNCaP) and colorectal cancer cells (HCT116)

One of the major goals of developing these DEP cell sorters was to manipulate and isolate biological cells. In the present work, for demonstration, we kept our selection of LNCaP prostate cancer cells as the target cells for isolation from HCT116 colorectal cancer cells. These two types of cells were relatively difficult to separate, since they are similar in diameter (around 20 μm) and are both epithelial cancer cells. The DEP force difference between these two types of cells was mainly due to their different dielectric properties. To separate them, selection of the AC frequency was crucial. According to the measurement of DEP spectrum of each cell type by a wedge chip we fabricated earlier [39], it was found that at the frequency of 2.5 MHz, we could efficiently separate these two types of cells, since at this frequency, while HCT116 cells had a negligible DEP force (the cross-over frequency for LNCaP was 20 MHz), LNCaP cells experienced a relatively strong nDEP force (Unless specialized, the applied frequency was kept at 2.5

MHz). Increase of purity in cascade sorter and increase of throughput without compromising the enrichment factor in the staggered sorter were investigated. The purity represents the ratio of target particles number T collected in the side channel to the total particles number ($T + N$), collected in the side channel, and the enrichment factor is the ratio of target particles blocked by the nDEP force to the total target particles or cells that flow into the sorter.

4.2.3.5 Cell separation in the cascade DEP cell sorter

In the experiment of the cascade sorter, the sample Q was kept at 0.15 μL/min, the voltage of applied signal was 12 Vp-p. Visualization of the separation between the LNCaP and the HCT116 cells in the cascade sorter is given in Fig. 4.43, with and without the electrical activation. In Fig. 4.43(c), it is shown that in the second main channel, LNCaP cells were again repelled to the side channel due to the nDEP force, but the HCT116 cells were not. By this process, P of isolated LNCaP cells was further enhanced.

To quantify and characterize the purification of the prostate cancer cells from the cascade sorter, we estimated P of the prostate cancer cells (prostate cancer cells number divided by total cells number) in the side channel. Cells entered into the side channel were counted based on movie obtained from the visualization (the same movie of Fig. 4.43). Tests were repeated 5 times to obtain average value and error bar. As shown in Fig. 4.44, purities of LNCaP at the entrance of the side channel were compared for three cases: without AC signal, with AC signal in a single electrode pair sorter, and with AC signal in a cascade configuration sorter.

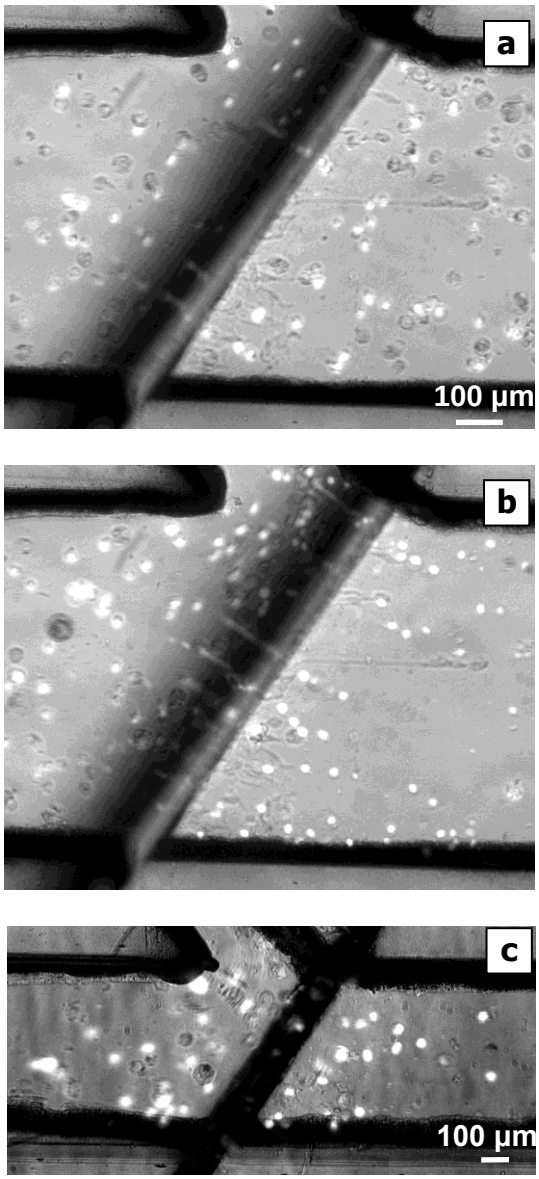

Figure 4.43 Visualization of the separation of LNCaP and HCT116 cells in the cascade sorter. (a) Without AC activation, most cells flowed along the main channel. (b) With AC activation, LNCaP cells were repelled to the side channel, when a small portion of HCT116 cells also flowed in the side channel (c) Most LNCaP cells were repelled to the second side channel, while most HCT116 cells passed over the gap. The dark spheres were the LNCaP cells, and the bright spheres are the HCT116 cells.

Without electric field activation, the LNCaP cells and HCT116 cells had the same possibility to enter the side channel with portion of fluid that flowed into each side channel, therefore, the percentage of LNCaP cells was about 50%, which was identified

with the experiment result. As the electrodes were activated, *P* of LNCaP was increased to 80% in the single sorter, suggesting that most cells repelled to the side channel were prostate cancer cells. However, there were still 20% colorectal cancer cells that flowed into the side channel. Nevertheless, in the cascade sorter, the prostate cancer cells were separated again from the colorectal cancer cells near the electrode pair in the second main channel. Here, *P* of the LNCaP cells was increased to 96% by the cascade sorter. Compared with the single DEP sorter, *P* of the prostate cancer cells was increased by 20% in the cascade sorter. After all, since the LNCaP cells were repelled into the second side channel with a smaller volume of suspending medium, the concentration of cells was also increased from 1.5× 106 cells/ml to 4.5× 106 cells/ml. These results are very useful for the situation, where high purity and concentration of target cells is required. From Fig. 4.44, it is anticipated that with additional increase of the cascade number, *P* of the target cell can be further improved.

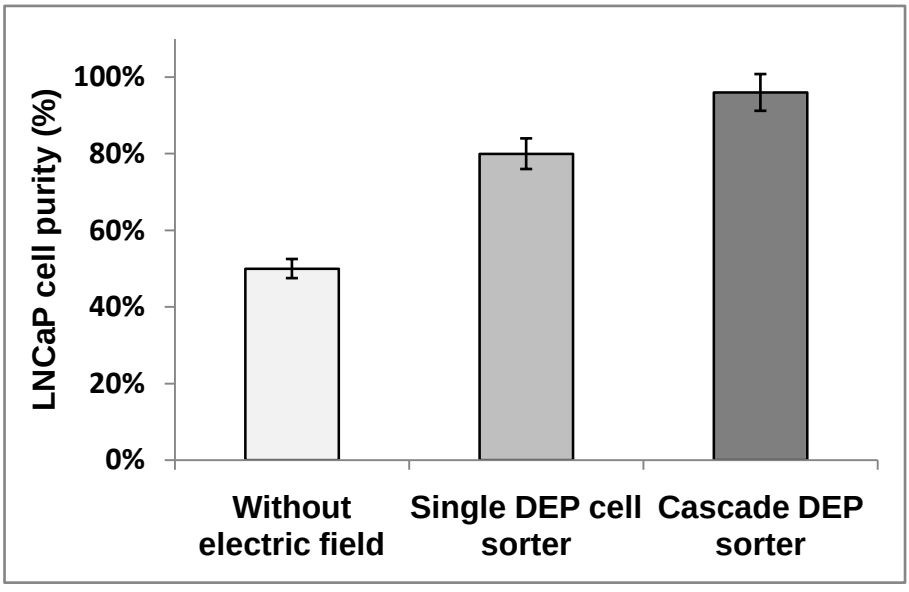

Figure 4.44 Quantitative comparison of LNCaP cell purity at the entrance of the side channel.

4.2.3.6 Cell separation in the staggered side channel DEP cell sorter

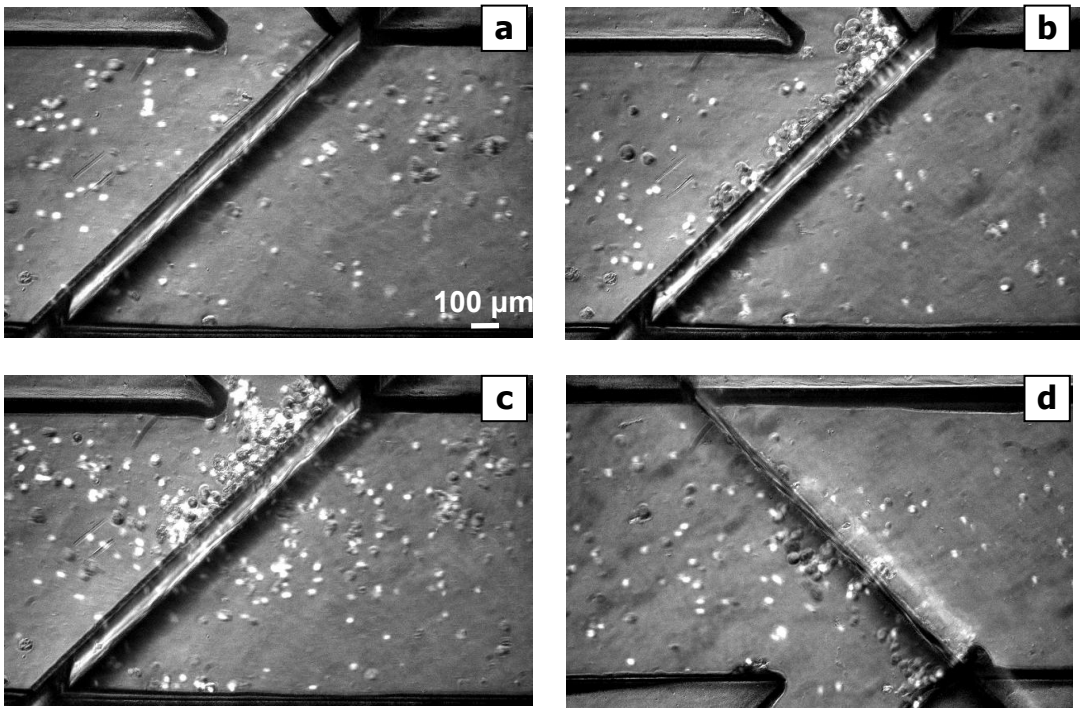

Figure 4.45 Visualization of separation between LNCaP and HCT116 cells in the staggered side channel sorter. (a) Without AC activation, both kinds of cells flowed through the electrode gap along the main channel. (b) At relatively low *Q* of 0.2 μL/min, with applied AC signals, almost all LNCaP cells were repelled to the first side channel due to the nDEP force. (c) When a relatively high *Q* of 0.4 μL/min was delivered, a small portion of LNCaP cells escaped to the main channel. (d) For the staggered DEP sorter, the escaped LNCaP cells were repelled by the second electrode pair, but the HCT116 cells remained flowing down to the end of the main channel.

To measure and quantify the throughput improvement in the staggered sorter, the applied voltage was kept at 12 Vp-p, and Q was changed from 0.1 μL/min to 1.6 μL/min. As shown in Fig. 4.45, the LNCaP cells were isolated from the HCT116 cells in the single side channel sorter after electrical activation at low Q, compared Fig. 45(a) to (b). Unfortunately, comparing Fig. 4.45(b) to (c), the number of target cells, which escaped from the first electrode pair, increased with the increased throughput. This effect will

reduces η. However, the design of the staggered side channel sorter, aiming at increasing the throughput without compromising η, can indeed overcome this problem as shown in Fig. 4.45(d).

We first measured η by increasing throughput in the single side channel sorter. As shown in Fig. 4.46, when Q was lower than 0.2 μL/min, η remained at 90%. As Q was increased from 0.2 μL/min, η started to decrease. Finally, when Q reached to 0.9 μL/min, η decreased to 20%, and the sorter then had no more effect for cell isolation.

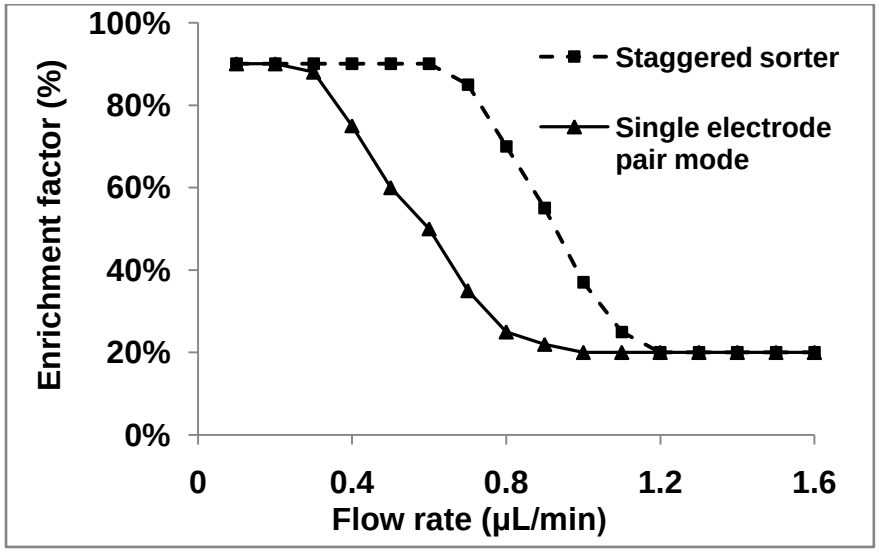

Figure 4.46 Enrichment factor as a function of sample flow rate.

We then measured η by increasing throughput in the staggered sorter. As also shown in Fig. 4.46, η remained at 90% as long as Q was lower than 0.6 μL/min. When Q reached to 1.2 μL/min, η decreased to 20%, and the sorter then had no more effect for cell isolation with further increasing of Q. For the single side channel sorter, to remain an enrichment factor of e.g. 90%, Q needed to be lower than 0.2 μL/min. Meanwhile, for the

staggered sorter, as long as Q was lower than 0.6 μL/min, the enrichment factor could be kept at 90%. Thus, in keeping the same η of 90%, Q was increased three times in the staggered sorter compared with that in the single side channel sorter. These results suggest that, without compromising η the sample throughput was successfully increased in the staggered sorter.

5. DISSCUSION

5.1 Mixing of equivalent conductivity

In the part of 4.1.4.6, we achieved fast mixing of two flows with equivalent conductivity. This is a very important result. Since the conductivity gradient is almost 0, in this case, according to equation 2.3, which lead to the charge density ρ_f close to 0. This means that, the electrical body force cannot be caused by net charge accumulated at the interface of the two streams. However, the mixing is still caused by the electrical force with no doubt, since the mixing started right after electric signal is applied. There are two mechanism of this mixing: firstly, electroosmosis. The top and bottom substrates of our micromixer are acrylic plastic, which are nonconductive. When liquid loaded into the channel, thin electric double layers (EDL) with zeta potential will be formed. The fluid was stretched and folded due to the transverse electroosmotic flow generated by applying an electric field on the electrodes. Consequently, mixing achieved even between two flows with no conductivity gradient. Song et al presented a numerical study of enhancing the mixing effect in microchannels via transverse electroosmotic flow in a similar mixer design.[225] Secondly, AC electric field might lead to non-uniform thermal distribution, which will cause a non-uniform charge distribution inside these two flows. Experimental measurement would be need for further investigation on this phenomenon.

5.2 Scalar turbulence measurement

Batchelor theory on small scalar structures has been perceived for more than five decades. However, so far, no reliable experiment in a laboratory can validate it, although some earlier pioneering measurements have supported the classical Batchelor theory, which predicts that beyond inertial-convective subrange, there is a viscous-convective subrange having a -1 slope in scalar power spectrum. In laboratory's experiments, Miller and Dimotakis (1996) found that their measured spectrum in jet did not follow the Batchelor's -1 slop; Williams et al (1997) measured the scalar spectrum in a magnetically forced two-dimensional turbulence with relatively low Reynolds number, and reported that the slope is steeper than -1. It seems that the debate if there is the -1 Batchelor spectrum beyond -5/3 spectrum, has not received its conclusion yet. Since Sc is about 2000, the Batchelor scale is about 40 times smaller than Kolmogorov scale. There should be a sufficient bandwidth of Batchelor spectrum that can be measured if it exists. Therefore, one may argue that either poor spatial resolution or low Re could be the reasons that the -1 spectrum cannot be observed experimentally.

As we know that Batchelor's theory is based on the assumption of isotropic flow (at least locally), therefore, isotropic flow should be achieved first in order to measure the Batchelor -1 spectrum. On the one hand, the -5/3 spectrum, whose appearance requires high Re and is usually an indication of isotropic flow, has already been observed in Fig. 4.11. We assume that, at least, local isotropic flows have been realized in Fig. 4.11(a). On the other hand, as Batchelor (1959) mentioned that the -1 spectrum does not require the Reynolds number of the turbulence to be so large that an

inertial subrange exists. Hence, the relatively low Re and anisotropic flow may not be the reason why there is no -1 Batchelor spectrum beyond the -5/3 spectrum.

5.3 Cascade and staggered DEP sorter

The purity and throughput can be further improved by adding more electrodes pairs and side channels into the DEP cell sorter. Moreover, multi parallel channels share the same inlet could also highly increase the throughput. Since each channel occupies a small area, the whole cell sorter chip could be still very small in size. And with only one inlet, a single injection of sample can result in different separation in each channel, which will highly improve the analysis efficiency, significantly reduce the sample wasting.

6. CONCLUSION

We firstly explore the effectiveness of manipulating electrokinetics to control/enhance fluid mixing inside a quasi T-microchannel with electrically conductive sidewalls in a diffuser configuration. With a small angle between the two sidewalls, there is the electric field not only in the transverse direction, but also in the streamwise direction. Compared with parallel sidewalls, the non-parallel sidewall can cause stronger mixing, if the angle between the sidewalls is small, e.g. about 5 ^{o}shown in this work, where the electric field in the transverse direction is not significantly reduced by the spreading of the channel. It is also found that the mixing can be enhanced under high conductivity gradient, low frequency, high voltage and 180 ^{o} signal phase shift between the two electrodes. Such a mixing process can also be achieved at high AC frequency to avoid bubble generation that often occurs at low AC frequency. Particle visualization indicates the spanwise vortex in the flow, and thus the motion in the transverse direction, which could be the cause of mixing enhancement in the presented micromixer. Furthermore, the turbulent flow is also measured with laser induced fluorescence (LIF) for scalar investigation and laser induced fluorescence photobleaching anemometer (LIFPA) for velocity measurement. Results indicated that for the first time turbulence can be achieved under AC electrokinetic forcing at low Reynolds number in the order of 1 in this novel design. Thus, turbulent mixing can also be generated in microfluidics to cause rapid mixing. Moreover, to further

investigate turbulence in microfluidics, scalar measurement with LIF system will also be done in future works.

Secondly, we successfully manipulated and isolated HCT116 colorectal cancer cell from HEK293 kidney cell and E-coli bacteria based on cell dielectric property, e.g. permittivity, conductivity and size, by a microfluidic cell sorter based on conventional negative dielectrophoresis. After that, LNCaP prostate cancer cells were also isolated from the mixture with HCT116 colorectal cancer cells. DEP spectra of the prostate cancer cell and the colorectal cancer cell were measured in media with different conductivity. Effect of parameters such as flow rate and applied voltage has been investigated as well. The present work indicated that a given cell may have a specific dielectric property that is different from that of other cells. Such a difference may be leveraged for DEP separation. These results give a new opportunity for clinic diagnosis of prostate cancer for circulating tumor cell using a lab-on-a-chip device. Furthermore, we developed a cascade configuration sorter to increase purity of the isolated target cells, and a staggered sorter with two side channels in opposite side walls to increase sample throughput without compromising enrichment factor. Carboxylate particles have been first separated in both sorters based on their difference in sizes. Then we have successfully isolated the prostate cancer cells LNCaP from the colorectal cancer cells HCT116 by optimizing electric properties in these cell sorters. *P* of isolated cells was increased by 20% through adding only one more sorter in the cascade configuration. Sample throughput was increased to three times in the staggered side channel DEP sorter compared with that of a single DEP sorter without compromising the enrichment factor. The present work indicates that, not only biological cells can be separated and isolated from each other by DEP, but also *P* of

the isolated target cells and sample throughput could be increased by the designed cascade and staggered DEP sorter. This would provide new opportunities to enhance DEP sorter performance for lab-on-a-chip applications. In future works, isolate circulating tumor cells from real blood will be test in our cell sorters, which is very important to practical applications in medical diagnostics.

REFERENCES

1. Terry, S.C., J.H. Jerman, and J.B. Angell, *A gas chromatographic air analyzer fabricated on a silicon wafer*. Electron Devices, IEEE Transactions on, 1979. **26**(12): p. 1880-1886.

2. Kirby, B.J., *Micro- and Nanoscale Fluid Mechanics: Transport in Microfluidic Devices*2010: Cambridge University Press.

3. Karniadakis, G.M., Beskok, A., Aluru, N, *Microflows and Nanoflows*2005: Springer Verlag.

4. Tabeling, P., *Introduction to Microfluidics*2010: OUP Oxford.

5. Oosterbroek, E. and A.v.d. Berg, *Lab-on-a-Chip: Miniaturized systems for (bio)chemical analysis and synthesis, Elsevier Science*. 2nd ed2003.

6. Geschke, O., H. Klank, and P. Telleman, *Microsystem Engineering of Lab-on-a-chip Devices*. 1 ed2004.

7. Sanders, G.H.W. and A. Manz, *Chip-based microsystems for genomic and proteomic analysis.* TrAC Trends in Analytical Chemistry, 2000. **19**(6): p. 364-378.

8. Auroux, P.-A., et al., *Micro Total Analysis Systems. 2. Analytical Standard Operations and Applications.* Analytical Chemistry, 2002. **74**(12): p. 2637-2652.

9. Bousse, L., et al., *ELECTROKINETICALLY CONTROLLED MICROFLUIDIC ANALYSIS SYSTEMS.* Annual Review of Biophysics and Biomolecular Structure, 2000. **29**(1): p. 155 - 181.

10. Jacobson, S.C. and J.M. Ramsey, *Electrokinetic Focusing in Microfabricated Channel Structures.* Analytical Chemistry, 1997. **69**(16): p. 3212-3217.

11. Wen, J., et al., *Microfluidic-Based DNA Purification in a Two-Stage, Dual-Phase Microchip Containing a Reversed-Phase and a Photopolymerized Monolith.* Analytical Chemistry, 2007. **79**(16): p. 6135-6142.

12. Oddy, M.H., J.G. Santiago, and J.C. Mikkelsen, *Electrokinetic Instability Micromixing.* Anal. Chem., 2001. **73**: p. 5822–5832.

13. Shin, S.M., I.S. Kang, and Y.-K. Cho, *Mixing enhancement by using electrokinetic instability under time-periodic electric field.* J Micromech Microeng, 2005. **15**: p. 455–462.

14. El Moctar, A.O., N. Aubry, and J. Batton, *Electro–hydrodynamic micro-fluidic mixer.* Lab on a Chip, 2003. **3**: p. 273-280.

15. Dreher, S., N. Kockmann, and P. Woias, *Characterization of Laminar Transient Flow Regimes and Mixing in T-shaped Micromixers.* Heat Transfer Engineering, 2009. **30**(1): p. 91 - 100.

16. Wu, Z. and D. Li, *Micromixing using induced-charge electrokinetic flow.* Electrochimica Acta, 2008. **53**(19): p. 5827-5835.

17. Singh, M., et al., *The mapping method as a toolbox to analyze, design, and optimize micromixers.* Microfluidics and Nanofluidics, 2008. **5**(3): p. 313-325.

18. Nam-Trung, N. and W. Zhigang, *Micromixers review.* Journal of Micromechanics and Microengineering, 2005. **15**(2): p. R1.

19. Nguyen, N.-T. and Z. Wu, *Micromixers - a review.* Journal of Micromechanics and Microengineering, 2005. **15**(2): p. R1- R16.

20. Hessel, V., H. Loe, and F. Schofeld, *Micromixers--a review on passive and active mixing principles.* Chemical Engineering Science, 2005. **60**(8-9): p. 2479-2501.

21. Yang, Z., et al., *Ultrasonic micromixer for microfluidic systems.* Sensors and Actuators A: Physical, 2001. **93**(3): p. 266-272.

22. Bockhorn, H., et al., *Theoretical and Experimental Investigations of Convective Micromixers and Microreactors for Chemical Reactions*, in *Micro and Macro Mixing*, D. Mewes and F. Mayinger, Editors. 2010, Springer Berlin Heidelberg. p. 325-346.

23. Gradl, J. and W. Peukert, *Characterization of Micro Mixing for Precipitation of Nanoparticles in a T-Mixer*, in *Micro and Macro Mixing*, D. Mewes and F. Mayinger, Editors. 2010, Springer Berlin Heidelberg. p. 105-124.

24. Chen, C.-H., et al., *Convective and absolute electrokinetic instability with conductivity gradients.* Journal of Fluid Mechanics, 2005. **524**(-1): p. 263-303.

25. Wang, S.-C., et al., *Dynamic superconcentration at critical-point double-layer gates of conducting nanoporous granules due to asymmetric tangential fluxes.* Biomicrofluidics, 2008. **2**(1): p. 014102-9.

26. Wang, S.-C., et al., *AC electro-osmotic mixing induced by non-contact external electrodes.* Biosensors and Bioelectronics, 2006. **22**(4): p. 563-567.

27. Wang, S.-C., et al., *Microfluidic Mixing by dc and ac Nonlinear Electrokinetic Vortex Flows.* Industrial & Engineering Chemistry Research, 2004. **43**(12): p. 2902-2911.

28. Yossifon, G. and H.-C. Chang, *Selection of Nonequilibrium Overlimiting Currents: Universal Depletion Layer Formation Dynamics and Vortex Instability.* Physical Review Letters, 2008. **101**(25): p. 254501.

29. Nguyen, N.T. and Z. Wu, *Micromixers – a review.* Journal of Micromechnics and Microengineering, 2005. **15**: p. r1-r16.

30. Chang, C.-C. and R.-J. Yang, *Electrokinetic mixing in microfluidic systems.* Microfluidics and Nanofluidics, 2007. **3**(5): p. 501-525.

31. Kamholz, A.E., et al., *Quantitative Analysis of Molecular Interaction in a Microfluidic Channel: The T-Sensor.* Analytical Chemistry, 1999. **71**(23): p. 5340-5347.

32. Ismagilov, R.F., et al., *Experimental and theoretical scaling laws for transverse diffusive broadening in two-phase laminar flows in microchannels.* Applied Physics Letters, 2000. **76**(17): p. 2376-2378.

33. Stroock, A.D., et al., *Chaotic Mixer for Microchannels.* Science, 2002. **295**(5555): p. 647-651.

34. Stroock, A.D., et al., *Erratum: Patterning Electro-osmotic Flow with Patterned Surface Charge [Phys. Rev. Lett. 84, 3314 (2000)]*. Physical Review Letters, 2001. **86**(26): p. 6050-6050.

35. Erickson, D. and D. Li, *Influence of Surface Heterogeneity on Electrokinetically Driven Microfluidic Mixing.* Langmuir, 2002. **18**(5): p. 1883-1892.

36. Oddy, M.H., J.G. Santiago, and J.C. Mikkelsen, *Electrokinetic Instability Micromixing.* Analytical Chemistry, 2001. **73**(24): p. 5822-5832.

37. Lin, H., et al., *Instability of electrokinetic microchannel flows with conductivity gradients*, in *Physics of Fluids*2004, American Institute of Physics. p. 1922-1935.

38. Mao, H., T. Yang, and S.P. Cremer, *A microfluidic device with a linear temperature gradient for parallel and combinatorial measurements.* J. Am. Chem. Soc., 2002. **124**(16): p. 4432–4435.

39. Deshmukh, A.A., D. Liepmann, and A.P. Pisano. *Characterization of a micro-mixing, pumping, and valving system, Proc*. in *Transducers'01, 11th Int. Conf. on Solid-State Sensors and Actuators*. 2001. Munich, Germany.

40. Glasgow, I. and N. Aubry, *Enhancement of microfluidic mixing using time pulsing.* Lab on a Chip, 2003. **3**: p. 114-120.

41. Deval, J., P. Tabeling, and C.M. Ho. *A dielectrophoretic chaotic mixer, Proc.* in *MEMS'02, 15th IEEE Int. Workshop Micro Electromechanical System*. 2000. Las Vegas, Nevada.

42. Bau, H.H., J. Zhong, and M. Yi, *A minute magneto hydrodynamic (MHD).* mixer Sensors Actuators B, 2001. **79**: p. 207–15.

43. Liu, R.H., et al., *Bubble-induced acoustic micromixing.* Lab on a Chip, 2002. **2**: p. 151-157.

44. Joanne, D., T. Patrick, and H. Chih-Ming, *A DIELECTROPHORETIC CHAOTIC MIXER*, in *Micro Electro Mechanical Systems, 2002. The Fifteenth IEEE International Conference on*2002: Las Vegas, NV, USA. p. 36-39.

45. Dodge, A., et al., *Spatiotemporal resonances in a microfluidic system.* Physical Review E, 2005. **72**(5): p. 056312.

46. Biddiss, E., D. Erickson, and D. Li, *Heterogeneous Surface Charge Enhanced Micromixing for Electrokinetic Flows.* Analytical Chemistry, 2004. **76**(11): p. 3208-3213.

47. Coleman, J.T., J. McKechnie, and D. Sinton, *High-efficiency electrokinetic micromixing through symmetric sequential injection and expansion.* Lab on a Chip, 2006. **6**(8): p. 1033-1039.

48. Feng, J.J., S. Krishnamoorthy, and S. Sundaram, *Numerical analysis of mixing by electrothermal induced flow in microfluidic systems.* Biomicrofluidics, 2007. **1**(2): p. 024102-8.

49. Moctar, A.O.E., N. Aubry, and J. Batton, *Electro-hydrodynamic micro-fluidic mixer.* Lab on a Chip, 2003. **3**(4): p. 273-280.

50. Ramos, A., et al., *Ac electrokinetics: a review of forces in microelectrode structures.* Journal of Physics D: Applied Physics, 1998. **31**(18): p. 2338-2353.

51. Griffiths, S.K. and R.H. Nilson, *Band Spreading in Two-Dimensional Microchannel Turns for Electrokinetic Species Transport.* Analytical Chemistry, 2000. **72**(21): p. 5473-5482.

52. Groisman, A. and V. Steinberg, *Elastic turbulence in a polymer solution flow.* Nature, 2000. **405**(6782): p. 53-55.

53. Janasek, D., J. Franzke, and A. Manz, *Scaling and the design of miniaturized chemical-analysis systems.* Nature, 2006. **442**(7101): p. 374-380.

54. Ahn, Y.-C., W. Jung, and Z. Chen, *Optical sectioning for microfluidics: secondary flow and mixing in a meandering microchannel.* Lab on a Chip, 2008. **8**(1): p. 125-133.

55. Capretto, L., et al., *Micromixing Within Microfluidic Devices.* Topics in Current Chemistry 2011. **304**: p. 42.

56. Tennekes, H. and J.L. Lumley, *A First Course in Turbulence*1972: The MIT press.

57. Kirby, B., *Micro - and Nanoscale Fluid Mechanics: Transport in Microfluidic Devices*2010: Cambridge University Press.

58. Sharp, K.V., et al., *Liquid Flows in Microchannels*, in *The Mems Handbook*, M. Gad-el-Hak, Editor 2002, CRC Press.

59. Wang, G.R., *On Large Structures and Turbulent Mixing in Confined Mixing Layers under Forcing.* AIChE Journal, 2006. **52**(1): p. 14.

60. Wang, G.R., *Realizing Statistical Features of High Reynolds Number Turbulence at Relatively Low Reynolds Number Flow.* Submitted Journal of Fluid Mechanics, 2013.

61. Groisman, A. and V. Steinberg, *Efficient mixing at low Reynolds numbers using polymer additives.* Nature, 2001. **410**: p. 905-908.

62. Shraiman, B.I. and E.D. Siggia, *Scalar turbulence.* Nature, 2000. **405**: p. 8.

63. Warhaft, Z., *Passive scalars in turbulent flows.* Annu. Rev. Fluid Mech., 2000. **32**: p. 38.

64. Antonia, R.A. and P. Orlandi, *On the Batchelor constant in decaying isotropic turbulence.* Phys. Fluids, 2003 **15**: p. 2084-2086.

65. Duplat, J., C. Innocenti, and E. Villermaux, *A nonsequential turbulent mixing process.* Physics of Fluids, 2010. **22**(3): p. 035104.

66. Donzis, D., K. Sreenivasan, and P. Yeung, *The Batchelor Spectrum for Mixing of Passive Scalars in Isotropic Turbulence.* Flow, Turbulence and Combustion, 2010. **85**(3): p. 549-566.

67. Yeung, P.K. and K.R. Sreenivasan, *Spectrum of passive scalars of high molecular diffusivity in turbulent mixing.* Journal of Fluid Mechanics. **716**: p. null-null.

68. Kolmogorov, A., *The local structure of turbulence in incompressible viscous fluid for very large Reynolds number.* Dokl. Akad. Nauk SSSR 1941. **30**: p. 9-13.

69. Obukhov, A.M., *Structure of the temperature field in a turbulent flow.* Izv. Akad. Nauk SSSR, Ser. Geogr. Geofiz., 1949. **13**: p. 58

70. Corrsin, S., *On the spectrum of isotropic temperature fluctuations in an isotropic turbulence.* J. Appl. Phys., 1951. **22**: p. 469

71. Frisch, U., *Turbulence—The legacy of A. N. Kolmogorov*1995: Cambridge University Press.

72. Batchelor, G.K., *Small-scale variation of convected quantities like temperature in a turbulent fluid. I. General discussion and the case of small conductivity.* J. Fluid Mech., 1959. **5**: p. 113

73. Gibson, C.H. and W.H. Schwarz, *The universal equilibrium spectra of turbulent velocity and scalar fields.* J. Fluid Mech., 1963. **16**: p. 365-384.

74. Nye, J.O. and R.S. Brodkey, *The scalar spectrum in the viscous-convective subrange.* J. Fluid Mech. , 1967. **29**: p. 151-163.

75. Grant, H.L., et al., *The spectrum of temperature fluctuations in turbulent flow.* Journal of Fluid Mechanics, 1968. **34**(03): p. 423-442.

76. Wu, X.l., et al., *Hydrodynamic Convection in a Two-Dimensional Couette Cell.* Physical Review Letters, 1995. **75**(2): p. 236-239.

77. Kraichnan, R.H., *Small-scale structure of a scalar field convected by turbulence.* Phys. Fluids, 1968. **11**: p. 945.

78. Holzer, M. and E.D. Siggia, *Turbulent mixing of a passive scalar.* Phys. Fluids 1994. **6**: p. 1820-1837.

79. Bogucki, D., A. Domaradzki, and P.K. Yeung, *Direct numerical simulations of passive scalars with Pr>1 advected by turbulent flow.* Journal of Fluid Mechanics, 1997. **343**: p. 111-130.

80. Chasnov, J.R., *The viscous-convective subrange in nonstationary turbulence.* Physics of Fluids, 1998. **10**(5): p. 1191-1205.

81. Miller, P. and P. Dimotakis, *Measurements of scalar power spectra in high Schmidt number turbulent jets.* J. Fluid Mech., 1996. **308**: p. 129-46.

82. Williams, B., D. Marteau, and J. Gollub, *Mixing of passive scalar in magnetically forced two-dimensional turbulence.* Phys. Fluids, 1997. **9**: p. 2061-80.

83. Antonia, R.A., et al., *Temperature structure functions in turbulent shear flows.* Phys. Rev. A 1984. **30**: p. 2704.

84. Lesieur, M. and R. Rogallo, *Large eddy simulation of passive scalar diffusion in isotropic turbulence.* Phys. Fluids A, 1989. **1**: p. 718-22.

85. Chen, S. and N. Cao, *Anomalous scaling and structure instability in three dimensional passive scalar turbulence.* Phys. Rev. Lett., 1997. **78**: p. 3459

86. Hof, B., et al., *Turbulence regeneration at moderate Reynolds numbers.* Phys. Rev. Lett., 2005. **95**: p. 214502.

87. Wang, G.R., *A rapid mixing process in continuous operation under periodic forcing.* Chem. Eng. Sci., 2003. **58**: p. 11.

88. Wang, G.R., *Turbulent Mixing, Stability and Secondary Flow in a Confined Configuration*2000, Berlin: Verlag Dr. Ko ̈ster, ISBN: 3-89574-376-3**,** Bd. 8

89. Wang, G., F. Yang, and W. Zhao, *Can a flow be turbulent in microfluidics with Reynolds number in the order of 1?,* in *65th Annual Meeting of the APS Division of Fluid Dynamics*2012: November 18-20, San Diego, California.

90. Wang, G., F. Yang, and W. Zhao, *There can be turbulence in microfluidics with Reynolds in the order of 1*. 2013. **Submitted**.

91. Yang, F., W. Zhao, and G. Wang, *Turbulent mixing in microfluidics with Reynolds number in the order of 1*, in *65th Annual Meeting of the APS Division of Fluid Dynamics*2012: November 18-20, San Diego, California.

92. Wang, G., W. Zhao, and F. Yang, *Scalar features of turbulent mixing in microfluidics with low Reynolds number.* 2013. **in preparation**.

93. Cheng, I.F., et al., *An integrated dielectrophoretic chip for continuous bioparticle filtering, focusing, sorting, trapping, and detecting.* Biomicrofluidics, 2007. **1**(2): p. 021503-15.

94. Fergenson, D.P., et al., *Reagentless Detection and Classification of Individual Bioaerosol Particles in Seconds.* Analytical Chemistry, 2003. **76**(2): p. 373-378.

95. Chang, H.-C. and G. Yossifon, *Understanding electrokinetics at the nanoscale: A perspective.* Biomicrofluidics, 2009. **3**(1): p. 012001-15.

96. Gordon, J.E., Z. Gagnon, and H.-C. Chang, *Dielectrophoretic discrimination of bovine red blood cell starvation age by buffer selection and membrane cross-linking.* Biomicrofluidics, 2007. **1**(4): p. 044102-5.

97. Senapati, S., et al., *Rapid on-chip genetic detection microfluidic platform for real world applications.* Biomicrofluidics, 2009. **3**(2): p. 022407-7.

98. Susmel, S., G.G. Guilbault, and C.K. O'Sullivan, *Demonstration of labeless detection of food pathogens using electrochemical redox probe and screen printed gold electrodes.* Biosensors and Bioelectronics, 2003. **18**(7): p. 881-889.

99. Daniel Figeys, *Adapting arrays and lab-on-a-chip technology for proteomics.* Proteomics, 2002. **2**(4): p. 373-382.

100. Sato, K., et al., *Determination of Carcinoembryonic Antigen in Human Sera by Integrated Bead-Bed Immunoasay in a Microchip for Cancer Diagnosis.* Analytical Chemistry, 2001. **73**(6): p. 1213-1218.

101. Easley, C.J., et al., *A fully integrated microfluidic genetic analysis system with sample-in-answer-out capability.* Proceedings of the National Academy of Sciences, 2006. **103**(51): p. 19272-19277.

102. Fulwyler, M.J., *Electronic Separation of Biological Cells by Volume.* Science, 1965. **150**(3698): p. 910-911.

103. M, D.W. and G.W. H, *Flow-through chamber for photometers to measure and count particles in a dispersion medium*, 1971: United States.

104. Miltenyi, S., et al., *High gradient magnetic cell separation with MACS.* Cytometry, 1990. **11**(2): p. 231-238.

105. McCloskey, K.E., J.J. Chalmers, and M. Zborowski, *Magnetic Cell Separation: Characterization of Magnetophoretic Mobility.* Analytical Chemistry, 2003. **75**(24): p. 6868-6874.

106. Guck, J., et al., *Optical Deformability as an Inherent Cell Marker for Testing Malignant Transformation and Metastatic Competence.* Biophysical journal, 2005. **88**(5): p. 3689-3698.

107. Evander, M., et al., *Noninvasive Acoustic Cell Trapping in a Microfluidic Perfusion System for Online Bioassays.* Analytical Chemistry, 2007. **79**(7): p. 2984-2991.

108. Huang, L.R., et al., *Continuous Particle Separation Through Deterministic Lateral Displacement.* Science, 2004. **304**(5673): p. 987-990.

109. Yamada, M., M. Nakashima, and M. Seki, *Pinched Flow Fractionation: Continuous Size Separation of Particles Utilizing a Laminar Flow Profile in a Pinched Microchannel.* Analytical Chemistry, 2004. **76**(18): p. 5465-5471.

110. Nagrath, S., et al., *Isolation of rare circulating tumour cells in cancer patients by microchip technology.* Nature, 2007. **450**(7173): p. 1235-1239.

111. Jäggi, R., R. Sandoz, and C. Effenhauser, *Microfluidic depletion of red blood cells from whole blood in high-aspect-ratio microchannels.* Microfluidics and Nanofluidics, 2007. **3**(1): p. 47-53.

112. Fiedler, S., et al., *Dielectrophoretic Sorting of Particles and Cells in a Microsystem.* Analytical Chemistry, 1998. **70**(9): p. 1909-1915.

113. Jones, T.B., *Electromechanics of Particles*1995: Cambridge University Press.

114. Pethig, R. and D.B. Kell, *The passive electrical properties of biological systems: their significance in physiology, biophysics and biotechnology.* Physics in Medicine and Biology, 1987(8): p. 933.

115. Sukhorukov, V., W. Arnold, and U. Zimmermann, *Hypotonically induced changes in the plasma membrane of cultured mammalian cells.* Journal of Membrane Biology, 1993. **132**(1): p. 27-40.

116. Gawad, S., Schild, L., Renaud, P. H., *Micromachined Impedance Spettroscopy Flow Cytometer for Cell Analysis and Particle Sizing.* Lab on a Chip, 2001. **1**: p. 76-82.

117. Talary, M., et al., *Dielectrophoretic separation and enrichment of CD34+cell subpopulation from bone marrow and peripheral blood stem cells.* Medical and Biological Engineering and Computing, 1995. **33**(2): p. 235-237.

118. Kua, C.H., et al., *Cell Motion Model for Moving Dielectrophoresis.* Analytical Chemistry, 2008. **80**(14): p. 5454-5461.

119. Pethig, R. and G.H. Markx, *Applications of dielectrophoresis in biotechnology.* Trends in Biotechnology, 1997. **15**(10): p. 426-432.

120. Markx, G.H., P.A. Dyda, and R. Pethig, *Dielectrophoretic separation of bacteria using a conductivity gradient.* Journal of Biotechnology, 1996. **51**(2): p. 175-180.

121. Michael P. Hughes, *Strategies for dielectrophoretic separation in laboratory-on-a-chip systems.* Electrophoresis, 2002. **23**(16): p. 2569-2582.

122. Thomas Schnelle, et al., *Dielectrophoretic manipulation of suspended submicron particles.* Electrophoresis, 2000. **21**(1): p. 66-73.

123. Schnelle, T., et al., *Single micro electrode dielectrophoretic tweezers for manipulation of suspended cells and particles.* Biochimica et Biophysica Acta (BBA) - General Subjects, 1999. **1428**(1): p. 99-105.

124. Hughes, M.P., et al., *Manipulation of herpes simplex virus type 1 by dielectrophoresis.* Biochimica et Biophysica Acta (BBA) - General Subjects, 1998. **1425**(1): p. 119-126.

125. Crane, J.S. and H.A. Pohl, *A Study of Living and Dead Yeast Cells Using Dielectrophoresis.* Journal of The Electrochemical Society, 1968. **115**(6): p. 584-586.

126. John Kadaksham, Pushpendra Singh, and Nadine Aubry, *Dielectrophoresis induced clustering regimes of viable yeast cells.* Electrophoresis, 2005. **26**(19): p. 3738-3744.

127. Becker, F.F., et al., *Separation of human breast cancer cells from blood by differential dielectric affinity.* Proceedings of the National Academy of Sciences of the United States of America, 1995. **92**(3): p. 860-864.

128. Huang, Y., et al., *The Removal of Human Breast Cancer Cells from Hematopoietic CD34+ Stem Cells by Dielectrophoretic Field-Flow-Fractionation.* Journal of Hematotherapy & Stem Cell Research, 1999. **8**(5): p. 481-490.

129. Dang, F., et al., *Characterization of Electrophoretic Behavior of Sugar Isomers by Microchip Electrophoresis Coupled with Videomicroscopy.* Analytical Chemistry, 2003. **75**(10): p. 2433-2439.

130. Shultz-Lockyear, L.L., et al., *Effects of injector geometry and sample matrix on injection and sample loading in integrated capillary electrophoresis devices.* Electrophoresis, 1999. **20**(3): p. 529-538.

131. Hoburg, J.F. and J.R. Melcher, *Internal electrohydrodynamic instability and mixing of fluids with orthogonal field and conductivity gradients.* Journal of Fluid Mechanics, 1976. **73**(02): p. 333-351.

132. Hoburg, J.F. and J.R. Melcher, *Electrohydrodynamic mixing and instability induced by co-linear fields and conductivity gradients.* Physics of Fluids, 1977. **20**(6): p. 903-911.

133. Baygents, J.C. and F. Baldessari, *Electrohydrodynamic instability in a thin fluid layer with an electrical conductivity gradient.* Physics of Fluids, 1998. **10**(1): p. 301.

134. Storey, B.D., et al., *Electrokinetic instabilities in thin microchannels.* Physics of Fluids, 2005. **17**(1): p. 018103-4.

135. POSNER, J.D. and J.G. SANTIAGO, *Convective instability of electrokinetic flows in a cross-shaped microchannel.* Journal of Fluid Mechanics, 2006. **555**: p. 1-42.

136. Oddy, M.H. and J.G. Santiago, *Multiple-species model for electrokinetic instability.* Physics of Fluids, 2005. **17**(6): p. 064108-17.

137. Huang, M.-Z., et al., *Application of electrokinetic instability flow for enhanced micromixing in cross-shaped microchannel.* Biomedical Microdevices, 2006. **8**(4): p. 309-315.

138. Pan, Y.-J., C.-M. Ren, and R.-J. Yang, *Electrokinetic flow focusing and valveless switching integrated with electrokinetic instability for mixing enhancement.* Journal of Micromechanics and Microengineering, 2007. **17**(4): p. 820.

139. Tai, C.-H., et al., *Micromixer utilizing electrokinetic instability-induced shedding effect.* Electrophoresis, 2006. **27**(24): p. 4982-4990.

140. Melcher, J.R. and G.I. Taylor, *Electrohydrodynamics: A Review of the Role of Interfacial Shear Stresses.* Annual Review of Fluid Mechanics, 1969. **1**(1): p. 111-146.

141. LI, F., et al., *Linear stability of a two-fluid interface for electrohydrodynamic mixing in a channel.* Journal of Fluid Mechanics, 2007. **583**: p. 347-377.

142. Ozen, O., et al., *Electrohydrodynamic linear stability of two immiscible fluids in channel flow*. Electrochimica Acta, 2006. **51**(25): p. 5316-5323.

143. Zahn, J. and V. Reddy, *Two phase micromixing and analysis using electrohydrodynamic instabilities.* Microfluidics and Nanofluidics, 2006. **2**(5): p. 399-415.

144. Sundaram, N. and D.K. Tafti, *Evaluation of Microchamber Geometries and Surface Conditions for Electrokinetic Driven Mixing.* Analytical Chemistry, 2004. **76**(13): p. 3785-3793.

145. Pethig, R. and D.B. Kell, *The passive electrical properties of biological systems: their significance in physiology, biophysics and biotechnology.* Physics in Medicine and Biology, 1987. **32**(8): p. 933-970.

146. Khoshmanesh, K., et al., *Dielectrophoretically patterned carbon nanotubes to sort microparticles.* Electrophoresis, 2010. **31**(20): p. 3380-3390.

147. Khoshmanesh, K., et al., *Particle trapping using dielectrophoretically patterned carbon nanotubes.* Electrophoresis, 2010. **31**(8): p. 1366-1375.

148. White, C.M., L.A. Holland, and P. Famouri, *Application of capillary electrophoresis to predict crossover frequency of polystyrene particles in dielectrophoresis.* Electrophoresis, 2010. **31**(15): p. 2664-2671.

149. Kang, Y., et al., *DC-Dielectrophoretic separation of biological cells by size.* Biomedical Microdevices, 2008. **10**(2): p. 243-249.

150. Pethig, R., *Review Article---Dielectrophoresis: Status of the theory, technology, and applications.* Biomicrofluidics, 2010. **4**(2): p. 022811-35.

151. Gascoyne, P.R.C., et al., *Dielectrophoretic separation of mammalian cells studied by computerized image analysis.* Measurement Science and Technology, 1992(5): p. 439-445.

152. Çetin, B. and D. Li, *Lab-on-a-chip device for continuous particle and cell separation based on electrical properties via alternating current dielectrophoresis.* Electrophoresis, 2010. **31**(18): p. 3035-3043.

153. Shafiee, H., et al., *Contactless dielectrophoresis: a new technique for cell manipulation.* Biomedical Microdevices, 2009. **11**(5): p. 997-1006.

154. Dharmasiri, U., et al., *Microsystems for the Capture of Low-Abundance Cells.* Annual Review of Analytical Chemistry, 2010. **3**(1): p. 409-431.

155. Park, J., et al., *Single cell trapping in larger microwells capable of supporting cell spreading and proliferation.* Microfluidics and Nanofluidics, 2010. **8**(2): p. 263-268.

156. Pratt, E.D., et al., *Rare cell capture in microfluidic devices.* Chemical Engineering Science, 2011. **66**(7): p. 1508-1522.

157. Nakamura, R.M., et al., *Cancer Diagnostics Current and Future Trends*2004: Humana Press.

158. Jemal, A., et al., *Cancer Statistics, 2008.* CA Cancer J Clin, 2008: p. CA.2007.0010.

159. Jemal, A., et al., *Cancer Statistics, 2009.* CA: A Cancer Journal for Clinicians, 2009. **59**(4): p. 225-249.

160. Sardana, G., B. Dowell, and E.P. Diamandis, *Emerging Biomarkers for the Diagnosis and Prognosis of Prostate Cancer.* Clinical Chemistry, 2008. **54**(12): p. 1951-1960.

161. Schröder, F.H., et al., *Evaluation of the Digital Rectal Examination as a Screening Test for Prostate Cancer.* Journal of the National Cancer Institute, 1998. **90**(23): p. 1817-1823.

162. Legler, J.M., et al., *The role of prostate-specific antigen (PSA) testing patterns in the recent prostate cancer incidence declinein the United States.* Cancer Causes and Control, 1998. **9**(5): p. 519-527.

163. Etzioni, R., et al., *Overdiagnosis Due to Prostate-Specific Antigen Screening: Lessons From U.S. Prostate Cancer Incidence Trends.* Journal of the National Cancer Institute, 2002. **94**(13): p. 981-990.

164. Zieglschmid, V., C. Hollmann, and O. Böcher, *DETECTION OF DISSEMINATED TUMOR CELLS IN PERIPHERAL BLOOD.* Critical Reviews in Clinical Laboratory Sciences, 2005. **42**(2): p. 155-196.

165. Miller, M.C., G.V. Doyle, and L.W.M.M. Terstappen, *Significance of Circulating Tumor Cells Detected by the CellSearch System in Patients withMetastaticBreast Colorectal and Prostate Cancer.* Journal of Oncology, 2010. **2010**: p. 1-8.

166. Rhim, A.D., et al., *EMT and Dissemination Precede Pancreatic Tumor Formation.* Cell, 2012. **148**(1-2): p. 349-61.

167. Sieben, S., et al., *Comparison of different particles and methods for magnetic isolation of circulating tumor cells.* Journal of Magnetism and Magnetic Materials, 2001. **225**(1-2): p. 175-179.

168. Stott, S.L., et al., *Isolation and Characterization of Circulating Tumor Cells from Patients with Localized and Metastatic Prostate Cancer.* Science Translational Medicine, 2010. **2**(25): p. 25ra23.

169. Pratt, E.D., et al., *Rare cell capture in microfluidic devices.* Chemical Engineering Science, 2010. **In Press, Corrected Proof**.

170. Ellis, W.J., et al., *Detection and isolation of prostate cancer cells from peripheral blood and bone marrow.* Urology, 2003. **61**(2): p. 277-281.

171. Gleghorn, J.P., et al., *Capture of circulating tumor cells from whole blood of prostate cancer patients using geometrically enhanced differential immunocapture (GEDI) and a prostate-specific antibody.* Lab on a Chip, 2009. **10**(1): p. 27-29.

172. Dharmasiri, U., et al., *Highly efficient capture and enumeration of low abundance prostate cancer cells using prostate-specific membrane antigen aptamers immobilized to a polymeric microfluidic device.* Electrophoresis, 2009. **30**(18): p. 3289-3300.

173. Zheng, S., et al., *Membrane microfilter device for selective capture, electrolysis and genomic analysis of human circulating tumor cells.* Journal of Chromatography A, 2007. **1162**(2): p. 154-161.

174. Tuchin, V.V., *A Clear Vision for Laser Diagnostics (Review).* Selected Topics in Quantum Electronics, IEEE Journal of, 2007. **13**(6): p. 1621-1628.

175. Thomas Ryll, et al., *Performance of small-scale CHO perfusion cultures using an acoustic cell filtration device for cell retention: Characterization of separation efficiency and impact of perfusion on product quality.* Biotechnology and Bioengineering, 2000. **69**(4): p. 440-449.

176. Doh, I. and Y.-H. Cho, *A continuous cell separation chip using hydrodynamic dielectrophoresis (DEP) process.* Sensors and Actuators A: Physical, 2005. **121**(1): p. 59-65.

177. Gambari, R., et al., *Applications to Cancer Research of "Lab-on-a-chip" Devices Based on Dielectrophoresis (DEP).* Technology in Cancer Research and Treatment, 2003. **2**: p. 31-40.

178. Gascoyne, P.R.C., et al., *Isolation of rare cells from cell mixtures by dielectrophoresis.* Electrophoresis, 2009. **30**(8): p. 1388-1398.

179. Wu, Z. and et al., *Microfluidic continuous particle/cell separation via electroosmotic-flow-tuned hydrodynamic spreading.* Journal of Micromechanics and Microengineering, 2007. **17**(10): p. 1992.

180. Dittrich, P.S. and A. Manz, *Lab-on-a-chip: microfluidics in drug discovery.* Nature Reviews. Drug Discovery, 2006. **5**(3): p. 210-218.

181. Aldaeus, F., et al., *Multi-step dielectrophoresis for separation of particles.* Journal of Chromatography A, 2006. **1131**(1–2): p. 261-266.

182. Talary, M.S. and et al., *Electromanipulation and separation of cells using travelling electric fields.* Journal of Physics D: Applied Physics, 1996. **29**(8): p. 2198.

183. Urdaneta, M. and E. Smela, *Parasitic trap cancellation using multiple frequency dielectrophoresis, demonstrated by loading cells into cages.* Lab on a Chip, 2008. **8**(4): p. 550-556.

184. Cui, H.-H. and K.-M. Lim, *Pillar Array Microtraps with Negative Dielectrophoresis.* Langmuir, 2009. **25**(6): p. 3336-3339.

185. Huang, Y., et al., *Differences in the AC electrodynamics of viable and non-viable yeast cells determined through combined dielectrophoresis and electrorotation studies.* Physics in Medicine and Biology, 1992. **37**(7): p. 1499.

186. Pardee, A.B., *Cancer Cells and Normal Cells.* Proceedings of the American Philosophical Society, 1976. **120**(2): p. 87-92.

187. Leather, A.J.M., et al., *Detection and enumeration of circulating tumour cells in colorectal cancer.* British Journal of Surgery, 1993. **80**(6): p. 777-780.

188. CARTER, B., et al., *Prediction of metastatic potential in an animal model of prostate cancer: flow cytometric quantification of cell surface charge*. Vol. 142. 1989, New York, NY, ETATS-UNIS: Elsevier.

189. Armitage, N.C., et al., *The influence of tumour cell DNA abnormalities on survival in colorectal cancer.* British Journal of Surgery, 1985. **72**(10): p. 828-830.

190. Stratton, M.R., *Exploring the Genomes of Cancer Cells: Progress and Promise.* Science, 2011. **331**(6024): p. 1553-1558.

191. Pethig, R., et al., *Dielectrophoresis: A Review of Applications for Stem Cell Research.* Journal of Biomedicine and Biotechnology, 2010. **2010**.

192. Holmes, D., et al., *Leukocyte analysis and differentiation using high speed microfluidic single cell impedance cytometry.* Lab on a Chip, 2009. **9**(20).

193. Asami, K., Y. Takahashi, and S. Takashima, *Dielectric properties of mouse lymphocytes and erythrocytes.* Biochimica et Biophysica Acta (BBA) - Molecular Cell Research, 1989. **1010**(1): p. 49-55.

194. Medoro, G., et al., *A lab-on-a-chip for cell detection and manipulation.* Sensors Journal, IEEE, 2003. **3**(3): p. 317-325.

195. Manaresi, N., et al., *A CMOS chip for individual cell manipulation and detection.* Solid-State Circuits, IEEE Journal of, 2003. **38**(12): p. 2297-2305.

196. Chen, D. and H. Du, *A microfluidic device for rapid concentration of particles in continuous flow by DC dielectrophoresis.* Microfluidics and Nanofluidics, 2009. **9**(2): p. 281-291.

197. Moncada-Hernández, H. and B. Lapizco-Encinas, *Simultaneous concentration and separation of microorganisms: insulator-based dielectrophoretic approach.* Analytical and Bioanalytical Chemistry, 2010. **396**(5): p. 1805-1816.

198. Balasubramanian, A.K., et al., *A microfluidic device for continuous capture and concentration of microorganisms from potable water.* Lab on a Chip, 2007. **7**(10): p. 1315-1321.

199. Hughes, M.P., H. Morgan, and F.J. Rixon, *Dielectrophoretic manipulation and characterization of herpes simplex virus-1 capsids.* European Biophysics Journal, 2001. **30**(4): p. 268-272.

200. Green, N.G. and H. Morgan, *Dielectrophoretic separation of nano-particles.* Journal of Physics D: Applied Physics, 1997. **30**(11): p. L41.

201. Deen, W.M., *Analysis of Transport Phenomena*, ed. K.E. Gubbins1998, New York: OXFORD UNIVERSITY PRESS.

202. Yang, F., et al., *Dielectrophoretic separation of colorectal cancer cells.* Biomicrofluidics, 2010. **4**(1): p. 013204-13.

203. Hu, X., et al., *Marker-specific sorting of rare cells using dielectrophoresis.* Proceedings of the National Academy of Sciences of the United States of America, 2005. **102**(44): p. 15757-15761.

204. Santiago, J.G., et al., *A particle image velocimetry system for microfluidics.* Experiments in Fluids, 1998. **25**(4): p. 316-319.

205. Zhao, Y., et al., *Phase-resolved optical coherence tomography and optical Doppler tomography for imaging blood flow in human skin with fast scanning speed and high velocity sensitivity.* Opt. Lett., 2000. **25**(2): p. 114-116.

206. Liu, C., et al., *A micromachined flow shear-stress sensor based on thermal transfer principles.* Microelectromechanical Systems, Journal of, 1999. **8**(1): p. 90-99.

207. Hu, H. and M.M. Koochesfahani, *Molecular tagging velocimetry and thermometry and its application to the wake of a heated circular cylinder.* Measurement Science and Technology, 2006(6): p. 1269.

208. Kuang, C. and G. Wang, *A far-field nanoscopic velocimeter for nanofluidics.* Lab-on-a-Chip, 2010. **10**: p. 240–245.

209. Kuang, C., et al., *Study of the Rise Time of Electroosmotic Flow within a Microcapillary.* Anal. Chem., 2009. **81**: p. 6590-6595.

210. Horoszewicz, J.S., et al., *LNCaP Model of Human Prostatic Carcinoma.* Cancer Research, 1983. **43**(4): p. 1809-1818.

211. Wang, Z.-P., et al., *Identification and characterization of circulating prostate carcinoma cells.* Cancer, 2000. **88**(12): p. 2787-2795.

212. Zeng, C., et al., *Evaluation of 5-ethynyl-2'-deoxyuridine staining as a sensitive and reliable method for studying cell proliferation in the adult nervous system.* Brain Research, 2010. **1319**: p. 21-32.

213. Yang, R., D.L. Feeback, and W. Wang, *Microfabrication and test of a three-dimensional polymer hydro-focusing unit for flow cytometry applications.* Sensors and Actuators A: Physical, 2005. **118**(2): p. 259-267.

214. L. M. Levine, T.C., *Combining Additive and Subtractive Techniques in the Design and Fabrication of Microfluidic Devices*

215. Sreenivasan, K.R., *The passive scalar spectrum and the Obukhov-Corrsin constant.* Phys. Fluids, 1996. **8**: p. 8.

216. Chen, S., et al., *Far-Dissipation Range of Turbulence.* Physical Review Letters, 1993. **70**(20): p. 4.

217. Saddoughi, S.G. and S.V. Veeravalli, *Local isotropy in turbulent boundary layers at high Reynolds number.* Journal of Fluid Mechanics, 1994. **268**: p. 40.

218. Comte-Bellot, G. and S. Corrsin, *Simple Eulerian time correlation of full- and narrow-band velocity signals in grid-generated, 'isotropic' turbulence.* Journal of Fluid Mechanics, 1971. **48**: p. 65.

219. Mydlarski, L. and Z. Warhaft, *Passive scalar statistics in high-Peclet-number grid turbulence.* J. Fluid Mech., 1998. **358**: p. 135-75.

220. Jayesh, C. Tong, and Z. Warhaft, *On temperature spectra in grid turbulence.* Phys. Fluids, 1994. **6**: p. 306-312.

221. Jaewan, P., et al., *Application of electrokinetic instability for enhanced mixing in various micro-channel geometries*, in *Physics of Fluids*2005, American Institute of Physics. p. 118101.

222. Corless, R.M., et al., *Two Perturbation Calculations in Fluid Mechanics using Large-expression Management.* Journal of Symbolic Computation, 1997. **23**(4): p. 427-443.

223. Fiedler, H.E. and H.H. Fernholz, *On management and control of turbulent shear flows.* Progress in Aerospace Sciences, 1990. **27**(4): p. 305-387.

224. Yang, F., et al., *Dielectrophoretic separation of colorectal cancer cells.* Biomicrofluidics, 2009. **4**(1): p. 013204-13.

225. Song, H. and D. Bennett, *Numerical study of enhancing the mixing effect in microchannels via transverse electroosmotic flow by placing electrodes on top and bottom of the channel.* Microsystem Technologies, 2011. **17**(9): p. 1427-1437.

226. Ewing, D., *The effect of cross flow on one-dimensional spectra measured using hot wires.* Experiments in Fluids, 2004. **36**: p. 10.

227. Wyngaard, J.C. and S.F. Clifford, *Taylor's hypothesis and high-frequency turbulence spectra.* Journal of Atmospheric Sciences, 1977. **34**: p. 8.

228. Kuang, C., R. Qiao, and G. Wang, *Ultrafast Measurement of Transient Electroosmotic Flow in Microfluidics.* Microfluidics and Nanofluidics, 2011. **11**: p. 353-358.

229. Kuang, C., et al., *Study of the Rise Time in Electroosmotic Flow within a Microcapillary.* Analytical Chemistry, 2009. **81**(16): p. 6590-6595.

APPENDIX

1 EKI mixing visualization

To visualize the fast diffusion, we use Laser induced fluorescence. Two streams of fluids will diffuse and mix in the microchannel. One stream has fluorescent dye solution and the other is pure water. Fluorescein sodium salt (C20H10Na2O5) solution was used for the visualization in Fig. 4.1. The reason of using fluorescein instead of Coumarin is that our microscope does not have the cube that matches the excitation and emission of the Coumarin, and the signal is weak with Coumarin. In addition, the selection of dye should have no influence on the mixing dynamics. On the other hand, for velocity measurement, two streams have the same dye concentration. When polystyrene microparticles are used for visualization of the flow, their corresponding dielectrophoresis (DEP) effect on particle motion may be neglected since the bulk velocity is much larger than the velocity caused by DEP.

2. Calibration for LIFPA

Since LIPFA is very similar to a hotwire anemometer, we can approximately use similar data processing method used in hotwire for the LIPFA. Based on measured calibration curve between flow velocity and fluorescence intensity, the flow velocity can be calculated by measuring the fluorescence intensity. According to the LIFPA model,

fluorescence intensity I_f increases with fluid velocity u. The calibration curve for current setup is shown in Fig. A1. Coumarin 102 dye solution with concentration of 20 μM was used for the two streams for this study. Hence, the fluorescence concentration is the same in the entire microchannel and the only reason that causes the variation in fluorescence intensity is because of photobleaching, i.e. the change of flow velocity.

Apparently if the flow is not one dimensional, the measured signal should be the norm of three components of velocity, i.e. u (streamwise component) and v (transverse component). This will not significantly affect the statistical and spectral analysis [217, 226, 227] of the measured velocity for demonstration that the flow is turbulence.

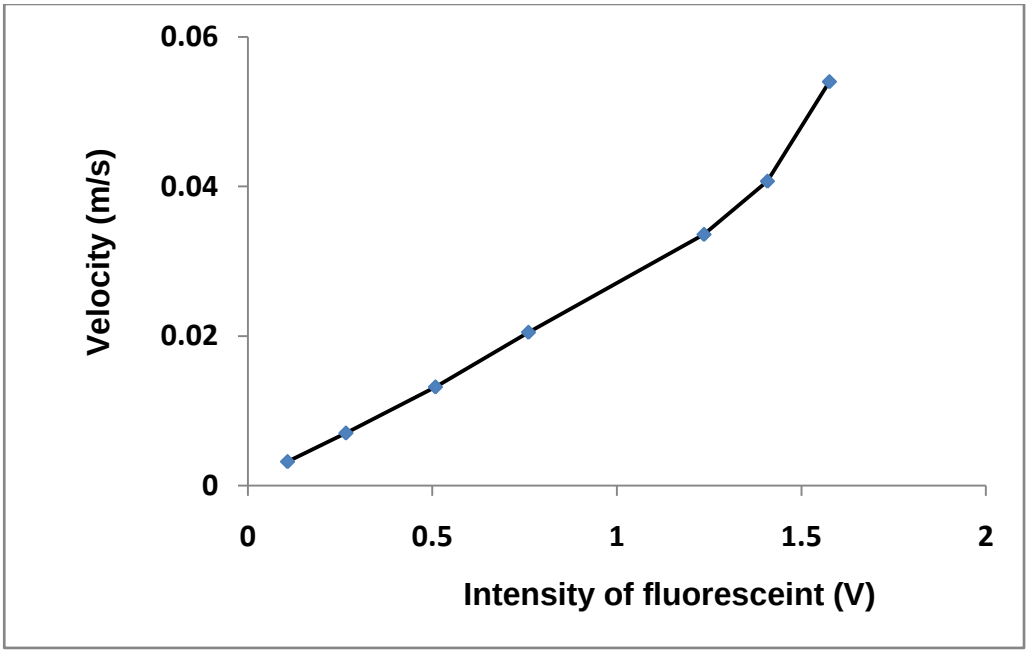

Figure A1. Calibration between flow velocity and fluorescence intensity.

3. Spatial resolution

The spatial resolution of the LIFPA is approximately determined by the focused laser beam volume that is circular cylindrical. The diameter and the length of this detection volume is estimated to be approximately 203 nm and 812 nm respectively.

4. Temporal resolution of our LIFPA

Since the transient velocity fluctuation can have high frequency in the order of 1000 Hz, high temporal resolution is required for LIFPA, in order to ensure that the high frequency single will not be lost. The rise time of DC electroosmotic flow (EOF) is measured to validate the ultrafast time resolution of LIFPA, since this is one of the most basic transient electrokinetic flows and a very fast dynamic process.

In our experiment, a neutrally charged, small molecular dye Coumarin 102 (Sigma-Aldrich Corp., MO) has been used, to eliminate this effect on EOF. This dye has a relatively high quantum efficiency of photobleaching, with a high absorption coefficient at around 400 nm wavelength and high emission coefficient around 460 nm wavelength. The dye was diluted with methanol to a neutral dye solution with concentration of 20 μM. it is easy to keep the dye concentration uniform in the entire microcapillary, since the molecule size of the dye Coumarin 102 is about 0.6 nm.

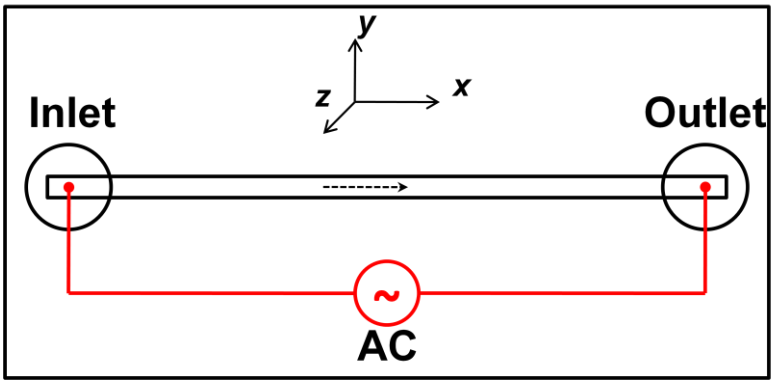

Figure A2 Flow, electrodes configuration and force descriptions.

A brief structure description of the microchannel chip is shown in Fig. A2. The chip was made using plastic lamination based microfabrication.[213] Two transparent acrylic plastic substrates of 24 mm x 20 mm x 1.25 mm were used as top (cap) and bottom layer respectively. One inlet and one outlet wells are drilled on the top layer. The diameter of all the wells is 1/16 inch. Channel is formed on a middle layer, with height of 40 μm, width of 200 μm respectively.

The microchannel was placed on a 3D translation stage. A syringe pump Harvard PHD 2000 was used to drive two syringes containing fluorescence dye (Coumarin 102) solution to deliver the two streams of fluids with different conductivity to the microchannel. A Tektronix function generator, Model AFG3102 was used to provide 20 $V_{p\text{-}p}$ amplitude signals. A continuous wave laser (405 nm in wave length) has been used as excitation source. The expanded laser beam was focused to the detection point by an objective (PlanApo, NA 1.4 oil immersions, Olympus, NY). The detailed optical setup is given in earlier publication.[208, 228] The fluorescence signal was captured by a

photomultiplier (PMT, HAMAMATSU, R-928) with high sensitivity. The PMT was connected to an AD converter, LabVIEW SignalExpress was used to monitor and record data. Here, a frequency of the lowpass filter for the current preamplifier was utilized to decrease the influence of random noise. The sampling rate is 12.8 kHz and the cut-off frequency (The frequency of the lowpass filter for the current preamplifier) f_{sc} is 3 kHz to optimize the signal-noise ratio.

Two electrodes were placed at the inlet and outlet of the microchannel respectively, and a 20 V_{p-p} DC signal was applied to these electrodes. Fluorescence dye solution with 5000 μS/cm conductivity was injected into the channel.

4.1 Power spectra

In our experiment, EOF response time was measured in the term of power spectra magnitude at each applied AC frequency. For example, in the microchannel with length of 2 mm, when we apply an AC signal with 400 Hz to the electrodes, EOF flow was generated in this microchannel. Using an AD convertor, the fluorescent signal captured by PMT was recorded by LabView SignalExpress. Also by this software, the signal was analyzed, and then a power spectrum in frequency domain was generated based on the acquired signal as shown in Fig A3.

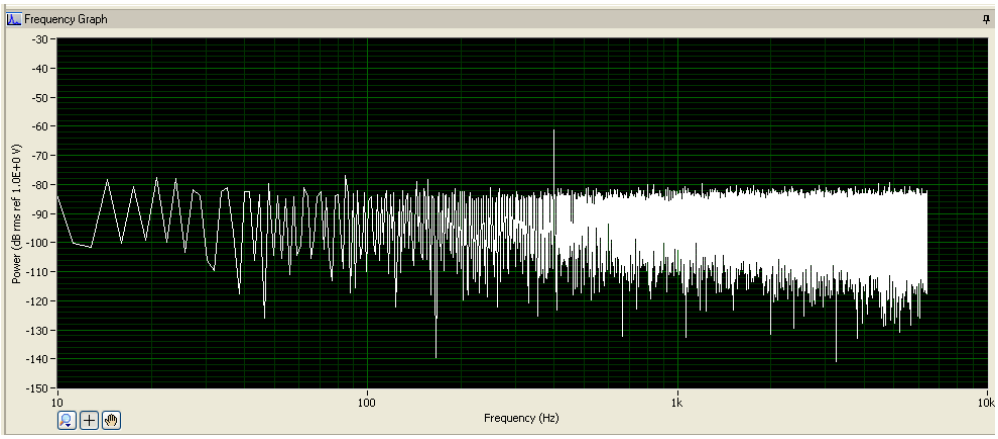

Figure A3 Power spectra at frequency 400 Hz of applied AC signal, generated by LabVIEW SignalExpress.

In Fig A3, an obvious peak was generated at frequency of 400 Hz. This result indicated that, when we apply AC signal with 400 Hz frequency to the flow, EOF flow was generated. The flow velocity changes with every direction change of the AC electric field. In another word, the EOF respond to the AC electric field in the terms same frequency (400 Hz) velocity fluctuation. When refers to the fluorescent signal, there was 400 Hz fluctuation in the signal time trace which is characterized in the power spectra, in the form of a peak at 400 Hz. Furthermore, the magnitude of peak indicated the strength of the EOF velocity fluctuation. As we know that, the stronger the EOF velocity fluctuation, the higher power spectra magnitude (at applied frequency) is. When there is no EOF response to applied AC signal, there is no peak at the applied frequency on the power spectra. Therefore, by comparing highest frequency with a peak in the power spectra, we can compare the EOF response time in different experiment conditions (channel length, detection position, conductivies), and by peak magnitude at each

frequency, we can compare the EOF fluctuation at each applied frequency in different experiment conditions.

4.2 Channel length effect

EOF response times were first compared in three microchannels with different length, which are 2 mm, 5 mm and 10 mm. In this experiment, the conductivity was kept at 1 μS/cm, same AC signals were applied on three microchannels between inlet and outlet, the amplitude of applied AC signal was also kept the at 20 V_{p-p} , frequencies of applied AC signal was adjusted between 10 Hz to 3kHz.

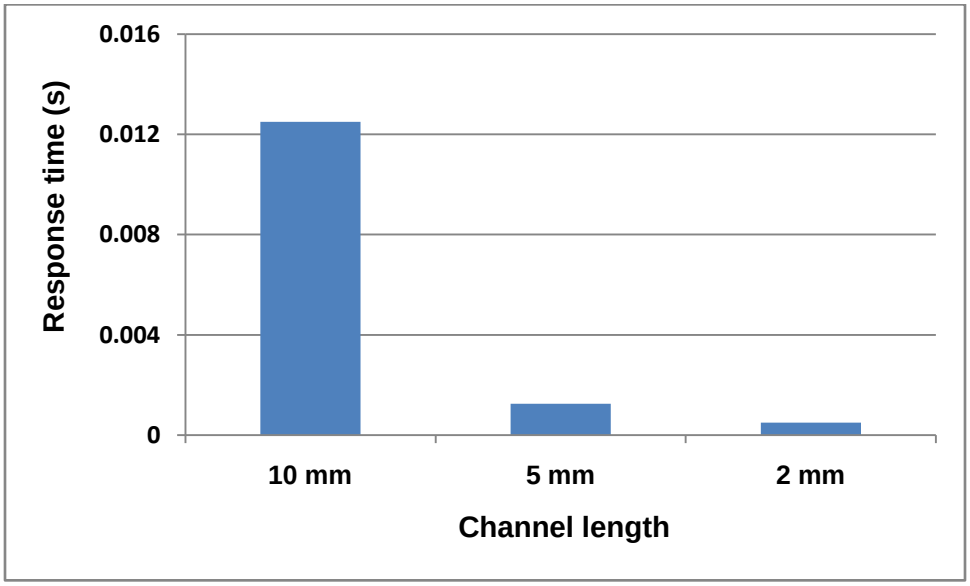

Figure A4 Comparison of response time in different length microchannel, in the term of power spectra magnitude at each applied AC frequency.

EOF response times in three microchannels with different length are shown in Fig. A4. In the microchannel with length of 2 mm, the response time is shorter than that in the channels of 5 mm and 10 mm lengths. According to the acquired power spectra magnitude at each applied AC frequency in three different microchannel, when the

channel length is 2 mm, at 400 Hz applied AC frequency, the magnitude of power spectra peak is about 4 times higher than that in 5mm microchannel, while at the same applied AC signal, in the 10 mm microchannel, there is no power spectra peak which means no EOF response. In the 2 mm microchannel, there is still a small peak at 2 kHz in its power spectra. EOF flow is response to the AC signal as high as 2 kHz. It indicated that, the EOF response time in this 2 mm microchannel is less than 0.0005 s. Meanwhile, in the 5 mm and 10 mm microchannels, the highest frequency to have a power spectra peak are 800 Hz and 80 Hz. EOF flows in these channels are response to AC signals as high as 800 Hz and 80 Hz, the EOF response times for these microchannels are about 0.00125 s and 0.0125 s. Which are much longer than that in a 2 mm microchannel.

It is noticed that, in the shorter microchannel, the EOF flow had a shorter response time to the applied AC electric field. This phenomenon could be explained by that, the applied electric field plays a key role in the EOF flow. It is an obvious fact that, by the same applied AC signal (20 V_{p-p}), the electric field is stronger in the short microchannel than that in the longer microchannel. Consequently, the stronger electric field leads to a higher acceleration of EOF flow, faster response speed, and shorter response time.

4.3 Position effect

Since the EOF flow's velocity profile is not uniform at $t = 0$, the velocity near side wall will be higher than that far away from side wall,[229] we here also compare the EOF response time at two different position in the 2 mm microchannel. One position is within 1 μm to the side wall, the other one is 20 μm from the side wall. In this

experiment, the conductivity was kept at 1 µS/cm, same AC signals were applied on three microchannels between inlet and outlet, the amplitude of applied AC signal was also kept the at 20 V_{p-p} , frequencies of applied AC signal was adjusted between 10 Hz to 3kHz.

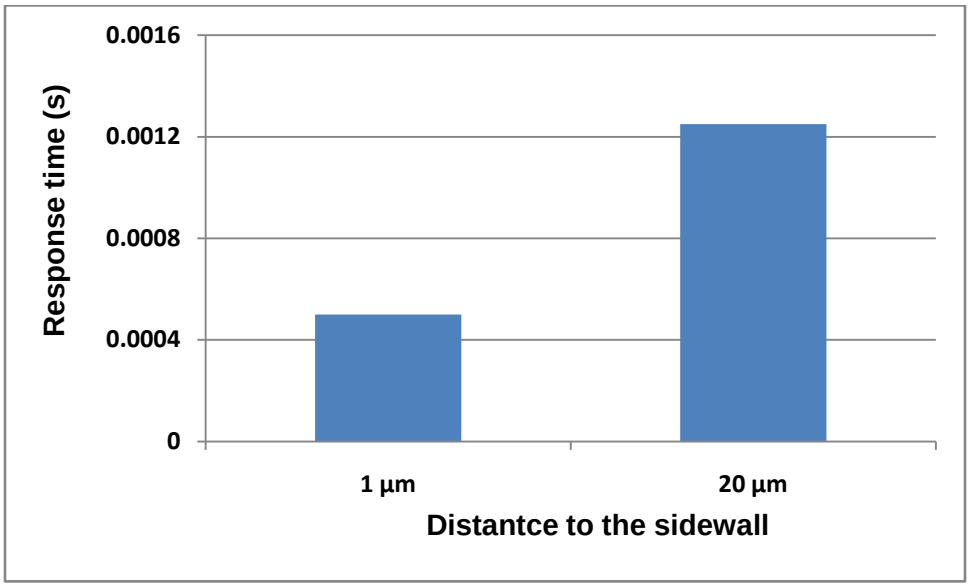

Figure A5 Comparison of response time at different positions in microchannel.

EOF response times two different position in the 2 mm microchannel are shown in Fig. A5. At the position within 1 µm to the side wall, the response time is shorter than that at the position of 20 µm from the side wall. According to acquired power spectra, at the position within 1 µm to the side wall, at 1 kHz applied AC frequency, the magnitude of power spectra peak is about 2 times higher than that 5 µm from the side wall, which means that velocity fluctuation is stronger at 1 µm to the side wall. Furthermore at position within 1 µm to the side wall, there is still a small peak at 2 kHz. EOF flow is response to the AC signal as high as 2 kHz. It indicated that, the EOF response time at position within 1 µm to the side wall is less than 0.0005 s. Meanwhile, at position of 20

μm from the side wall, the highest frequency to have a power spectra peak is 800 Hz. EOF flows at that position response to AC signals as high as 800 Hz, the EOF response times is about 0.00125 s which is much longer than that at position within 1 μm.

The response time in the center is longer than it is near the wall. This phenomenon could be explained by that, because the charged surface attains its maximum velocity shortly after the electric field is turned on. Subsequently, this liquid layer close to surface exerts frictional shear stress on the adjacent layer of liquid. The liquid is then driven by friction stress layer by layer.

4.4 Conductivity effect

EOF response times were also compared with three different conductivities of dye solution, which are 1 μS/cm, 2000 μS/cm, 5000 μS/cm. In this experiment, same AC signals were applied on three microchannels between inlet and outlet, the amplitude of applied AC signal was also kept the at 20 V_{p-p} , frequencies of applied AC signal was adjusted between 10 Hz to 3kHz.

EOF response times with three different conductivities of dye solution are shown in Fig. A6. With the conductivity of 1 μS/cm, the response time is shorter than that with 2000 μS/cm, 5000 μS/cm. According to acquired power spectra, when the conductivity is 1 μS/cm, at 100 Hz applied AC frequency, the magnitude of power spectra peak is about 4 times higher than that with 2000 μS/cm conductivity, while at the same applied AC signal, with 5000 μS/cm, the power spectra peak is very low which means there is almost no EOF response. Furthermore, it is shows that, with 1 μS/cm, EOF flow response to the AC signal as high as 2 kHz. It indicated that, the EOF response time with 1 μS/cm

conductivity solution is less than 0.0005 s. Meanwhile, with 2000 μS/cm, 5000 μS/cm conductivity solutions, the highest frequency to have a power spectra peak are 200 Hz and 100 Hz. EOF response times for these conductivity solutions are about 0.005 s and 0.01 s. Which are much longer than that that when the conductivity is 1 μS/cm.

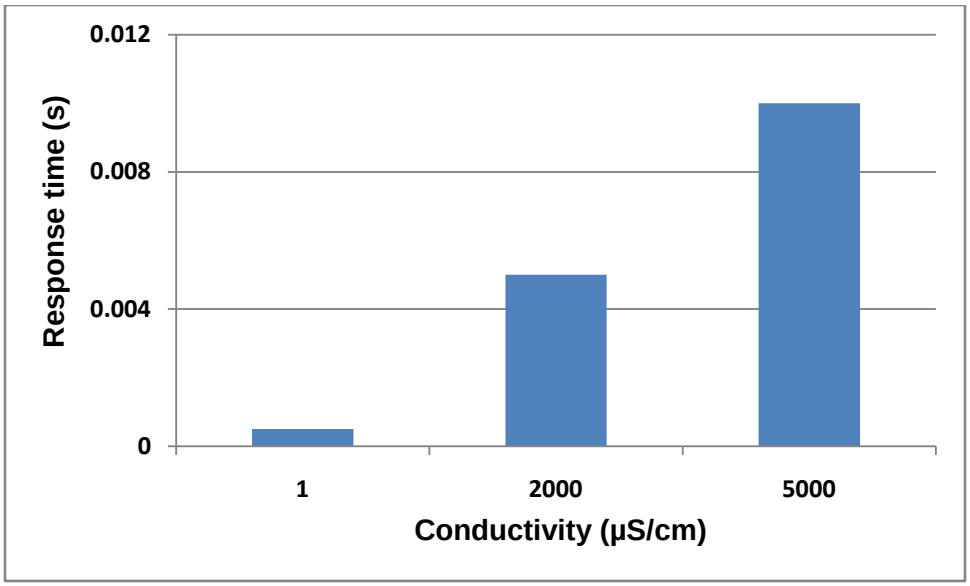

Figure A6 Comparison of response time by different conductivity dye solution in microchannel.

5 Conductivity effect

Another concern is if conductivity has influence on fluorescence intensity. To validate that the fluorescent intensity does not change with conductivity variation, we measured fluorescent intensity of same dye concentration solution with different conductivity (from 0 to 13,200 μS/cm). Result is displayed in Fig. A7, which shows that fluorescent intensity, does not change with the conductivity within the range of 1-5,000

μS/cm, which was used in our experiment.

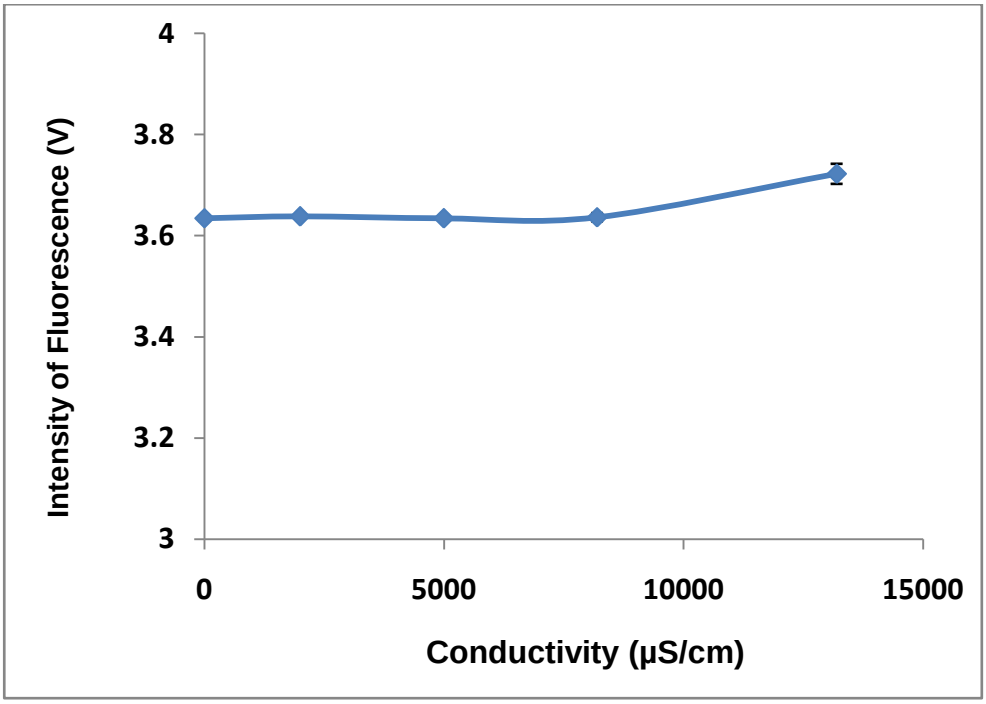

Figure A7 Fluorescent intensity of Coumarin solutions with different conductivitie. Within the conductivity range of 1 – 5,000 μS/cm, that was involved in the Coumarin solution used in the experiment, the fluorescent intensity was not dependent of the conductivity of the solution.

6 Conductivity gradient effect

To ensure that the fluorescence signal variation is purely caused by the flow velocity, we also test if conductivity gradient will have any influence on fluorescence intensity. We change the conductivity ratio of the two initial streams at the entrance to generate the conductivity gradient and measure the fluorescence signal at the interface between the two streams downstream. The result indicates that the conductivity gradient has no effect on the fluorescence intensity as shown in Fig. A8.

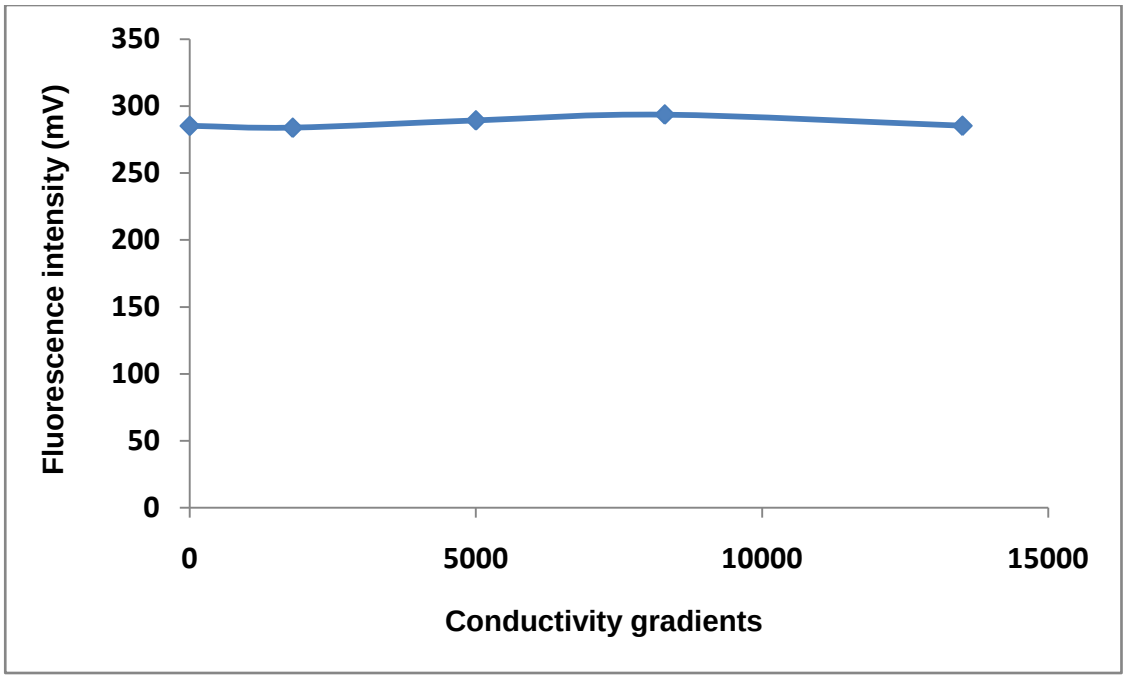

Figure A8 Fluorescent intensity of Coumarin solutions with different conductivity gradients.